Kirk-Othmer Encyclopedia of Chemical Technology.

SUPERCONDUCTIVITY AND SUPERCONDUCTORS

1. Introduction

1.1. Discovery of Superconductivity

H. Kamerlingh Onnes, successfully liquefied helium in 1908 and then went on to investigate the low temperature resistivity of mercury in 1911. He found that the resistivity fell abruptly at 4.2 K (−269°C) and proposed that mercury had entered a novel physical state (1). This phenomenon was called superconductivity, and the temperature at which it occurred is called the critical temperature, T_c. Since the discovery of superconductivity in metallic mercury, an intensive and persistent materials research over a 90-year period resulted in a continuous increase of critical temperature and finally a mercury-base superconducting perovskite material $HgBa_2Ca_2Cu_3O_9$ was discovered, which was characterized by highest known critical temperature ∼ 163 K, but room temperature superconductivity was as yet unattainable. Much effort was put into the search for new superconducting materials and structural characterization of the possible higher T_c superconductors. Even combinatorial techniques were used to search for such an improved T_c. The research to find a unified description–representation of the crystal structures of copper-containing ceramic superconductors (2) was mainly conducted to provide hints for the determination of still unknown crystal structures or possible new structural patterns of even higher T_c superconductors.

1.2. Critical Temperature

The generally accepted definition of T_c is the midpoint of the resistive transition (3). The resistive transition of the composite superconductors and multiphase superconductors reveal only the best continuous superconducting path that exists along the sample. If such a path exists, T_c takes its highest value and does not reflect the actual volume properties of such superconducting materials.

Magnetic susceptibility measurements of the superconducting material may reveal the superconductivity of the discontinued or even isolated superconducting phases in the samples, but also they may give slightly lower T_c values than the resistive transition because of the local suppression of the superconducting parameters by the penetrating magnetic field (4). Over the last 90 years many Nobel Prize winners were awarded for their direct and indirect contribution to superconductivity. Many more Nobel Prize winners were awarded for their discoveries in the area related to basic and applied superconductivity.

1.3. Meissner Effect (Diamagnetic and Paramagnetic Supercurrents)

Surprisingly, for more than two decades after its discovery, superconductivity was considered to be a state of zero electrical resistance. Not until 1933, with the discovery of the Meissner effect, did it become evident that a totally different phenomena was actually involved, namely, that of perfect diamagnetism. The Meissner state or state of magnetic flux expulsion is the lowest free energy state of a bulk superconductor as long as the externally induced magnetic field is less than the so-called first critical field H_{c1}. An externally applied magnetic field $H_a < H_{c1}$ produces a flux density, B, in the superconductor, but diamagnetic superconducting screening currents, i_d, generate an internal flux density that is exactly equal everywhere and opposite to this flux density. Consequently, the net flux density is zero. (The net flux density in a sphere is zero only up to the two-thirds of H_{c1} of the material used, due to the demagnetizing coefficient, N.)

It is critical to understand the consequences of perfect diamagnetism and the role of paramagnetic and diamagnetic supercurrents for applications of superconductivity, eg, levitation and suspension. Therefore a defect free, infinitely long superconducting tube in a parallel external magnetic field (demagnetizing coefficient $N = 0$) is considered. If such a superconducting tube is exposed to the external magnetic field H_{c1}, a diamagnetic current called the Meissner current, i_d, is flowing on the outside surface of the superconducting tube Fig. 1**a**. If such a superconducting tube is exposed to an external magnetic field $> H_{c1}$ and subsequently the field is reduced to a value less than H_{c1}, or alternatively the magnetic field $H_{\mathrm{a}} < H_{\mathrm{cl}}$ is applied before the material is cooled below its T_c, two superconducting currents are created. One superconducting current is flowing on the outside surface of the tube, which is a diamagnetic Meissner current i_d. On the other hand, the second is flowing on the inside surface of the tube in the opposite direction to i_d, and is called the paramagnetic current, i_p (Fig. 1**b**). Paramagnetic supercurrent supports the flux threading inside space of the superconducting tube. In the presence of the external magnetic field, both currents must circulate to maintain these differences in the flux density inside and outside the superconducting tube. The net circulating current $i_n = i_d - i_p$ is what generates a flux density equal to the difference between the flux density outside the superconducting tube and the flux density inside the tube. If the external magnetic field is reduced to zero, i_d is also reduced to zero, whereas an paramagnetic superconducting current, i_p, set up in a superconducting tube by trapped magnetic flux inside the tube, will circulate indefinitely without dissipation exhibiting electrical perpetual motion (Fig. 1**c**).

1.4. Flux, Fluxoid, Fluxon, and Cooper Pairs

There is a fundamental difference in the magnetic flux behavior outside a superconducting body and inside the superconductor. Outside the superconductor there is a continuous flux, Φ; but the space surrounded by continuous superconductor there is Fluxoid, Φ’. The equation known as a “quantum condition” or “phase condition”, which describes the Fluxoid, can be expressed as follows:

$$\frac{m}{n_s e^2} \oint J_s \cdot dl + \int \int_s B \cdot dS = n \frac{h}{2e} = \Phi' = n\Phi_{\mathrm{o}} \tag{1}$$

where n_s is a density of superelectrons, m is electron mass, and h is Planck’s constant. The first term on the left side of equation 1 contains the line integral of the paramagnetic current density around the superconductor–normal interface. The second term is the magnetic flux contained within a normal region. As one may deduce from the quantum condition that any Flxuoid Φ’ contained within a superconductor should only exist as multiples, n, of a flux quantum, the Fluxon $\Phi_{\mathrm{o}} = h/2e = 2.07 \times 10^{-15}$ Weber. Because the phase of the wave function around the Fluxon containing regions may only change as a 2π wave function surrounding the Fluxoid Φ’ present in the normal zone or hole in the superconductor, it can be only a multiple of 2π. Division by twice the electronic charge in equation 1 is strong evidence that the supercurrent is carried by pairs of electrons. In 1956, Cooper showed that the electrons in certain metals below T_c existed not as individual particles, but as coupled pairs (5). Following this finding Bardeen, Cooper, and Schrieffer (BCS theory) constructed a microscopic theory of superconductivity, which provided an explanation for this phenomenon (6). For BCS superconductors, the attractive interaction is attributed to the so-called electron–phonon interaction. Such a mechanism is supported by the observed isotopic effect in which the critical temperature T_{c} is proportional to $M^{1/2}$ (7,8), the mass of ions forming the crystal lattice.

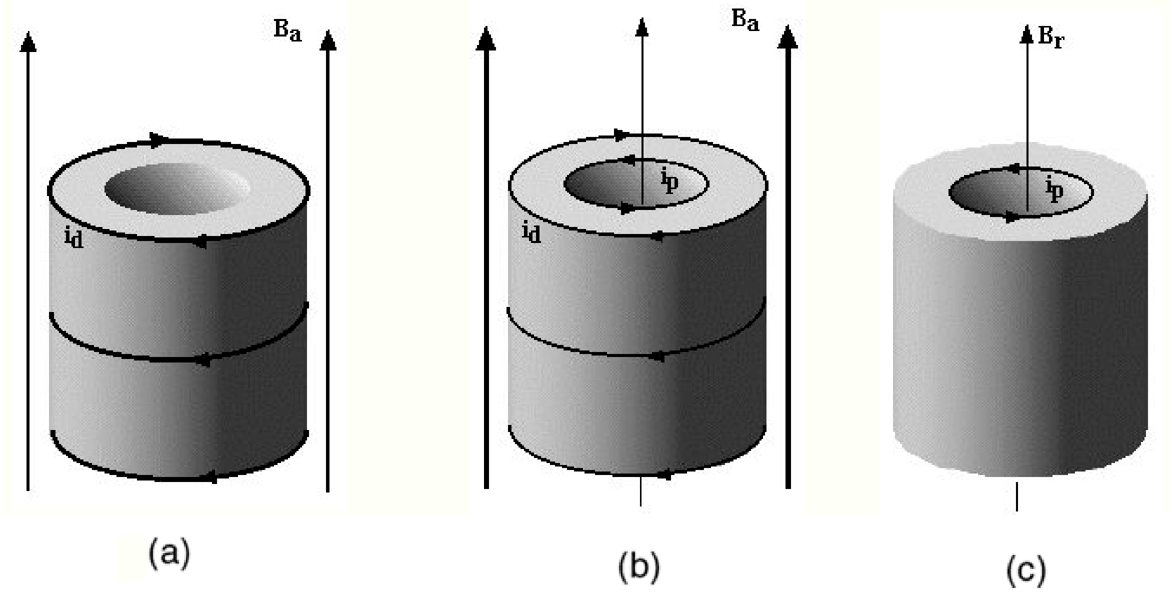

Fig. 1. Hollow superconductor: (**a**) the magnetic field is applied when the material in the fully superconducting state (applied magnetic field is smaller than the H_{c1}) the only superconducting current is a diamagnetic Meissner current, i_{d}; (**b**) material becomes superconducting in a magnetic field or by application of the magnetic field $>H_{\mathrm{c1}}$ there is a paramagnetic current, i_p, flowing on the inner surface of the hole to support the flux in the normal zone in the superconductor; (**c**) after reduction of the applied magnetic field to zero the induced $i_d = 0$ and the i_p remain only to support flux trapped in the normal region. The $i_d - i_p$ is the net circulating current, i_{n}, which generates a flux density equal to the difference between the flux density in the hole and the flux density outside the superconducting body.

An oversimplified picture of the electron–phonon interaction can be described as follows: consider an electron moving through a lattice of positive ions, the lattice will become slightly distorted by the Coulombic attraction between the electron and ions with the result that temporarily there will be a higher density of positive charge at points near the path of the electron as it passes the ions. When a second electron approaches the path of the first one, in the brief interval before the lattice relaxes, it could experience an attractive force because of the temporarily higher positive charge. If the attractive force can overcome the normal Coulombic repulsion between electrons, a net attraction between the two electrons is obtained. The effective net attraction between the normally repulsive electrons produces a pair binding energy on the order of millielectron volts (meV), enough to keep them paired at extremely low temperatures.

The BCS theory is based on the wave function in which all the electrons are paired. Because the total momentum of the Cooper pair is unchanged by the interaction between one of its electrons and the lattice, the flow of electrons continues indefinitely. Therefore, to break a Cooper pair to create two quasiparticle excitations, a certain amount of energy (denoted by 2Δ) is needed. The parameter 2Δ is usually called the energy gap, which is a function of temperature, (eq. 2)

$$2\Delta(\mathrm{o}) \approx E_g \approx \frac{7}{2} k_{\mathrm{B}} T_c \tag{2}$$

T_c is given by $k_{\mathrm{B}} T_c = 1.14\, h\omega_{\mathrm{D}} \exp(-1/\lambda*)$, where $h\omega_{\mathrm{D}}$ is the Debye energy, k_{B} is the Boltzmann constant, and $\lambda*$ is a dimensionless electron–phonon coupling strength. In the weak coupling limit, $\lambda*$ is $\ll 1$ and T_c is low.

As $\lambda*$ increases, the tightly bound pairs of fermions form bosons to which Pauli's exclusion principle does not apply. The energy gap is related to the coherence length ξ for the superconductor, one of the two characteristic lengths associated with superconductivity.

According to BCS theory, all electrons are bound in the superconducting state into identical two-electron states. In other words, all the pairs that are bosons are described by an identical pair of wave functions. Thus, one cannot change the pair wave functions individually without destroying the paired state altogether with an enormous cost in free energy. This is the reason Cooper pairs are not subject to scattering by phonons or impurities so that zero resistance is observed. In other words, in an ideal metal, the electric energy is transported by free electrons that experience collisions with the crystal lattice. Whereas in metallic superconductors, electron Cooper pairs are responsible for the resistiveless conductivity through the interaction with phonons without actual dissipation on the crystal lattice (electron–phonon interaction). There has been much experimental evidence indicating the existence of Cooper pairs in high T_c ceramic oxide superconductors (9). However the mechanism that facilitates the pairing at such high temperatures is not yet clear. There are two important questions that need to be answered. What are the quasiparticles responsible for the normal conduction? What is the interaction that pairs these quasiparticles in the superconducting state? So far many theories have been proposed (10), but they are still to be verified by experiments. Besides high T_c superconductors, there are a number of other novel materials that exhibit superconductivity and whose properties cannot be explained very well by the BCS theory (11). These materials include organic and heavy fermion superconductors.

1.5. Specific Heat

Specific heat is an important physical parameter that provides important information [together with the far-infrared and microwave absorption measurements] about the existence of an energy gap in the excitation spectrum of superconductors. The electronic specific heat coefficient $\gamma = C_{\mathrm{el}}/T$ is determined solely by the nature, magnitude, and energy dependence of the spectrum of excitations lying within an energy range $\sim k_{\mathrm{B}}T$ of the chemical potential. Therefore a jump in specific heat at the T_c is a very reliable probe of bulk superconductivity and the doping effects on superconductivity. There are four important features that characterize the specific heat profile for superconducting materials: (*1*) sharp jump in the specific heat at $T = T_c$; (*2*) a crossover followed by lower values of specific heat for a superconductor in comparison to normal material; (*3*) excess specific heat in the superconducting state near T_c and finally (*4*) exponential rather than power low behavior at the lowest temperatures.

1.6. Penetration Depth and Coherence Length : Definition of the Type of Superconducting Properties

A product of the theoretical and experimental investigations of superconductivity are two characteristic lengths; the coherence length ξ and the London penetration depth λ. The relative differences between these values are characteristic for different superconducting materials and define the character of the interfacial energy between the normal and superconducting region. Thus, the applicability of the superconducting material.

1.6.1. Coherence Length

The superconducting coherence length ξ was first introduced by Pippard (12). Coherence length can be defined as a characteristic distance over which the Cooper electron pairs act coherently together, which obviously varies for different superconducting materials. The estimate of ξ_o obtained from BCS theory (12) yields

$$\xi_o = \frac{\hbar \nu_{\mathrm{F}}}{\Delta} = 0.18\,(\frac{\hbar \nu_{\mathrm{F}}}{k_{\mathrm{B}} T_c}) \tag{3}$$

where Planck's constant is divided by 2π, v_F is the Fermi velocity, Δ is the superconducting energy gap, and k_B is the Boltzmann constant. Behavior of a typical superconductor suggests that electron pairs (Cooper pairs) are coupling over a range of hundreds of nanometers, three orders of magnitude larger than the lattice spacing, but the distance between electrons in normal metal is comparable to lattice spacing. If all the pairs have the same momentum, the continuous recombination of the new pairs is plausible. All bosons are described by the same wave function.

This important concept of coherence length was formulated by Pippard (13), where a superconductor can be regarded as consisting of two interpenetrating electron fluids: the normal electrons (quasi particles) and the superelectrons. For the practical application of Type II superconductors when local electrodynamics is important, Pippard introduced the modified coherence length eq. (4).

$$\frac{1}{\xi_p}=\frac{1}{\xi_o}+\frac{1}{l_e} \tag{4}$$

where ξ_o is London coherence length and the l_e is a mean free path for electron in material.

1.6.2. Penetration Depth

Penetration depth refers to the exponentially decaying magnetic field at the surface of a superconductor. It is related to the density of superconducting electrons in the material. The London equations are one of the theoretical approaches to the description of the superconducting state (14). They relate the curl of the current density J to the magnetic field:

$$\nabla\times J_S=-\frac{1}{\mu_o\lambda_L^2}B \tag{5}$$

$$J_S=-\frac{1}{\mu_o\lambda_L^2}\cdot E \tag{6}$$

where λ_L is a London penetration depth.

London suggested that the magnetic behavior of the superconductor might be correctly described if differential equation 7 is applied not only to B itself (14). Therefore

$$\frac{\partial^2 B(x)}{\partial x^2}=\frac{1}{\alpha}B(x) \tag{7}$$

where $B(x)$ is the flux density at distance x inside the metal. This equation has the solution

$$B(x)=B_a\exp(\frac{-x}{\sqrt{\alpha}}) \tag{8}$$

where B_a is the flux density of the applied field at the surface. Equation 8 shows that the flux density dies away exponentially inside a superconductor, falling to $1/e$ of its value at the surface at a distance $x=\sqrt{\alpha}$.

London penetration depth, λ_L, is the distance required to fall to $1/e$ times the externally applied field B_a.

$$\lambda_L=\sqrt{\frac{m}{\mu_0 n_s e^2}} \tag{9}$$

Table 1. Critical and Characteristic Parameters of Metallic Superconductors

Material	Coherence range, ξ, nm	London penetration depth, λ, nm	G–L parameter, κ	Critical temperature, T_c, K	Thermodynamic critical field H_c, mT
Pb	83	37	0.45	7.2	80
Sn	230	34	0.16	3.7	30
Cd	760	110	0.14	0.57	3
Al	1600	16	0.01	1.2	1
Nb[a]	38	39	1.02	9.2	198

[a] Type II superconductor.

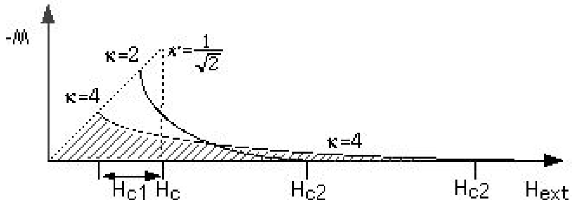

Fig. 2. Magnetization curves of superconductors in relation to the external magnetic field: Type I superconductors $\kappa<1/\sqrt{2}$, Type II superconductors $\kappa>1/\sqrt{2}$. The parameter H_c represent the thermodynamic magnetic field that is a characteristic value for the superconducting material. Up to H_{c1} there is a Meissner state and above H_{c1}, but below H_{c2}, there is a mixed state (15).

where m, e, and n_s are the electron mass, charge, and superelectron density, respectively. The experimental values of the temperature-dependent penetration depth $\lambda(T)$ can be fitted by the empirical equation

$$\lambda(T)=\lambda(0)[1-(\frac{T}{T_c})^4]^{-1/2} \tag{10}$$

The value of λ will vary for different materials, see Table 1 for some examples.

1.6.3. Ginzburg-Landau Parameter (G–L)

Both these characteristic parameters are described above: λ and ξ define one of the most important parameters, the Ginzburg-Landau parameter $\kappa=\lambda/\xi$. The value of κ categorizes materials into basic Type I superconductors, $\kappa<1/\sqrt{2}$ (surface energy positive, not important for applications), and Type II superconductors, $\kappa>1/\sqrt{2}$ (surface energy negative, potentially very applicable superconducting materials) (Fig. 2).

At the boundary between the normal and the superconductor, the density of superconducting electrons rises, gradually from zero (in the normal region) to its maximum density (in the superconducting region) over a distance equal to about the coherence length, ξ. The difference in the free energy densities in the normal and superconducting phase in the superconductor defines the type of the superconductor.

Because of the positive interfacial (normal–superconductor) free energy density for Type I in the intermediate state (16) (Fig. 3), it is favorable to have a small number of N–S interfaces, ie, to have a small number of the large normal domains. The origin of the negative surface energy in Type II superconductors is presented in Fig. 4. The coherence length is greatly reduced in comparison to the penetration depth, resulting in negative surface energy.

In this case, the appearance of a normal region in the superconducting volume would reduce the free energy. One may expect that the superconducting material would split into a fine-scale mixture of

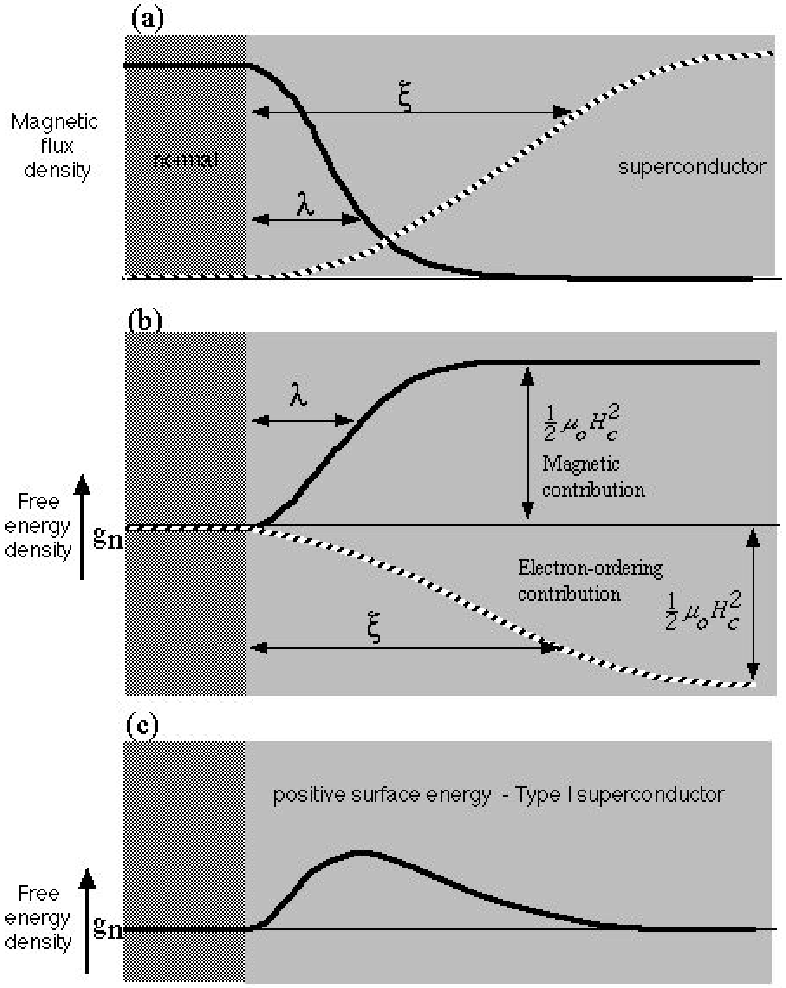

Fig. 3. Schematic of the origin of the positive surface energy in the Type I superconductor at the normal–superconductor interface. The penetration depth λ is shorter than the coherence range ξ and $\kappa < 1/\sqrt{2}$. (After Ref. 16.)

superconducting and normal regions whose boundaries would be parallel to the applied magnetic field. The arrangement provides maximum boundary surface relative to volume of the normal material. Due to the negative interfacial (N–S) free energy density in a mixed state, it is favorable, from the energy viewpoint, to have a large number of as small as possible normal cores in the superconducting medium (16). The consequence of negative surface energy is that in Type II superconductors $> H_{c1}$ there is a mixed state that exists up to higher magnetic fields called the upper critical field, H_{c2}.

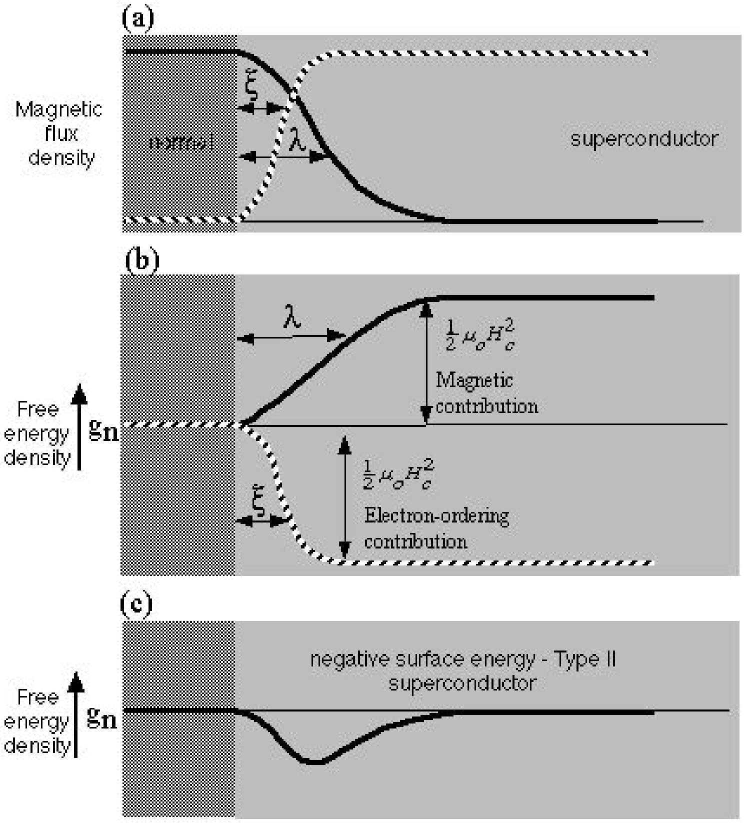

Fig. 4. The schematic of the origin of the negative surface energy in the Type II superconductor at the normal–superconductor interface. The coherence length ξ is shorter than the penetration depth λ and $\kappa > 1/\sqrt{2}$. (After Ref. 16.)

1.7. Critical Fields: H_c, H_{c1}, H_{c2}, H_{c3}

By solving the Ginzburg-Landau equations by the thermodynamic magnetic field H_c can be expressed in equation 11 the general dependence between penetration depth, λ, and coherence range, ξ.

$$H_C(T)\lambda(T)\xi(T) = \text{const} = \frac{\Phi_o}{2\pi\mu_o\sqrt{2}} \tag{11}$$

There is a linear correlation between the thermodynamic magnetic field H_c and the critical temperature T_c of pure elements, as presented in Fig. 5. The value of H_{c2} may be expressed as

$$\mu_o H_{c2}(T) = \frac{\Phi_o}{2\pi\xi(T)} \tag{12}$$

and also in the first approximation:

$$\mu_o H_{c1} = \frac{\Phi_o}{\pi\lambda^2} \tag{13}$$

Table 2. T_c, $B_{c2}(0)$, and γ for a Series of A15 Type Compounds[a]

Compound	Critical temperature, T_c,K	Upper critical flux density $B_{c2}(0)$, T	Electronic specific heat γ,K[T], mJ/K^2-at-g	G–L parameter κ
Nb_3Ge	23.0	38	7.6	
$Nb_3(Al_{0.7}Ge_{0.3})$	21.0	43	8.7	
Nb_3Ga	20.7	38	11.5	
Nb_3Al	19.1	34	10.8	
Nb_3Sn	18.0	32	2.8	34
$Nb_3(Au_{0.7}Pt_{0.3})$	13.0	30	9.0	
V_3Si	17.0	24	13.9	
V_3Ga	15.9	22	24.2	
$YB_2Cu_3O_7$[b]	91	100		

[a] Ref. 17.

[b] $YB_2Cu_3O_7$ high temperature superconducting cuprate.

Taking into account that the magnetic energy of the individual normal zone in a Type II superconductor is a sum of the kinetic energy of a paramagnetic current, the energy of the magnetic field, the exact expression for H_{c1}, has the following form:

$$\mu_o H_{c1} = \frac{\Phi_o}{4\pi\lambda^2}\ln\frac{\lambda}{\xi} \tag{14}$$

By combining equations 11 and 12, the threshold value of κ that defines the type of superconductor can be expressed as follows:

$$H_{c2} = \sqrt{2}\kappa H_c \tag{15}$$

If $\kappa < 1/\sqrt{2}$, ($H_{c2} < H_c$), it is a Type I superconductor. If $\kappa > 1/\sqrt{2}$, ($H_{c2} > H_c$), it is Type II superconductor (15). The simplified relation between the G and L parameter, H_c, H_{c1}, and H_{c2} can be expressed as

$$H_{c1} H_{c2} = H_c^2 \ln\frac{\lambda}{\xi} \tag{16}$$

Therefore, as derived from equation 15, if $\kappa = \lambda/\xi$ is large, then H_{c1} is small and H_{c2} is large. Experimental studies of various superconductors have led to the following calculated values for these two characteristic lengths listed in Table 1. Among all the known pure elements, niobium is one of the few intrinsic Type II superconductors. Simple alloys, eg, NbTi and Nb_3Sn intermetallics, are characterized by the higher κ and also higher T_c (Table 2). In some cases, the B_{c2} at 0 K can be estimated via Hake's empirical formula (17), equation 17.

$$B_{c2}(0) = K\,T_c\left[\frac{\partial B_{c2}(T)}{\partial T}\right]_{T=T_c} \tag{17}$$

1.7.1. Surface Superconductivity

The superconducting layer can persist in applied magnetic fields up to one-third of the critical field, H_{c3}, for materials with $\kappa > 0.42$. At H_{c3}, a superconducting surface layer of thickness $\sim\xi$ can exist and the maximum

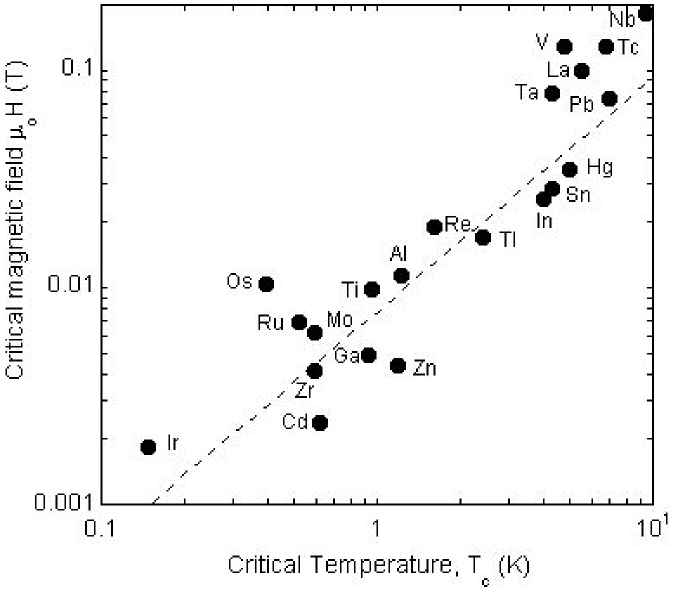

Fig. 5. Thermodynamic critical magnetic fields versus critical temperature for metallic elementary superconductors. Only Nb and Ta are Type II superconductor, the rest are Type I superconductors.

value of H_{c3}, when the applied field is parallel to the sample surface, is given by

$$H_{c3} = 1.69\, H_{c2} \tag{18}$$

As the angle of the applied field to the surface is changed, the value of H_{c3} is reduced monotonically from $1.69 \cdot H_{c2}$ when the field is parallel to the surface and it is equal to H_{c2} if the applied field is perpendicular to the surface. Also, the value of H_{c3} is sensitive to the surface morphology.

1.8. Demagnetizing Effect

In practice, the applied field at which flux penetrates a Type I or II superconductor is usually lower than the H_{c1} value due to the demagnetizing coefficient, N. It is a well-known magnetostatic problem that except for the case of a long thin rod in the parallel magnetic field, the field inside the rod differs from the applied field. A magnetized body produces within itself a demagnetizing field, $H_D = NM$, where M is magnetization that is superimposed on the applied field. The field inside the body H_i can be express as

$$H_i = H_a - NM \tag{19}$$

For the superconductor $M = -H_i$

$$H_i = \left(\frac{1}{1-N}\right) H_a \tag{20}$$

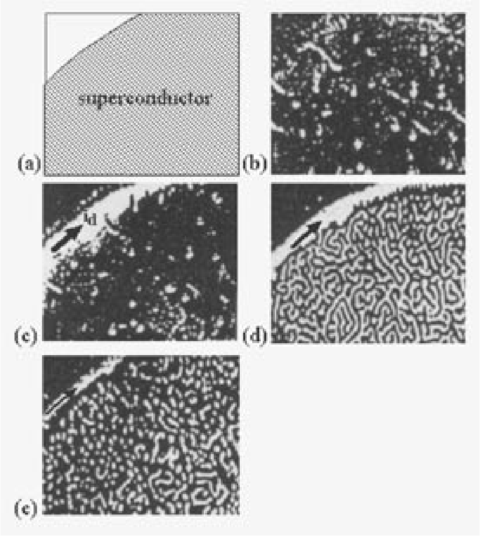

Fig. 6. Magnetoptical flux decoration of the fragment of the flat thin lead disk surface (Type I superconductor in an intermediate state), exposed to a perpendicular external magnetic field at two different stages of the flux penetration: (**a**) outline of the fragment of the superconducting disk; (**b**) $H_{\text{ext}} = 0$; (**c**) increasing magnetic $H_{\text{ext}} \sim 0.17\ H_{\text{c1}}$—high diamagnetic current, i_d, visible at the circumference of the sample; (**d**) increasing magnetic field, $H_{\text{ext}} \sim 0.53\ H_{\text{c1}}$—the amount of the flux in the volume is high so the volume of material in the superconducting state is smaller. Therefore the diamagnetic Meissner current is smaller than in **c**; (**e**) decreasing magnetic field, $H_{\text{ext}} \sim 0.17\ H_{\text{c1}}$—the amount of the flux in the volume is higher than in **c** so the volume of the material in the superconducting state is smaller. Therefore, the diamagnetic Meissner current is comparatively smaller (thin arrow). The width of white circumference represents the density of the diamagnetic superconducting current. The white irregular features indicate the presence of the magnetic flux in the volume of the disk. The initial white pattern in **b** represents imperfection of the magnetooptic coating.

Most of the basic shapes, eg, rods and plates, can be approximated by an ellipsoid with defined axes of revolution corresponding to the length and diameter of the sample. Therefore, it is apparent that for a sphere $N = 1/3$, amplification of the external magnetic strength at the equator is equal to $3/2H_{\text{a}}$, and for a rod perpendicular to the magnetic field $N = 1/2$, amplification of the external magnetic strength at the rod surface is equal to $2H_{\text{a}}$. In the case of the thin film or flat disc in a perpendicular magnetic field, the $N \Rightarrow 0$, so an external magnetic strength at the sample edges can be very high $10^4\ H_{\text{a}}$. Even if a magnetic field compression at the flat sample edges was very high, it would never exceed the H_{c1} value until the applied field H_{a} is smaller than H_{c1} for the given superconductor. This is clearly demonstrated in Fig. 6, where a thin lead disc is exposed to an external perpendicular field.

1.9. The Fluxon Lattice

1.9.1. Type I Superconductors (Intermediate State)

A very important feature of diamagnetic and paramagnetic currents can be revealed by flux decoration. Comparison of the images in Fig. 6 taken for the different values of the magnetic field gives strong evidence for the Meissner diamagnetic current, i_d, which is associated with the external magnetic field, (Fig. 6**c**,**d**). The intensity of the superconducting Meissner current is a function of the external magnetic field, H_{ext} and amount of magnetic flux present in the volume of the superconductor. White irregular features (domains) recorded on the superconductor surface indicate the presence of the magnetic Fluxoid in the volume of the disk that is surrounded by the paramagnetic current i_p. The macroscopic size white dots in Fig. 6**e** do not represent an individual Fluxon Φ_o, as in a Type II superconductor, but a Fluxoid Φ'. However, there is some critical thickness of the superconducting film d, where normal domains of a Type I superconductor may be reduced to a single flux quanta and the material behaves as a Type II superconductor. In such cases, the domain size a decreases with decreasing thickness d of the film (eq. 21), but this is not of practical importance, since the H_{c1} of Type I superconductors is unacceptably low.

$$a = a_n + a_s = [\frac{\delta d}{f(\frac{H}{H_c})}]^{0.5} \tag{21}$$

where $d =$ wall energy parameter; $a_n =$ normal domain size; $a_s =$ superconducting domain size.

1.9.2. Type II Superconductors (Mixed State)

Since the negative surface energy between the normal and superconducting region favors formation of normal zones, which have the largest possible surface/volume ratio, the formation of Fluxons is justified. In the first approximation, the minimum flux density necessary to support one Fluxon in the Type II superconductor can be defined as $\mu_o H_{c1} \approx \Phi_o/(\pi\lambda^2)$. An isotropic flux line consists of a normal core of radius ξ, which is surrounded by a larger region of radius λ, within which the screening currents circulate.

1.9.2.1. Flux Pattern in Type II Superconductors. A mixed state between the Meissner and the normal state is achieved in Type II superconductors with the magnetic field entering as quantized flux lines that occupy only a portion of the volume. This leads to coexistence of a magnetic field and superconductivity in a bulk superconductor up to an upper critical field H_{c2}. Each Fluxon carries one quantum of magnetic flux that is surrounded by a vortex of supercurrents. Due to the natural repulsive forces between neighboring flux lines of the same orientation, the vortices arrange themselves into a triangular Fluxon-line lattice, called the Abrikosov lattice. In such an arrangement, the net forces between vortices become zero. At low flux densities, B, when the distance between Fluxon lines in the Abrikosov lattice is much larger than the coherence length, the mixed-state structure can be obtained from a linear superposition of the fields of individual vortices (18). At high flux densities, the concept of individual vortices breaks down because magnetic field cores of Fluxons merge together and the mean flux density in the superconductor due to the cores and diamagnetic surface current approaches the flux density of the applied field as the magnetic field increases and reaches H_{c2} (19). A Fluxon lattice with triangular symmetry and spacing a_o has an average induction

$$B = n^{'}\Phi_o = \frac{2\Phi_o}{\sqrt{3}a_o^2} \tag{22}$$

where n' is the density of the Fluxons (number of Fluxons, n, divided by sample surface). The vortex spacing at $H \geq H_{c1}$ is $\sim \lambda$, whereas closer to H_{c2} it is proportional to ξ. For example, at $B = 0.01$ T, $a_o = 490$ nm, at $B = 0.1$ T, $a_o = 155$ nm, a very high field of 20 T, $a_o = 11$ nm is comparable with crystal lattice defects.

The high temperature superconductors differ from isotropic conventional metallic superconductors. In addition to their high T_c values, the large spatial anisotropy of these superconductors is striking. The anisotropy is due to the layered crystal structure, which is currently believed to be essential for the existence of high T_c superconductivity. The layers are composed of CuO_2 planes, separated from each other by insulating planes of various other oxides. It is believed, on both experimental and theoretical grounds, that superconductivity and charge transport are mostly confined to the CuO_2 planes (Fig. 7). An increase in and the distance of insulating layers in the cuprate materials weakens the coupling between superconducting CuO_2 planes along the c axis. This decoupling between planes causes the vertical vortex lattice to break into pancakes and strings. Conduction along ab planes is much higher than along the c axis. There is also a significant difference between λ and ξ for different crystallographic orientations in layered HTS superconductor as indicated in Fig. 8.

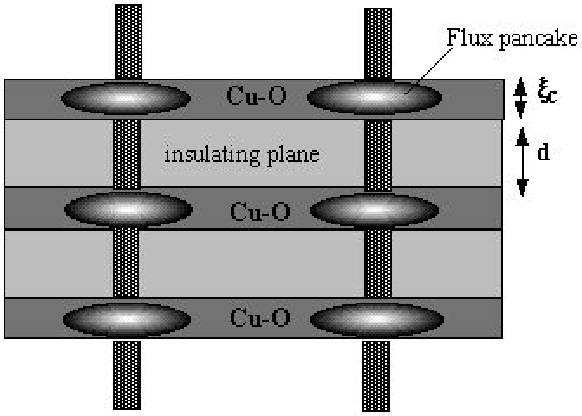

Fig. 7. Schematic representation of the Fluxon lines crossing the CuO conductive layers in high temperature superconductors (HTS).

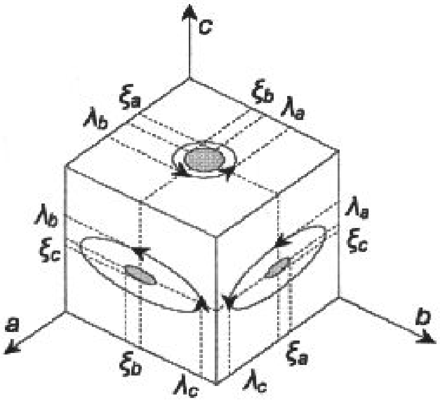

Fig. 8. Schematic representation of screening currents, λ and ξ cores of magnetic flux lines parallel to different crystal axis a, b, c in anisotropic oxide superconductors.

The general solution of the anisotropic Ginzburg-Landau equations provides dependence of the H_{c2} versus angle Θ between the magnetic field direction and c axis as follows:

$$\mu_0 H_{c2} = \frac{\Phi_0}{2\pi(\xi_{ab})^2}(\cos^2\Theta + \epsilon \sin^2\Theta)^{-1/2} \tag{23}$$

where ϵ is a G–L mass anisotropy parameter. The two extreme values for perpendicular and parallel orientation are

$$\mu_D H_{c2(c)} = \frac{\Phi_0}{2\pi(\xi_{ab})^2} \quad \text{for } H\perp ab \tag{24}$$

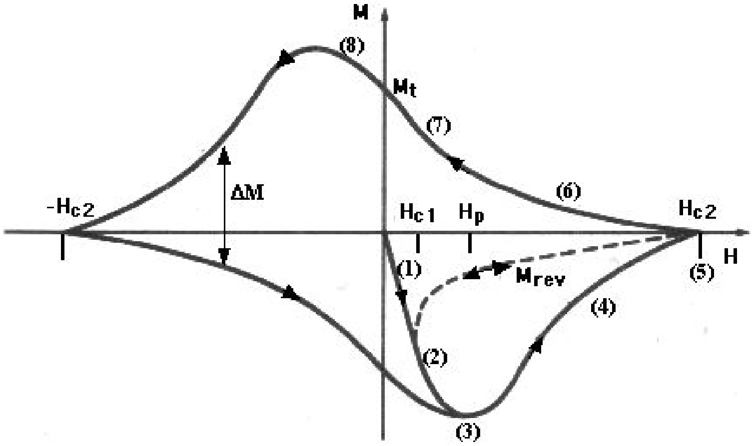

Fig. 9. Hysteretic magnetization loop (solid curve) including the reversible magnetization M_{rev}, superconductor without pinning defects (dashed line).

$$\mu_o H_{c2(ab)} = \frac{\Phi_o}{2\pi \xi_{ab}\xi_c} \quad \text{for } H \perp c \tag{25}$$

and the general dependence between the anisotropic H_{c2}, λ, and ξ can be expressed as

$$\frac{\mu_o H_{c2(c)}}{\mu_o H_{c2(ab)}} = \frac{\xi_c}{\xi_{ab}} = \frac{\lambda_{ab}}{\lambda_c} \tag{26}$$

1.10. Hysteresis Loop, Hysteretic Alternating Current (ac) Losses

There are two distinguishing regions on the –M versus H diagram for the defect free (without pinning) Type II superconductor: (*1*) fully reversible region from $H = 0$ to the lower critical field H_{c1} and (*2*) reversible region represented by dashed curve from H_{c1} to the upper critical field H_{c2}. On reducing the field, this curve will be retraced, and therefore no magnetic flux will be trapped in the volume of the superconductor. In contrast, the imperfect or practical Type II superconductor follows the magnetization curve indicated by the solid line. In this case, there are three distinguishable regions of the different behavior of a superconductor in the external magnetic field. The first reversible region is from $H = 0$ to H_{c1} point 1 in Figs. 9 and 10. In this region below H_{c1}, no flux penetrates the volume. The shielding is done by the diamagnetic supercurrent, i_d (see also Fig. **1a**), the bulk of the sample does not see any field. The second, (irreversible) region is from H_{c1} to H_p in which flux penetrates the volume of the superconductor as indicated by points 2 and 3 in Figs. 9 and 10. A surface current still remains, but the magnetic field now penetrates to a certain depth below the surface. This flux is pushed in against the pinning forces. The third region from H_p, point 4 (which does not represent intrinsic material property, but depends on the sample geometry and the pinning strength), and the upper critical field H_{c2}, where the whole specimen sees the field and magnetic flux, fully penetrates the superconductor. At H_{c2}, point 5, the superconductor became ordinary normal material.

After reduction of the magnetic field to zero, points 6 and 7, some of the flux will remain pinned in the sample by defects. Generally, the higher the remanent magnetization M_r, the higher the critical current capabilities of the superconductor. After reversing the applied magnetic field, point 8, flux lines with opposite orientation enter the sample. The remaining flux lines are attracted by the new penetrating antiflux lines.

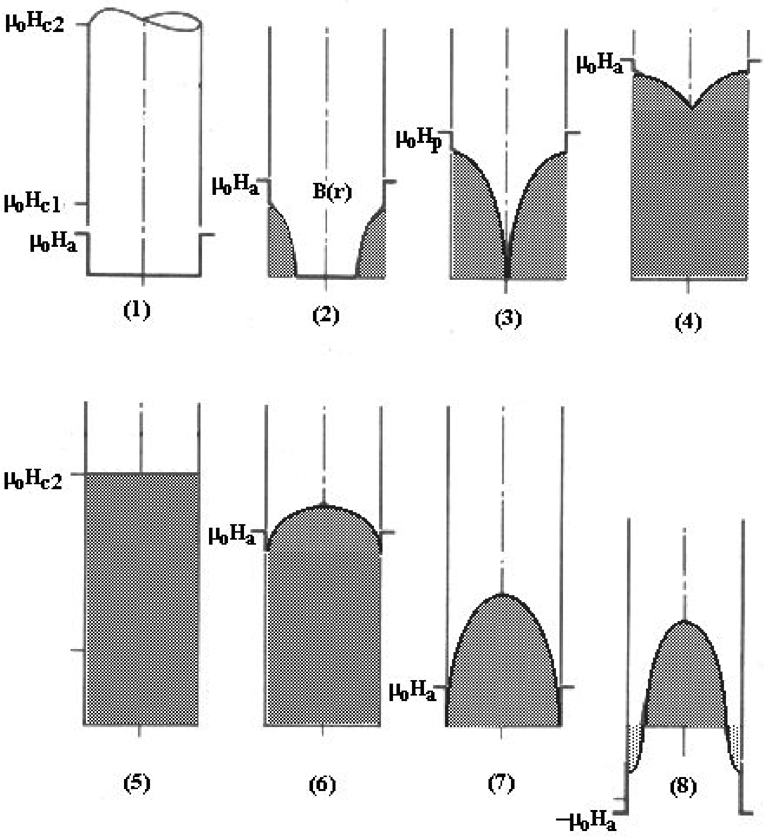

Fig. 10. Local flux-density profile, according to the critical state model, in a slab for increasing and decreasing applied field H. The characteristic points are marked accordingly to the hysteretic loop presented in Fig. 9.

Figure 11 represents an individual Fluxon and anti-Fluxon emerging from the flat superconductor into the free space observed outside the superconductor where there is no quantization of the flux. Fluxon spreads into the free space in the shape of a tornado (20). Because of the attracting force between Fluxon, which was previously established in the superconductor, and anti-Fluxon entering superconductor, they must join together in a free space as shown in Fig. 11**b**, and if there are no other forces to stop their progress toward each other they will annihilate dissipating the energy (Fig. 11**c-d**). This case is most likely associated with the magnetic hysteresis loop. The full reordering and annihilation process continues until all flux remaining from previous magnetization is dissipated. The full hysteresis loop (Fig. 9) represents the energy loss in the superconductor per cycle (eq. 27).

$$W = \oint_{\mathrm{S}} H\,dM \tag{27}$$

Electromagnetic losses occur in superconductors when they are exposed to time-varying fields or currents. Despite the different shapes of hysteretic loops for the given imperfect Type II superconductor, the following characteristic points on the irreversibility loop are identified as lower critical field, H_{c1}, penetration field, H_{p} (which does not represent the intrinsic material property, but depends on the sample geometry and the

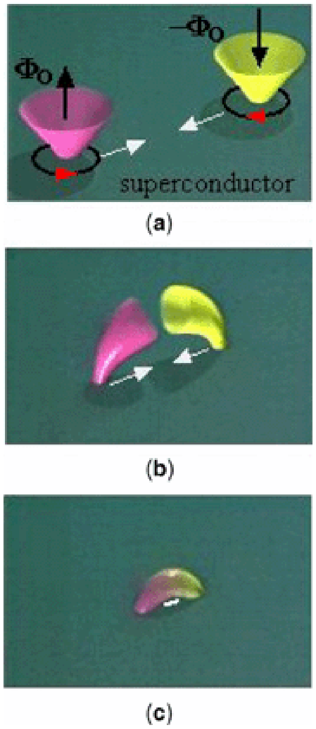

Fig. 11. Simulation of the sequence of events taking place in point 8 in Figs. 9 and 10, as Fluxon Φ_o and anti-Fluxon -Φ_o, annihilation takes place. Such annihilation is associated with energy dissipation, and discharge of the two paramagnetic currents to zero, which has consequences in a magnetic hysteresis (Fig. 9). Paramagnetic currents are marked as black rings around fluxons (**a**) and as a one discharging ring in (**c**). White arrows point out directions of the fluxons movement.

pinning strength), upper critical field, H_{c2} (full penetration), and remanent magnetization, M_t. Hysteretic loss in superconductors is a very important physical practical parameter, defining not only the strength of the pinning, but also the actual hysteretic losses per cycle. To define losses at higher frequency, losses per cycle have to be multiplied by the number of cycles per second. In real conductors, the total losses are the sum of the hysteresis component, the coupling currents in the resistive matrix, etc.

1.10.1. High Frequency Losses

Superconductors show zero resistance for direct current the frequency alternating currents are not too high. The frequency at which resistance begins to appear corresponds to the microwave or long-wave infrared (ir) portions of the spectrum. The characteristic frequency where resistance begins to appear for a particular superconductor depends on the temperature. The surface resistance of $YBa_2Cu_3O_{7-d}$ films measured at ~ 90 GHz, at 77 K, is reported to be $R_s < 8\,\mathrm{m}\Omega$. It is at least an order of magnitude below that of copper at the same temperature and frequency. There is some interest in the utilization of high T_c materials and MgB_2 in an accelerator cavity. The intergranular critical current density, J_c, dependence on magnetic field, H_s, surface resistance, R_s, and frequency, f, can be expressed as

$$J_c\,[\mathrm{A/cm^2}] = \frac{0.167\, f(\mathrm{GHz})}{R_s\,[\Omega]/H_s(\mathrm{A/m})} \tag{28}$$

1.11. Irreversibility Field

Soon after the discovery of high temperature superconducting cuprates it became clear that their mixed-state properties were different from those of classical 3D superconductors. The most striking early observations were (*1*) the existence of a so-called irreversibility line, which separates an extended range in the H–T plane where the magnetization is reversible from a magnetically irreversible state (21); and (*2*) the pronounced broadening of the resistive transition in a magnetic field (22). Like the giant flux creep phenomenon, it was established that there is a significant temperature range below the superconducting transition temperature, $T_{\mathrm{irr}}(H)$, in which the magnetization of a bulk superconductor is reversible during a warming and cooling cycle in the magnetic field and can be described as

$$H_{\mathrm{irr}} \propto [1 - \frac{T_{\mathrm{irr}}(H)}{T_c(\mathrm{o})}]^{3/2} \tag{29}$$

The existence of a reversible superconducting region above the irreversibility line, where flux pinning is ineffective and thus the transport critical current density, J_{c}, is zero. In a state above the irreversibility line high T_c, superconductors cannot carry a supercurrent because of freely movable flux lines, and thus become useless for applications. One interpretation of the irreversibility line is the thermally activated flux flow model stating that the irreversibility line represents a crossover from a pinned flux creep state to a depinned flux flow state when the thermal energy $k_{\mathrm{B}}T$ becomes comparable with the pinning energy. In this sense, the irreversibility line is a depinning line. The irreversibility line defines the applicability of the given superconductor. Additionally, the anisotropic HTS also possesses anisotropic H_{irr} for different orientation of the magnetic field with respect to crystallographic directions $H_{\mathrm{irr}}\ (ab)/H_{\mathrm{irr}}(c) > 10$. However, the class of materials known as a HTS are characterized by a high T_c and a very high upper critical field, H_{c2}. The resistive transition is broadened considerably by many tens of degrees with an applied field, which is in contrast to metallic superconductors for which resistive transition is always very sharp to temperatures closest to T_c and with high fields. The behavior of HTS is a direct result of finite resistance because of vortex motion by either flux creep, thermally activated flux flow (TAFF), or by flux flow in proximity to the irreversibility line.

The irreversibility line is not unique to high T_{c} superconductors, although less distinctly, but also exists in conventional metallic superconductors. Suenaga and co-workers (23) investigated the irreversibility line in low temperature superconducting NbTi and $\mathrm{Nb_3Sn}$ wires. They found that these materials have a clear irreversibility line that is lower than the superconducting phase line $H_{\mathrm{c2}}(T)$. They also found their H_{irr} data fit well to a flux lattice melting line (24), and thus they interpreted the observed irreversibility line as a flux lattice melting line. The irreversibility field H_{irr} as a function of temperature can be defined by four methods: (*1*) as the field over which the magnetic hysteresis becomes undetectable on the M–H loops versus temperature; (*2*) as a zero resistance versus magnetic field; (*3*) as a change in a susceptibility versus magnetic field; and (*4*) as a zero critical current versus temperature.

1.12. Critical Currents and Voltage and

Fundamental superconducting parameters, eg, the magnetic penetration depth, λ, the coherence length, ξ, the critical fields (H_{c}, H_{c1}, H_{c2}), the G–L parameter, (κ), and critical temperature, T_c are intrinsic superconducting material properties. Structural ordering of the superconducting phase improve T_c (25), but may not coincide with the highest transport properties of the superconductor, eg, a critical current. The parameters defining the applicability of a superconducting conductor, eg, upper critical field, H_{c2}, critical temperature, T_c, and the critical current density, J_{c} (which is defined as the critical current I_{c} divided by the cross-sectional area S of the superconductor) are interrelated. They also are strongly dependent on the microstructure of the superconductor. The picture becomes more complex in the case of superconducting oxide cuprates, where thermally activated flux flow is very pronounced and the two dimensional aspects of the superconducting structures are apparent.

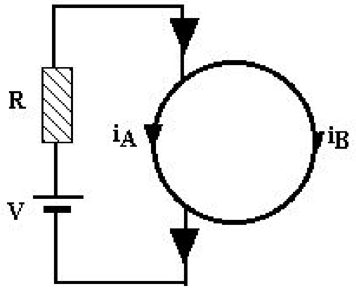

Fig. 12. Schematic division of transport superconducting current between two parallel paths.

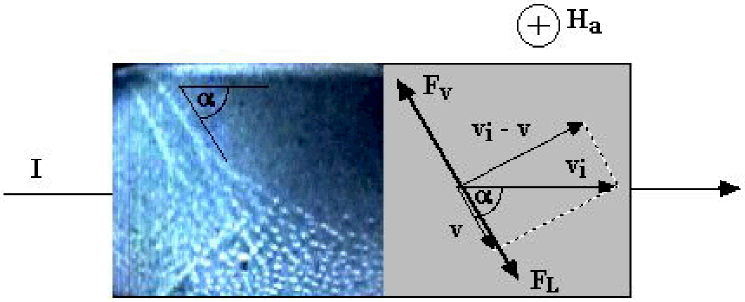

Fig. 13. Velocity and force diagrams for flux motion in the defect free flat superconductor in the applied magnetic field are directed into the plane of the sample. Left top part of the superconductor reveals the Fluxons entering from the edge of the defect free sample (no pinning). Velocity of the electrons carrying the transport current I is represented by v_{i}, and v is the velocity of a Fluxons through the material. The parameter F_{L} is the Lorentz force and F_{v} is viscous drag force.

A superconductor at a temperature of $T > 0$ can be regarded as consisting of two interpenetrating electron fluids: the normal electrons (quasiparticles) and the superelectrons. In the case of transport direct current (dc), all the current is carried by superelectrons. If the current is to remain constant, there must be no electric field in the metal, otherwise the superelectrons would be accelerated continuously in the electric field and the current would increase indefinitely. If there is no field, there is nothing to drive the normal electrons, and so there is no normal current. The consequence of zero resistance is that the fundamental Kirchhoff's law is not obeyed. However, the two resistanceless branches of different length presented in Fig. 12 contribute by inductance to the circuit inductance. The currents in the parallel resistanceless superconducting paths are inversely proportional to the self-inductances of those paths. It can be expressed by the following equation:

$$\frac{i_A}{i_B} = \frac{L_B - M_{AB}}{L_A - M_{AB}} \tag{30}$$

In the case of applied ac current due to some finite mass of electrons, the supercurrent lags behind the field. Hence, the superelectrons present an inductive impedance and because there is an electric field present, some of the current is carried by the normal electrons, and therefore, there is inevitable resistance resulting from electrons scattered on the crystal lattice of the superconducting material.

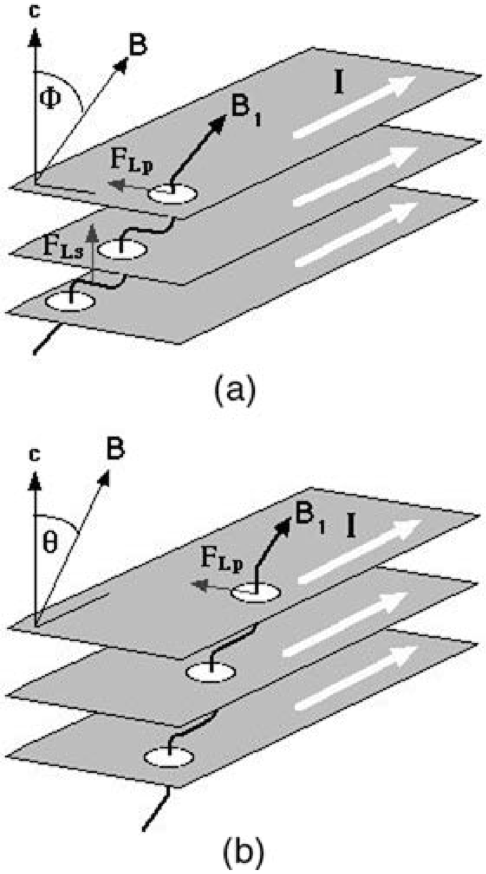

Fig. 14. Details of the flux line components penetrating superconducting Cu–O layers; (**a**) for $\theta = 0^\circ$ and $\Phi > 0^\circ$, Lorentz forces act on pancake vortices ($F_{\mathrm{L}P}$) and on the strings (F_{LS}), (**b**) for $\Phi\kappa = 0^\circ$ and $\theta > 0^\circ$, F_{L} act only on the pancake vortices ($B_1 =$ the local field, $B =$ the field averaged over a few Cu–O layers). The small circles symbolize shielding currents of pancake vortices.) (After 48).

1.12.1. V-I Characteristics of S–I–S Junctions

Superconducting devices based on tunneling of the quasiparticles or Cooper pairs, posses a unique and often complex voltage current characteristic. This characteristic has its origin in quantum phenomenon (26). Josephson mathematics (27) predicted that if there is a small gap or even an insulator between two superconductors, a superconducting current can be conducted across such a superconductor–insulator–superconductor, S–I–S, junction in the form of Cooper pairs, because of the proximity and quantum mechanical tunneling effect. This is called a Josephson junction. The electron transport across such a barrier is more general and the tunnel current consist of two parts. The first arises from the tunneling of Cooper pairs and the second comes from the tunneling of quasiparticles. This first term leads to the so-called Josephson effect. Once the magnetic field is applied, this stops superconducting electron Cooper pairs from tunneling through the barrier. If some voltage is applied across the junction, quasiparticle tunneling current takes place. Quasiparticles in a superconductor have both electronlike and holelike characters. Each time a quasiparticle crosses the barrier, an electron charge is transferred. The voltage current, *V*-*I*, characteristic of the S–I–S tunnel junction is dramatically different for these two parts of the tunnel current. The Cooper pairs tunneling characteristic is defined by the McCumber

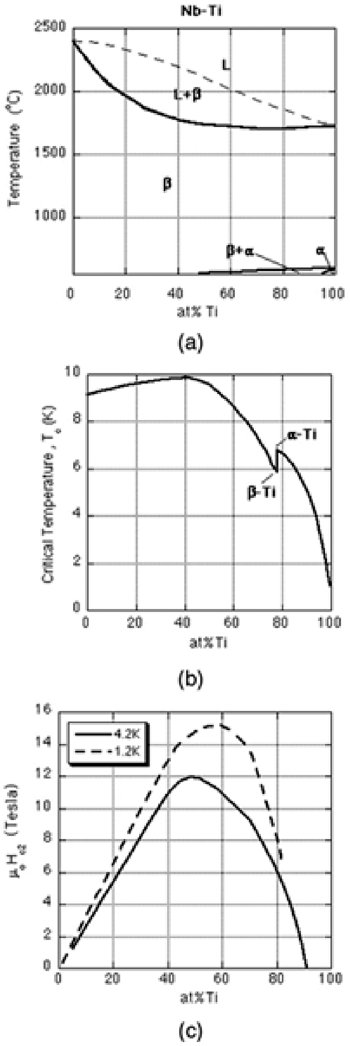

Fig. 15. Data on the Nb–Ti alloy versus at% of Ti: (**a**) binary-phase diagram of the Nb–Ti alloy; (**b**) critical temperature, T_c; (**c**) upper critical field H_{c2}.

parameter, β_c.

$$\beta_c = \omega_c \mathrm{CR_n} \tag{31}$$

$$\text{where } \omega_c = \frac{2eI_c R_n}{\hbar} \tag{32}$$

Practical junctions are usually described by resistively and capacitively shunted junctions, RCSJ. In most cases, this correctly describes the relationship measured qualitatively and quantitatively at the terminals between the current and voltage. Josephson junctions with an S–I–S structure have a nonvanishing capacitance $C \neq 0$

and a voltage-dependent nonlinear resistance $R(U)$. Under these conditions the calculation of the RCSJ model becomes quite complicated. In general, LTS Josephson tunnel junctions always show hysteresis. The HTS and LTS, S–I–S junctions that exploit the quasiparticle tunneling and not the Copper pair tunneling are suitable for detectors and mixers in the millimeter wave region when specially high sensitivity is required. In radioastronomy, S–I–S mixers are routinely employed. The S–I–S junctions that exploit the Copper tunneling, not quasiparticle tunneling, are suitable for use in superconducting quantum interference devices, SQUID, which are the most sensitive detectors of magnetic flux available. There is a simpler version of such a junction, the S–I–N junction, where N stands for normal metal. In this case, the onset on the voltage axis takes place at $U = \Delta/e$ and a derivative of the V–I curve gives superconductor density of states value, $dI/dV \sim \mathrm{Ns(E)}$.

1.12.2. V-I Characteristics of S–N–S Junctions

The S–N–S junction involves phenomena, eg, the proximity effect related to the coherence length (28) and also Andreev reflection (29). Andreev reflection is the mechanism by which current enters a superconductor from a normal contact. The S–N–S voltage–current characteristics are similar to that of the Cooper pair S–I–S junction, and to some extent to that of the discontinous multifiamentary S–N–S superconducting conductors (30). The main disadvantage of S–N–S junctions is their relatively low I_cR_n product, so sometimes S–I–N–I–S junctions are used. Therefore, the advantage of S–N–S junctions is a remarkably low parameter spread. There are other exotic types of junctions, eg, S–Se–S where Se stands for the semiconductor to integrate low temperature semiconducting circuits into superconducting SFQ circuits (31).

1.12.3. Critical Current, I_c and Critical Current Density, J_c

Both T_c and B_{c2} are important superconductor parameters, but critical current density, J_c is a key parameter in determining the use for many engineering and electronic applications. Although the critical temperature, T_c, sets an upper limiting temperature for the possible exploitation of a superconducting material, it is the value of J_c that determines the practical prospect for real engineering applications. In general, the material microstructure needs to be precisely controlled to achieve a high J_c. The perfect defect free superconductor characterized by highest T_c and B_{c2} may possess a very low critical current due to the lack of pinning centers that are, in most cases, represented by the dashed line in Fig. 9. The critical current I_c is defined as the maximum electrical current below which a superconductor exhibits superconductivity at some given temperature and magnetic field. The critical current is usually defined by means of an electric field criterion or resistivity (32). Critical current is the value of the current defined by the voltage generated by the movement of flux lines along the specified length of conductor. A usual I_c value used in industry is $E = 10^{-7}$V/cm. Practical superconductors commonly display a power low resistive dependence $V = kI^n$ or $E = kJ^n$, where k is a constant. Values of the power n are easily determined on a log–log plot of the slope of V–I or E–J curves. Values of n generally lie between 20 and 100 for high current practical superconductors (33). Lower n values usually indicate inhomogeneities in the local current densities (34). The critical current is also strongly dependent on applied magnetic field magnitude and direction. Typically, I_c values are prescribed at one or more magnetic fields, usually for the magnetic field applied perpendicular to the wire axis. This particular orientation of the magnetic field corresponds to the lower I_c values, but it is the most common orientation in magnet applications, where generated magnetic field by the superconducting coil is perpendicular to coil windings. The actual shape and sensitivity of the full E–I characteristic of high pinning practical superconductors very much depends on the sample length and configuration in the magnetic field.

Alternatively, resistive criteria of $\rho = 10^{-13}\,\Omega\,\mathrm{m}$ are sometimes used for commercial conductors as they relate directly to the energy dissipation in a particular device. The value of the maximum current density of a practical Type II superconductor, at which the depairing of the Cooper pairs take place and destroy

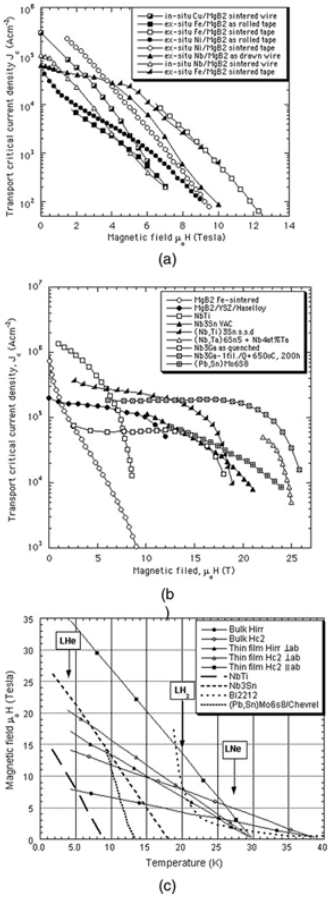

Fig. 16. Comparison of the critical parameters for MgB_2 conductors and LTS superconductors: (**a**) critical current density versus applied field for MgB_2 wires and tapes at a temperature of 4.2 K; (**b**) Comparison of the critical current density versus external magnetic field for the range of low temperature superconducting conductors including MgB_2 manufactured by different processes as specified in the legend. For an MgB_2 coated conductor (67) the magnetic field was parallel to the tape surface. In all cases, the magnetic field was perpendicular to the current, data for Nb_3Ga, $T_c = 14.5$ K; (Courtesy of Prof K. Inoue, National Institute for Materials Science, Tsukuba Magnet Laboratories, Tsukuba, Japan) (62); (**c**) Cumulative plot of upper critical field H_{c2} and irreversibility field H_{irr} versus temperature for MgB_2 bulk and thin films compared to other conductors, eg, optimized alloy NbTi, intermetallic Nb_3Sn, Chevrel-phase $PbSnMo_60_8$ and oxide ceramic $Bi_2Sr_2CaCu_2O_{8+d}$ after improvement of H_{c2} and H_{irr} is associated with degradation of the T_c. Data for the best MgB_2 wires and tapes are located between Bulk H_{irr} and Bulk H_{c2} curves. Also shown are isotherms for cryogens < 30 K (vertical arrows). (Data for MgB_2 from Ref. 176, for films, and for bulk MgB_2) (69,73).

superconductivity, can be estimated from the G–L equation as:

$$J_c \approx \frac{H_c}{\lambda} \tag{33}$$

In metallic Type II superconductor characterized, eg, by $\mu_o H = 0.1$ T and $\lambda \sim 100$ nm, the critical current density value at which Cooper pairs are broken up can be estimated to be $J_c \sim 10^8$ A/cm^2. The experimental data for applied metallic low temperature superconductors show that the maximum values are lower, $J_c \sim 10^6$–10^7

A/cm^2. The experimental results reported for $YBa_2Cu_3O_7$ high temperature superconducting bridges prove that critical current density value measured at 77.4 K can be as high as $J_c \sim 10^9$ A/cm^2 (35). Such high critical current density in high temperature superconducting narrow bridges is not presently fully understood, but may be due to vortex-ring creation.

The shape of the flux lines is strongly affected by the superposition of the self-field with the externally applied field. There are three regimes: (*1*) pure self-field regime $H_{\text{self}} \gg H_{\text{ext}}$; (*2*) low external field regime comparable to self-field $H_{\text{self}} \sim H_{\text{ext}}$, and (*3*) high magnetic field regime $H_{\text{self}} \ll H_{\text{ext}}$. The equilibrium FL is only found in single-crystal samples in a uniform applied field when the transport current is zero. Otherwise, FL is invariably distorted and can be defective. Where samples are too small for transport measurements, if the superconductor-normal metal contact resistance is too high or the current transfer from the matrix to superconductor is to long, or the superconductor is in powder form or multiphase with discontinuous superconducting paths, it is then possible to estimate the critical current density from the hysteresis loop (see left part of hysteresis loop in Fig. 9). In this case, the magnetic intragrain critical current density, $J_{c,\text{mag}}$, can been estimated from the Bean model (36) for solid superconducting samples. A formula for an infinitely long rod of a rectangular cross-section ($2a_1 \times 2a_2$, where $a_1 \geq a_2$) in a magnetic field parallel to the infinitely long axis has the following form (37):

$$J_{c,\text{mag}}(H) = \frac{\Delta M(H)}{a_2(1 - \frac{a_2}{3a_1})} \tag{34}$$

where $M(H)$ is the width of the magnetization characteristic at an applied magnetic field $H > H_p$, see Figs. 9 and 10. For an infinitely long cylindrical rod in a parallel magnetic field, $a_1 = a_2$ and reduces to

$$J_{c,\text{mag}}(H) = \frac{3\Delta M(H)}{2a} \tag{35}$$

where a = radius of the cylinder (SI units). For the granular system and the shorter samples, the constant in equation 35 can be different (38,39).

1.12.4. The Engineering Critical Current

A low value of the overall critical current density, J_e, is a particular problem with fully engineered conductors. The thickness of nonsuperconducting layers and the usual deterioration of J_c in the superconductor with increasing thickness t_s leads to a maximum in J_e with t_s, which can be expressed as

$$J_e(t_s) = J_c(t_s)\left(\frac{t_s}{t_s + \sum_{i=1}^{n} t_i}\right) \tag{36}$$

where

$$J_c(t_s) = J_c(t_s \approx 0) t_s^w e^{k \cdot t_s} \tag{37}$$

$J_c(t_S \approx 0)$ is a current density independent of thickness for $w = 0$ and $k = 0$; parameter w defines the maximum position on the $J_c(t_S)$ curve, where the k parameter defines the J_c versus t_s dependence and $\sum_{i=1}^{n} t_i$ is a sum of the thicknesses of the substrate, buffer layer, diffusion barrier, matrix, stabilizing (shunt) layer, insulating layer, etc (excluding superconductor). The shape of $J_c(t_S)$ dependence possess the maximum for Nb_3Sn conductors (25), but monotonic decay for thin and thick HTS films prepared by doctor blading and sputtering techniques, where a liquid-phase epitaxy of $YBa_2Cu_3O_{7-\delta}$ is characterized by an increasing function. It is important to take into account the correlation between J_c and J_e versus the superconducting layer thickness, t_s, with respect of the optimum property of the final conductor (40). From an applications point of view, the most optimum superconducting layer thickness is where the maximum of the J_e is reached, and not necessarily where the highest J_c of the superconducting layer is found.

1.12.5. Flux Flow in Superconductor

In the mixed state, the superconducting current flows throughout the whole body of the Type II superconductors. The superconducting material is threaded by the magnetic flux associated with the normal cores of Fluxons. There is an electromagnetic force (Lorentz force, F_L) between these Fluxons, and the superelectrons carrying the transport current if the magnetic field is applied in the presence of the transport current. The F_L parameter acts at right angles to both the direction of the transport current and the direction of the Fluxons. The voltage, which appears when the transport current exceeds the critical value, I_c, can be associated with the work required to drive the normal cores through the superconductor. For a given current the voltage is independent of time, which implies, that the core lattice is not accelerating under the forces that act on it, but moves with constant velocity. This implies that the superconductor behaves as a viscous medium as far as motion of the cores is concerned. The electrical flow resistivity does not depend on the composition and perfection or imperfection of the superconductor. If a “viscosity constant” η is ascribed to each material and there is a net force F per unit length acting on a normal core, the core will acquire a velocity $\upsilon = F/\eta$.

Consider the special case when the applied magnetic field is perpendicular to the direction of transport current flow. If the cores are held stationary in the superconductor, the relative velocity between the cores and the electrons carrying the transport current has a certain value, and F_L force tends to detach the vortices from their pinning sites. This force is perpendicular both to the transport current and to the axis of the cores. When, however, the cores have been set in motion, there is a different relative velocity between them and the electrons carrying the current, so the force acting on them is changed. Note that the vortices encircling the cores represent a circulatory motion of the superelectrons. This motion is superimposed on the linear motion produced by the transport current, and in the absence of any other forces the vortices are carried along by the transport current with the velocity v_i of its electrons (Fig. 13). If this happened there would be no relative motion of the vortices and transport current electrons, and therefore no F_L on the vortices. However, as seen, the appearance of a voltage suggests that there is opposition to the motion of the vortices through the metal, and now, as a result, the vortices acquire a component of velocity at right angles to the transport current.

It is important to realize that when the cores are in motion, the magnitude and direction of the forces acting on them are different from when they are held stationary in the material. The direction of the vortex motion is found when the transport current is raised above the critical value, so that the vortices become detached from the pinning centers. If in the steady state, the vortices move through the superconductor with a velocity v, which is constant. The forces on them must balance. These forces are illustrated in Fig. 13. The superconductor exerts a viscous drag on vortices moving through it, so there will be a force F_v acting in a direction opposite to the vortex velocity v:

$$F_v = \eta v \tag{38}$$

The electrons of the transport current have a velocity (v_i-v) relative to the core of the vortex and this produces, at right angles to (v_i-v), the F_L that drives the vortices in the direction v (see Fig. 13). The magnitude of F_L is given by

$$F_L = |v_i - v| n_s e \Phi_o \tag{39}$$

where n_s is the number of superelectrons per unit volume that related to l by the following relation: $n_s = 1/l^2$. For the velocity of the vortices to be constant, F_{L} must equal $-F_{\mathrm{v}}$, which from equations 38 and 39 yield

$$|v_i - v| = \frac{\eta v}{n_s e \Phi_{\mathrm{o}}} \tag{40}$$

and the angle α that the vortex motion makes with the transport current is defined as

$$\alpha = \tan^{-1}\{\frac{\eta}{n_s e \Phi_{\mathrm{o}}}\} \tag{41}$$

This shows that the greater the viscous drag exerted by the metal on the vortices (the bigger the value of η) the closer the vortices will move at right angles to the transport current. Measurements on practical Type II superconductors, eg, NbTi and Nb_3Sn, showed that α is close to 90°, which implies that the viscous drag is large. Hence, when flux flow occurs the vortices move virtually at right angles to the direction of the transport current. In defect free Type I and II superconductors, the angle α has a value of $\sim 60^\circ$, which reflects the lower flux viscosity in the superconductor because of lack of pinning centers, as presented in Fig. 13.

1.13. Lorentz Force and Pinning Force

Point defects, impurity phase, secondary phases, voids, cation vacancies, oxygen vacancies, twin structure, etc, are the effective pinning centers of the quantized flux lines and flux lattice. The pinning center is at its most effective if it has a size comparable to the coherence length, ξ. Therefore, the difference of free energy at the normal core and superconducting region is the highest. Due to such a lower energy state in the pining center, Fluxoid $n\Phi_{\mathrm{o}}$ or Fluxon Φ_{o} remain pinned by pinning centers as long as the F_{L} per unit volume is lower than the pinning force, F_{p}. Flux lines begin to move when F_{L} exceeds F_{p}, which defines the critical current density J_{c}.

$$\begin{gathered} -F_P = F_{\mathrm{L}} = J_c \times B \\ (\mathrm{N/m^3} = \mathrm{A/m^2 \cdot Vs/m^2}) \end{gathered} \tag{42}$$

F_{L} is an electromagnetic force (F_{L} between the flux and the current). Not every individual core is directly pinned to the material, but the interaction between the vortex currents is sufficient to give the lattice of Fluxons certain rigidity. If on the other hand only a few cores are pinned, the whole pattern is immobilized. What matters, therefore, is the average pinning force per core. The parameter F_{p} is an average pinning force per unit length of the core. If the transport current is increased to the critical current value, J_{c}, F_L exceeds F_{p} and the flux line lattice is no longer prevented from moving through the superconductor.

In technical Type II metallic superconductors, the pinning force is exerted on Fluxoids as a result of the presence of inhomogeneities, eg, microscopic precipitates, dislocations, stacking faults (41), or grain boundaries (42). This is the case when high angle grain boundaries are the dominating source of the pinning centers in intermetallic Nb_3Sn superconductors because the width of the typical grain boundary in polycrystalline Nb_3Sn is comparable with the coherence length, ξ. In the available oxide superconductors, F_{p} is much smaller than that in the practical metallic superconducting materials. Taking into account the very large values of λ in the HTS, the nonuniformities comparable to λ are not effective pinning centers in the cuprate superconductors. An effective pinning center has an effective dimension of ξ. The energy to destroy superconductivity, the condensation energy, is equal to $H_{\mathrm{c}}{}^2/8\pi$ per unit volume, where H_{c} is the thermodynamic critical field. Therefore, if there is, eg, a nonsuperconducting precipitate of volume ξ^3, an excess energy of $\xi^3 H_c{}^2/8\pi$ is required to push a flux line out of the precipitate (43). Although the value of H_c, is larger for the cuprates than for conventional metallic superconductors ($H_c = 3$ T for $YBa_2Cu_3O_7$, and 0.2 T for Nb at 0 K), the value of ξ^3 is much smaller in cuprates, 5×10^{-27} m^3 versus 6×10^{-23} m^3, respectively. Hence, the pinning energy could be smaller in the cuprates than in Nb by a factor of 10. The pinning energy thus calculated is as small as 0.1 eV for $YBa_2Cu_3O_7$, whereas it is 100 eV for Nb at 0 K. Furthermore, $\xi^3 H_c{}^2/8\pi$ scales with temperature as $(1-T/T_c)^{0.5}$, resulting in the estimation of the pinning energy at 77 K for $YBa_2Cu_3O_7$ of ~ 0.04 eV. Since the thermal energy at 77 K is 0.006 eV, the pinning energy obtained may not be large enough to prevent the thermally activated depinning process (44,45).

In high temperature superconductors, due to weak coupling through the insulating layers between superconducting CuO_2 planes along the c axis in the cuprate materials, there is an expected variation in the preferential flux line position for the magnet parallel to ab planes.

Takichi and Takahashi (46) considered a variation of the order parameter in the c direction with a periodicity of the lattice constant, c. They further argued that this modulation of the order parameter generates a periodic potential for Abrikosov vortices parallel to the ab plane. If the core of the flux line is located in between two CuO_2 double layers, where the order parameter is already reduced, the loss of condensation energy is smaller than when the flux core is placed in a CO_2 layer. The gradient of this potential generates force on the flux lines, which is an intrinsic pinning force, because the effect is intrinsic to the crystal structure. Intrinsic pinning depends strongly on the ratio of ξ_c to the c axis. It was calculated that the maximum pinning force occurs for $\xi_c/c \approx 0.3$ and a rapid decrease takes place for larger values. Above $\xi_c/c \approx 1$, the effect becomes negligible because the strength of the modulation decreases and because each flux line core contains several CuO_2 double layers, where gradients of the opposite sign add up to only small effective forces. The volume pinning force derived from intrinsic pinning can be large because all flux lines are pinned coherently along their full length if they are parallel to the ab plane. Therefore, it is essential to align the microstructure of HTS along the ab plane for high current applications.

1.13.1. Complex F_L in Layered HTS

The structure of F_L in layered HTS superconductors greatly depends on the direction of the applied field. For B perpendicular to the superconducting layers, the order parameter between the layers is strongly suppressed leading to reduced coupling between layers and the formation of superconducting 'pancakes' in the CuO planes, Fig 7. Pancakes in the superconductors with closer CuO_2 planes are in the form of flat discs, whereas in the materials with a larger distance between Cu–O planes, they are of the ellipsoidal shape, Fig. 8, and the volume $\sim(\xi_{ab}{}^2\xi_c)$. Also, they are easily thermally activated. The Lorentz force consists of pancake Fluxons coupled magnetically and also by proximity currents in the region between superconducting layers (47). For B parallel to the layers, the structure of FL is complex. If the superconducting layers are coupled, the Fluxon core will be entirely in the nonsuperconducting region and will cease to display a line singularity in the order parameter. Such a Fluxon is termed a Josephson vortex. The order parameter is high in the superconducting layers, but is strongly suppressed between them where the superelectron density is low. The nature of the vortex structure when the vortices are at some angle to the conductive CuO planes is still the subject of research, but a Fluxon line can be regarded as a sequence of pancake vortices interconnected by Abrikosov vortices or Josephson string, depending on the operating regime (48). Therefore, a vortex line can be regarded as a sequence of pancake vortices interconnected by Abrikosov vortices or Josephson string, depending on the operating regime. Lorentz forces act on pancake vortices and/or on the strings depending on the I_c versus B orientation as shown in Fig. 14.

1.14. Global Pinning Force Scaling

In most high pinning Type II superconductors, it has been observed that the pinning force shows a maximum in the F_p versus B plot. The global pinning force frequently exhibits scaling behavior with reduced field $b = B/B_{c2}$, where constant and G is a geometrical function of the microstructure, equation 36. Usually, this is interpreted as a surface area of inclusion per unit volume of matrix. The significance of this equation is that if one measures

F_p versus b at one temperature, then F_p at other temperatures can be predicted by scaling the results with a factor $[B_{c2}(T)]^\mathrm{n}$.

$$F_p = J_c B = G[\frac{(B_{c2}(T))^n}{k^m}]\, f(b) \tag{43}$$

where n and m are fitting parameters and

$$f(b) = b^p(1-b)^q \tag{44}$$

The position of the maximum of the pinning force on the cordinate axis of reduced field b is defined by the ratio $p/(p+q)$. Kramer (49) investigated the experimental data of several groups of hard superconductors, eg, NbZr, NbTa, NbTi, NbHf, Nb_3Sn, and V_3Ga, and pointed out that equation 43 can indeed describe the pinning force with the power n varying between 2 and 3, and with the function $f(b)$ depending on the microstructure and metallurgical treatment (50).

This general formulation, equation 43, fails where there is a change in basic pinning mechanism due, eg, to matching effects, dimensional crossover, or the onset of thermally activated processes. In such cases, more appropriate descriptions of the pinning in the full-field range can be given by the assumption of two pinning mechanisms. Then equation 43 can be rewritten as

$$F_p = BJ_c = S'[\frac{B_{c2}(T)^{n'}}{k^{m'}}]\, f(b)' + S''[\frac{B_{c2}(T)^{n''}}{k^{m''}}]\, f(b)'' \tag{45}$$

Such an approach was adopted in describing flux pinning of $YBa_2Cu_4O_8$ single crystals (50) and can be used in intermetallic superconductors, eg, Nb_3(Al,Ge), where the peak of J_c versus B is observed at both lower and higher fields (51).

2. Low Temperature Superconductors (LTS)

2.1. Transition Metals for Devices

Niobium and tantalum themselves as pure metals are not very practical for applied conductor development, but they are probably the most important electrode material for tunnel junction fabrication used in superconducting devices, eg, SQUID, X-ray detectors, optical detectors, and mixers. There are many reasons why such electrode materials are used longer lifetime, mechanical strength, chemical stability, high critical temperature, good adhesion to the substrates, high stability of the oxide barrier together with no deformation of the electrodes even after many temperature cycles. Niobium electrodes and aluminium oxide as the barrier show a pronounced knee in the quasiparticle branch of the current–voltage characteristic curve. The thickness of the oxide barrier very accurately determines the resistance and the critical current density of the superconducting tunnel junction. Performance of Nb and Ta is satisfactory, but increasing resolution of the Mo and Hf materials can be considered in the future development of electrode technology (52).

2.1.1. Tantalum for Superconducting Tunnel Junction

Tantalum has a number of attractive characteristic for photon detection. The characteristic quasiparticle lifetime, t_o, is > 10 times greater than for Nb and its reasonably high transition temperature near 4.5 K. In this respect, the superconducting properties are more akin to those of Sn. Epitaxial Ta films are formed in a superconducting body centered cubic (bcc) phase with room temperature resistivity $\sim 13.5\ \mu\Omega$ cm. In general, thin polycrystalline films do not superconduct. Sputter Ta films deposited onto a room temperature substrate are formed in the β-phase. The β-phase is characterized by a high room temperature resistivity (150–200 $\mu\Omega$ cm) that has a transition temperature of 0.5 K. However, it it possible that a thin (< 20 nm) layer of polycrystalline Nb could be used as a seed layer to promote formation of Ta in the bcc phase for room temperature deposition (53).

2.2. Nb–Ti Conductors

The major use of niobium is in the steel industry in the production of ferroniobium (85%), followed by superalloys (12%), where only 3% is shared between aerospace industry, nuclear energy, lighting, and superconductivity. The well-established Nb-based low temperature superconductors, eg, NbTi and Nb_3Sn, represent 98% of the world production of superconducting materials. The remaining 2% is shared between Nb_3Al- and Bi-based high temperature superconductors (HTS). The Nb–Ti alloy was discovered soon after another superconducting alloy Nb–Zr, in 1960. Once it was established that Nb–Ti posses strong pinning at elevated magnetic fields ~ 5 T, the industrial process was adapted. This was originally developed by Teledyne Wah Chang to make filaments for light bulbs. Even though it was possible to use/adapt a well-established technology, the price of the first 61 filament wire was 400 £/kg during the first year of production and the performance was 70 A at 5 T for the 0.4-mm wire. After 1 year, the price dropped to 200 £/kg with minor improvements in current density. Interestingly enough, the price of 200 £/kg was stable for almost 20 years, because it was based on an already mature technology. Taking into account the rate of inflation to be $\sim 10\%$ an year, the absolute price went down systematically.

Today, the price of the simple Ni–Ti wire for magnetic resonance imaging (mri) applications is at the level of 1 \$/kAm where the price of the sophisticated ITER conductor is currently 2 \$/kAm. Further reduction of price can be realized by an increase of performance when artificial pinning centers are introduced. The optimization of the critical current density is part of the conductor fabrication process. The parameter J_c is determined by the microstructure and can therefore be manipulated largely during the wire fabrication process. Optimization of J_c is achieved by introducing finely dispersed microstructural features acting as pinning centers. In the case of Nb–Ti, the combination of the dislocation wells and normal conducting α-Ti precipitates in the superconducting β-phase, see the Nb–Ti phase diagram in Fig. 15, are known to be most effective pinning centers. An optimum size and distribution of the precipitates is achieved by applying intermediate heat treatments (at $\sim 400^\circ$C) during the wire fabrication process. The most intensive research and development was put into the process of producing a new class of Nb–Ti superconducting materials that is characterized by the highest J_e values when artificial pinning centers (APC) are introduced, was carried out by Haussner and co-workers (54). It was demonstrated that the processes and manufactured articles under development have the following advantages by comparison to the conventional ones: a possibility of making and adjusting the APC material structure to produce the strictly specified properties in superconductors; an economy-type achievement of the high level current-carrying capacity as compared to traditional materials; an opportunity for the essential increase (by a factor of 4–5) of the superconductors current-carrying capacity.

Even further reduction of the cost can be achieved by exploitation of new emerging technologies, eg, Direct Electroreduction of Oxides (DERO) developed at the University of Cambridge (55,56). The cost of Nb–Ti alloys, by the use of the DERO process, is expected to be only between four and seven times cheaper than using current technologies, because the Nb–Ti materials account for only 20–50% of the total cost of the final wire. The remaining cost covers all the other materials used in composite, deformation processes, electrical insulation, and personnel.

2.3. Intermetallic Superconductors with A15 Structure

Unlike NbTi, Nb_3Sn is a brittle intermetallic compound having a well-defined stoichiometry, which is obtained in the practical multifilamentary wire form by cold deformation processes followed by multistage reactive diffusion (57)–(60). The Nb_3Sn intermetallic has a lattice parameter $a = 0.518\,\mathrm{nm}$ and an A15-type structure, A_3B, which belongs to space group *Pm3n*. The first single crystals of Nb_3Sn have been grown by Hanak and co-workers (61). The synthesis of this compound by the gas-phase reaction appeared to be feasible because both Nb and Sn can be obtained by the hydrogen reduction of their gaseous chlorides at temperatures well below 1000°C. A simultaneous reduction of a mixture of these chlorides yields crystalline Nb_3Sn without the intermediate formation of the free metals or other Nb–Sn phases, eg, Nb_6Sn_5 and $NbSn_2$. The overall reaction for the production of Nb_3Sn deposits can be described as

$$3\,\mathrm{NbCl_4\,(g)} + \mathrm{SnCl_2\,(g)} + 7\,\mathrm{H_2\,(g)} \Rightarrow \mathrm{Nb_3Sn\,(s)} + 14\,\mathrm{HCl\,(g)} \tag{46}$$

Intermetallic compounds were widely explored as potential superconducting materials in the 1950s and 1960s. The best intermetallic superconductors, based on niobium-rich compounds with group IIIB and IVB elements (eg, Nb_3Ga, Nb_3Al, and Nb_3Sn), are still under continuous development and new discoveries of a cheaper and more reliable processes are described (51,60,62). These are isotropic materials in which the conduction electrons travel in an electronic band made from niobium *d* states. The nature of the relation between the unique properties of the A15 intermetallic compound and the crystallographic structure was first pointed out by Weger (63). The A15 structure is distinguished from other intermetallic phases in the Nb–Sn phase diagram by having three distinct families of Nb atoms arranged in chains parallel to the [100], [010], and [001] axes. The quasi-one-dimensional nature of the Nb lattice leads to unusual features in the electronic band structure, which are responsible for the unique properties. The atomic volume of the transition metal atoms, eg, Nb, are smaller than that of non-transition-metal atoms, eg, Sn, and thus have to be considered as the more decisive factor in determining the properties of these materials.

2.4. MgB_2

The discovery of superconductivity in the well-known MgB_2 material at the beginning of the twenty-first century (64), has made us aware of the possibility of the existence of new superconducting materials that may have critical parameters, which are in some cases even better than the existing superconductors. As was described in the *New Scientist*: "In just a few months, a new superconductor has upstaged its rivals" (65). This important discovery stimulated three types of research: (*1*) toward a combinatorial search for new superconducting materials; (*2*) on basic science of MgB_2 properties; and (*3*) of research focused on optimum thermomechanical procedures for the manufacture of the powder-in-tube and coated conductors using doped and substituted Mg–B compounds (66,67).

Of the 96 binary boride systems known, only 60 have compounds of boron with metals of the subgroups Ia–VIIIa crystallizing in > 30 structural types. The stability of borides formed by metals decreases with increasing atomic number. In extreme cases, borides of copper do not exist and Cu–B, Ag–B, and Au–B systems are simple eutectic alloys (68). An essential role in the boride structures, unlike the carbides of the same metals, is that of the electron interaction between the boron atoms. This interaction depends both on the electron state of the metal, M, and on the value of the atomic ratio of boron/metal. In particular, with an increase in this ratio the structure formation evolves from one of the isolated boron atoms to an unbroken 3D framework, and can be shown by the following series: M_4B, M_3B, M_2B, MB, M_3B_4, MB_6, MB_{66},…, MB_{100}. The electron interaction between the boron atoms accompanied by the formation of strong covalent bonds is one of the main reasons that the diborides crystallize in the structure-type MB_2. There are four phases in the binary-phase diagram

Mg–B: diboride, MgB_2; hexaboride, MgB_6; tetraboride, MgB_4; and dodecaboride, MgB_{12}. The influence of the magnetic states on the properties of borides decreases in the direction of the increasing number of B atoms.

This superconducting compound in the fully ordered form has twice the transition temperature of Nb_3Sn and four times that of the NbTi alloy. The vital prerequisite of strongly linked current flow has already been demonstrated (69). One possible drawback, however, is that the upper critical magnetic field at which superconductivity is destroyed is modest and the material is anisotropic. Also, the so-called irreversibility field H_{irr} is low. In bulk and thin-film MgB_2 samples, it has been found that the irreversibility field is rather low compared to the upper critical field in the low temperature region, showing the possible existence of a quantum vortex liquid due to strong quantum fluctuation (69,70).

The weak temperature dependence, but strong field dependence, of the relaxation rate may further suggest that the vortex melting at a finite temperature is also induced by the strong quantum fluctuation. The reason for such a strong quantum effect is still unknown, but it may be related to the superconducting mechanism of MgB_2 (71). On other hand, a strong intergranular current typical for the intermetallic compounds leads to the conclusion that MgB_2 is more akin to a low T_c metallic superconductor than to a high T_c copper oxide superconductor (69). Recent research results demonstrated that MgB_2 is a BCS, phonon-mediated superconductor with the two distinct superconducting energy gaps that can be observed in the clean limit (72). In the dirty limit, which is applicable for MgB_2 postanneled films, only one average energy gap can be measured.

Commercial exploitation of the recently discovered MgB_2 superconductors will be severely limited unless mechanically robust, high critical current density, composite conductors can be fabricated with uniform properties over long lengths. The experience with LTS, eg, A15 conductors Nb_3Sn, $Nb_3(Al,Ge)$ and also the whole range of HTS conductors, suggests that to be able to unfold the full superconducting potential of the metal-borides, one has to address fundamental questions concerning the practical capability of the newly discovered material to conduct intergranular supercurrents in high magnetic fields considering the short coherence length$\xi_0 = 5.2\,\mathrm{nm}$ (73), which it appears is anisotropic and may vary from 2 to 7 nm depending on the sample preparation. It looks promising that new reliable superconducting joints and superconducting switches will be developed not only based on the new MgB_2 conductors, but also between MgB_2 and low temperature superconducting conductors, eg, NbTi, Nb_3Sn, and Nb_3Al opening a new range for electromagnetic device applications.

2.4.1. Thermoelectric Stability

Because of the possible relatively large filament size in new MgB_2 conductors, there are two important aspect of quench protection and stability: magnetic and cryogenic. First, to avoid flux jumps in the large filament MgB_2, conductors use of a magnetic shielding material, eg, iron, is advantageous to reduce large magnetic flux gradient in the superconducting filaments. Second, to provide adequate cryogenic stabilization, an external highly conductive (thermally and electrically) metal is essential. The role of copper as a stabilizing layer is very important for the stability of the conductor. As it emerges in a simplistic design where only the Fe matrix is used, the instability of the current appears to be a very important issue (74). Single-core Fe/MgB_2 PIT wires are very unstable. At the range of $E = 10\ \mu\mathrm{V/cm}$, such wire, without the Cu stabilizing layer, achieves the limit of liquid helium film boiling (T-$T_0 \sim 0.15\,\mathrm{K}$) and a further increase of the electric field may cause an unstable behavior (67).

Therefore usage of Cu as a stabilizing layer is an important approach to protect wires from damage in real power applications. Application of Cu as the only metallic matrix in the manufacture of the *in situ* MgB_2 wires during high temperature reaction between Mg and B (66,67) has some advantages over the other matrix materials. Such conductors are very stable due to a unique percolative stabilizing network formed between Mg and Cu in the body of the superconducting core. This provides an excellent thermodynamic stability to such conductors. It was proved experimentally that Cu stabilized *in situ* MgB_2 conductors are much more stable. However the presence of the $MgCu_2$ phase in between Cu and MgB_2 [which may contribute to 50 K T_c

anomaly (75)] forms a higher resistivity shell around the MgB_2 and may effect perfect heat transfer between superconductor and cryogenic liquid.

2.4.2. Critical Current Density in PIT Conductors

The exemplary data for the PIT conductors by an *ex situ* and *in situ* technique in comparison with LTS are presented in Fig. 16. Also a high transport critical current of solenoidal MgB_2/Cu coils fabricated using a wind-reaction *in situ* technique was recently reported (77). For MgB_2 coated conductor the maximum of the pinning force, which occurs at $b_{\max} = (n/n + m)$, see equation 42, shifts in the position toward the higher magnetic field and the actual value of the pinning force. The value is five times higher for MgB_2 coated conductor in comparison to PIT conductors (67). This reflects different types of flux pinning mechanisms induced by the fine nanoscale defects and inclusions in coated conductors (78).

High J_c values have been reported in thin films where many results exceed 10^6–10^7 A/cm^2 in a low field at 4.2 K (Fig. 16). Electron microscopy (70,78,79) shows that very small grains, as small as 10 nm in size, are produced in films made by pulsed-laser deposition. The high number density of grain boundaries is consistent with such high J_c values (69). In addition, transmission electron microscopy shows a substantial fraction of insulating MgO particles $\sim$10 nm in size. These are likely additional flux-pinning centers, since the diameter of magnetic flux lines is about this size.

2.4.3. Conductors for ac Applications with Improved Critical Current

2.4.3.1. Self-Field. Since iron appears to be one of the favorite materials used as an inert matrix especially for the Powder-in-Tube conductors, one can explore the possibilities of superconducting-magnetic heterostructures (80,81) with the aim of minimizing ac losses for novel electrotechnological devices. Generally, the ac losses in multifilamentary wires can be reduced by twisting filaments. The shorter the twist pitch length, the larger the ac loss reduction. The minimum practical twist pitch is approximately five times the diameter of the composite. While these twist pitches are fully effective in uniform external magnetic fields, they are only partially effective in nonuniform fields and less effective with respect to the self-field of the composite. In self-field conditions, the twist does not change the self-field flux linked between the inner and outer filaments substantially and the current first fills the outer layers of the superconducting composite, similar to a solid superconductor. To decouple the filaments in self-field conditions, a magnetic screening method was proposed (80,81). This method is extremely important for the coated conductor configuration, but is also very important for the multifilamentary wires and consists of surrounding each superconducting filament by a thin ferromagnetic layer.

In conclusions, magnetic shielding of the filaments reduces ac losses in self-field conditions because of decoupling of the filaments and at the same time it increases the critical current of the composite.

2.4.3.2. External Magnetic Field. Compared with other superconductors, MgB_2 has the advantage that it does not react with iron. Moreover, iron is the unique metal that can be used as a protective layer between MgB_2 and a stabilizing outer copper layer. Therefore, it automatically provides the magnetic shield of the filaments as well. It has been found that a multiple layer shield is more effective than a thicker single layer. From the numerical calculations of the hysteresis loss conducted for the magnetically clad monocore MgB_2 wire, it was concluded that ac loss in iron shields is negligibly small in comparison with the loss in the MgB_2 wire. Therefore losses in the shielded MgB_2 wire are negligibly small as compared with an unshielded one, up to a applied magnetic field of 0.3 T. Magnetic fields of this magnitude appear in some applications as, eg, superconducting transformers. The ac losses in the coated conductors are very sensitive to magnetic field orientation with respect to the conductor surface. Even for the untextured MgB_2 coatings, the only way to reduce losses effectively is to align the filamentary conductors parallel to the external magnetic field. Increasing the number of the filaments is very helpful in this case, but if the magnetic field can be correctly aligned along the conductor surface, the losses will be minimal.

2.5. Chevrel Phase (Pb,Sn)Mo_6S_8

The ternary compound $PbMo_6S_8$ was synthesized in 1971 by Chevrel (82) and superconductivity was discovered by Matthias and Marezio (83) with $T_c = 13.2\,K$. The Pb atoms are situated between the Mo_6S_8 units and have an unusual atomic environment. The Mo_6 clusters in the metallic chalcogenides do interact with each other because they are only 0.31–0.32-nm apart. These interactions are relatively weak, ie, they do not contribute much to the cohesion of the structure. They do, however, contribute to the stability and the size of the Mo_6 atom clusters. They are also very important for the electronic properties because they provide a 3D network of possible electronic conduction paths in the crystals. Considering the complexity of the crystallographic structure of the Chevrel phase, the crystal chemical formula of $PbMo_6S_8$ can be presented as $Pb^{[2S]}Mo_6{}^{[4Mo+5S]}S_6{}^{[4Mo]}S_2{}^{[3Mo+1Pb]}$ (84). A very comprehensive source of data describing structural, electronic, and lattice properties of the molybdenum-based ternary superconducting materials has been edited by Fisher and Maple (85). Since discovery of the superconductivity in this compound and the definition of very high upper critical fields of $PbMo_6S_8$ by Fisher $H_{c2} \sim 50\,T$ (86), much work was conducted on the development of practical conductors (87). Despite the initial impetus, when such promising material characterized by high H_{c2} was obtained, even today after 30 years of research, enough high J_c has not been obtained for this type of conductor. The main reason is the polycrystallinity of the superconducting core and low intergranular current, which make this material comparable to $YBa_2Cu_3O_7$ PIT conductors. The reduced pinning force versus reduced magnetic field $b = B/B_{c2}$ of a $PbMo_6S_8$ bulk sample at different temperatures can be fitted by one universal curve described by the parameters $p = 0.5$ and $q = 2$ and $n = 2.4$ in equations 42 and 43. In comparison with the technical superconductor Nb_3Sn, this is a signature that the J_c of magnetic fields lower than 10 T is dominated by grain boundaries. It was shown that the efficiency of grain boundaries as the pinning centers in $PbMo_6S_8$ is quite modest. Even when considering the coherence length $\xi_o = 4.8\,nm$, the macroscopic critical current is 20 and 10 times smaller in bulk and wire samples, respectively, in comparison with intergranular critical current. Unfortunately, currently even these values cannot be maintained over the whole length of the wire (88). The main reasons for this are microcracks and chemical ingomogeneities.

Also considering that such wires are manufactured as single-core conductors not as multifilamentary wires, currently make the applicability of Chevrel-phase conductors very limited. This material may not have much of a chance to compete with granular HTS polycrystalline wires and advanced Nb-based intermetallic superconductors. As with other superconducting materials, in spite of the high values of B_{c2}, the irreversibility line, B_{irr}(T), of the wires lies far below the B_{c2} (T) curve (89,90). Nevertheless, magnetic measurements on bulk samples have shown that Chevrel-phase materials may not be intrinsically granular despite their short coherence length (91,92).

3. High Temperature Superconducting Ceramic

The discovery of high T_c superconductivity in 1986 in structurally layered copper oxides astonished the materials science and condensed matter physics communities. The highly anisotropic crystal structures, the evolution of superconductivity from magnetism by chemical doping of the $3d^9$ Cu^{2+}-based host compounds, and the special aspects of copper–oxygen bonding make these materials of continuing interest. High T_c superconductivity has been a windfall for solid-state chemists, with ~100 new superconducting copper oxide based compounds discovered, and hundreds of new materials found and characterized.

According to the BCS theory, a high density of electronic states is preferred for high T_c. The charge carriers in all discussed HTS materials are thought to be essentially provided by deviating the nominal valence of copper from 2^+ to $(2+d)^+$. The compounds that contain divalent copper ions are insulators despite the odd number of valence electrons expected per unit cell. The origin of the gap formation in the conduction band has been attributed to the strong electron correlation relative to the energy corresponding to the band width (93). In the superconducting compositional region, it has been known that the energy gap structure described above is essentially retained on doping of the carriers to a substantially high level. Although the carrier density can be increased even higher by increasing the doping level, the gap structure then seems to be destroyed, and T_c quickly decreases (94). Therefore, the maximum carrier density remains in the range 2×10^{21}–5×10^{21} cm^{-3}, which is significantly lower than that of the typical metallic superconductors (10^{23}). Consequently, it seems likely that the low value of the carrier density is inherent in the extraordinarily high T_c of the oxide superconductors. This fact must be considered to tailor-make the oxide superconducting materials for practical applications. A low carrier density significantly affects several important superconductor properties including chemical stability (95). To increase the carrier density to the optimum level, one must make the valence of copper deviate significantly from 2^+. Therefore, resulting compounds do not have a rigid stoichiometric composition, and their crystal structures are rather loose. The composition tends to change depending on the processing conditions as well as the starting compositions. The fabrication method of oxide superconductors may thus have to be much more complex than the usual ceramic processing methods. In this content, such processing methods directed toward high purity as ultrahigh vacuum, controlled oxygen partial pressure, low temperature, rapid cooling, nonequilibrium, and/or atomic layer-by-layer processing may have to be considered (95).

Since the cuprate superconductors are the compounds of strongly alkaline and weakly acidic oxides, chemical stability is another problem. For example, the reaction between oxide superconductors and common oxide substrates, eg, Al_2O_3, YSZ, SiO_2, results in an undesirable interface region for thin-films processes. Water and carbon dioxide are known to deteriorate the superconducting properties by penetrating the grain boundaries of the sintered bodies. The low carrier density also leads directly to a decreased capacity to electrically screen the net charge in the material. Accumulation of net charge tends to occur in the ionic compounds at imperfections, typically at grain boundaries resulting from the deviation from the bulk composition or the segregation of impurity ions in the vicinity of the interface. The effective thickness of the potential barrier resulting from the interface charge Q per unit area can be approximated as dQ/n_c, where n_c is the carrier density. Therefore the potential barrier at the boundary could prevent the free transmission of current, especially in low carrier density materials. In oxide superconductors, the significance of the boundary potential barrier was first pointed out by Koch and co-workers (96) in YBCO, based on the observation of the Josephson junction V-I characteristics across grain boundaries. The transport critical current has been reported to be reduced across a single grain boundary to a varying extent, depending on the relative tilt angle based on the measurements of many bicrystal thin-film specimens of $YBa_2Cu_3O_7$ (97). Since the carrier density may not be increased significantly, more studies directed toward reducing the net charge at the boundary are needed. Currently, some information regarding the possible origin of the net charge has been reported using Ca doping of the high angle grain boundaries. In principle, it should be possible to neutralize the boundary net charge by adjusting the additive ions. However, associated noticeable reduction of T_c may be inevitable.

Despite tremendous research activities, the needed and promised HTS applied conductors, eg, $YBa_2Cu_3O_{7-\delta}$ wires and coated conductors, are still in a very infant stage of scaling up. They suffer from low engineering critical current density, J_e, and also have unacceptably high ac losses. The issue concerning the ac applicability of such HTS coated conductors was partially solved by use of laser filament patterning or by use of an additional magnetic material to modify the electromagnetic field distribution (81,98). However, sustained well-supported development is required to optimize such conductors.

3.1. The p- and n-Type HTS Superconductors

It was thought at the time when metallic superconductors were discovered that BCS-like superconductivity above $\sim$ 30–40 K would be very unlikely. Bednorz and Müller (99) made a long awaited important breakthrough in 1986 when they discovered superconductivity at 36 K in the La–Sr–Cu–O system, which won them the Nobel Prize in 1987. Materials with yet higher transition temperatures were developed over the next few years, notably with the discovery of $YBa_2Cu_3O_{7-\delta}$ by Wu and co-workers (100) with a maximum transition temperature of 93 K. The presence of superconductivity in this group of materials above the boiling point of liquid nitrogen makes them potentially one of the most important technological breakthroughs of the previous century. Currently, the highest known transition temperature is 135 K in $HgBa_2Ca_2Cu_3O_{8+\delta}$ (101,102), which can be increased to just > 160 K with the application of 30-GPa pressure. All the above applicable superconductors are p-Type (hole charge carriers), but there are also n-Type superconducting oxides, eg, $Sr_{2-x}Nd_xCuO_2$ ($T_c = 40K$) (103) and $Nd_{2-x}Ce_xCuO_2$ ($T_c = 22K$) with dominating electron charge carriers. The Hall constant, R_H, is negative in electronic superconductors (104) while for p-type superconductors R_H is positive (105,106).

There is experimental evidence that low dimensional structures (so-called heteronano interface, HNI, formed at the atomic level at the superconductor/normal metal or alloy interface), which involve processes, eg, Andreev reflection (29) and proximity effect (30), may be a pathway to even higher T_c superconductivity (67,107). However, it is not yet understood why such superconducting anomalies are observed only for specific type of superconductor–metal interfaces.

3.2. Magnetic Phase Diagram of High Temperature Superconductors

The breakthrough made by Bednorz and Müller in 1986 was clearly linked to the replacement of lanthanum by strontium in a La_2CuO_4 insulator. When some of the lanthanum atoms were replaced by strontium, $La_{1.85}Sr_{0.15}CuO_4$ looses all resistance to electric current and becomes a superconductor. The temperature below which this "doped" cuprate becomes superconducting varies with the concentration of strontium, and reaches a maximum of 38 K. This process is called doping and involves replacing an atom with three available electrons by an atom with only two available electrons. This introduces "holes" into the copper oxide layers: These are the charge carriers that make the material conducting, and under the right conditions, superconducting. The actual magnetic properties of the copper oxide ceramic can be expressed in terms of carrier doping as presented in Fig. 17. The antiferromagnetic region in Fig. 17 is the best understood region in the phase diagram. At zero doping the cuprates are all insulators, and below a few hundred degrees kelvin, they are also antiferromagnets (ie, the electron spins on neighboring copper ions point in opposite directions). However, when the doping is increased above a critical value (∼5%, although this varies from compound to compound), the antiferromagnetic state disappears and the so-called pseudogap or underdoped region is entered. It is called underdoped because the level of doping is less than the level that maximizes the superconducting transition temperature. Some of the most interesting behavior observed in the cuprates is detected in this region. High temperature superconductivity was discovered in materials with low carrier concentration, indicating that for superconductivity, charge fluctuations on the nanoscopic scale are essential. In HTS materials, an energy gap appears to open up in the electronic state at a temperature that is much higher than the superconducting transition temperature. In contrast, in metallic superconductors the BCS-type superconducting energy gap opens abruptly only when the temperature falls below the critical temperature. The presence of this energy gap in the nonsuperconducting state of HTS, known as the pseudogap, is a vitally important issue in the arguments on the HTS mechanism. A variety of explanations have been proposed for the pseudogap. Furthermore, the presence of a pseudogap has a considerable influence on the consideration of J_c. The J_c is determined by the pinning effect, and the trapping energy of a Fluxon on a pinning center determines the pinning force.

The formation of the pseudogap reduces the pin potential and is probably undesirable in terms of efforts to improve the J_c. If the above arguments were correct, a smaller pseudogap would be preferable for improving the J_c. A superconductor composition with a slightly higher hole concentration is preferable for attaining high J_c values, even if the T_c value must be sacrificed somewhat. The finding of an impurity that restrains the formation of the pseudogap, but has little effect on the T_c, would be a valuable contribution to increasing the J_c. The best known characteristic of the superconducting region is the fact that the resistivity is zero. However, condensed-matter physicists measure many other properties to define superconductivity, eg, the energy needed to split the Cooper pairs. This is the superconducting energy gap, 2Δ. The pairing process

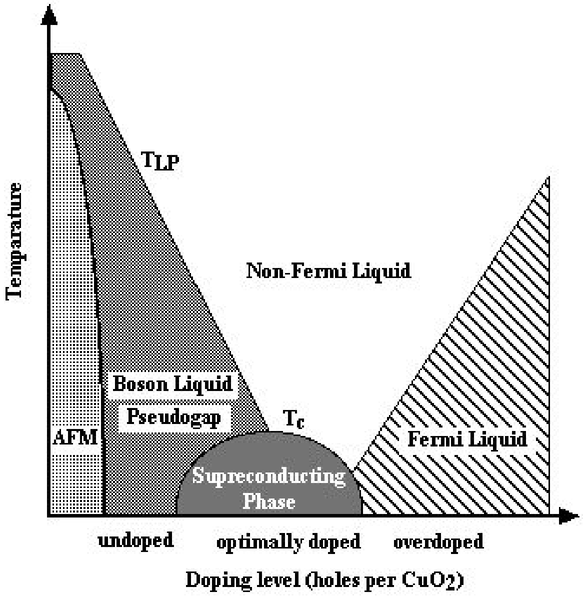

Fig. 17. The properties of the cuprate oxides vary with temperature and the doping per unit cell of CuO_2, (After Ref. 108.)

means that there are no single-particle excitations with energies of $< \Delta$ in the superconducting state, hence the name gap. Normal metals and Fermi liquids do not exhibit such gaps. Energy gaps show up clearly when the single-particle density of states is plotted, ie, when the number of electronic states with a given energy is plotted as a function of energy. The Fermi-liquid region of the phase diagram is also well understood. One of the central concepts in condensed-matter physics, introduced by Landau, is the “quasiparticle”. In a so-called Landau-Fermi liquid, the properties of single electrons are changed or “renormalized” by interactions with other electrons to form quasiparticles. The properties of the material can then be understood in terms of the weak residual interactions between the quasiparticles and their excitations. A key feature of the quasiparticle concept is that low energy single-particle excitations have very narrow linewidths: $\Delta\omega \sim \omega^2$, where ω is the energy of the excitation. When the quasiparticle approach is valid, there is a well-defined boundary between particles and holes in both energy and momentum space at zero temperature. This boundary occurs at the Fermi energy and defines the Fermi surface in momentum space. However, the Landau quasiparticle model can only explain part of the phase diagram of the cuprates. The part of the phase diagram between the underdoped and the Fermi-liquid regions, and above the area with the highest superconducting transition temperatures, is called the non-Fermi-liquid region. The thermodynamic properties in this region are unexceptional and, within experimental uncertainties, are in fact similar to the behavior of a Fermi liquid. However, this region is characterized by exceptionally simple, but unusual, power laws in all of its transport properties as a function of temperature. These transport properties include the resistivity, the optical conductivity, the electronic Raman-scattering intensity, the thermal conductivity, various nuclear relaxation rates, the Hall conductivity and the magnetoresistance. These unusual transport properties are why this part of the phase diagram is called the non-Fermi-liquid region (108).

3.2.1. Layered Structure

In addition to their high T_c values, the large spatial anisotropy of high T_c superconductors is striking (see section (3.2)). The anisotropy is due to the layered crystal structure, which is currently believed to be essential

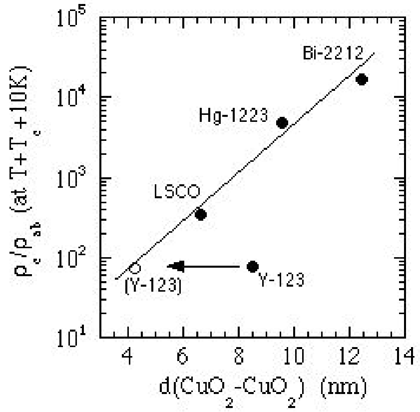

Fig. 18. Correlation between the electric anisotropy factor and the distance d between CuO_2 layers in typical perovskite superconductors. The CuO chain bonding layer is regarded as equivalent to that of the CuO_2 layer in $YBa_2Cu_3O_7$ (Y-123), Hg1223, Bi2212, and Y-123 are abbreviations for $HgBa_2Ca_2Cu_3O_{8+d}$, $Bi_2Sr_2CaCu_2O_8$, and $YBa_2Cu_3O_7$, respectively.

for the existence of high T_c superconductivity. The layers are composed of CuO_2 planes, separated from each other by planes of various other oxides. It is believed, on both experimental and theoretical grounds, that superconductivity and charge transport are mostly confined to the CuO_2 planes. There is a clear linear dependence for the critical temperature to be higher at lower characteristic distances in the perovskite structure (109).

Microstructural anisotropic properties of the HTS n- and p-Type superconductors are manifested in a dramatic anisotropy of the upper critical field $\mu_o H_{c2}$ for the field parallel or perpendicular to the ab planes.

3.2.2. Structural Anisotropy and Fluxon Line Fragmentation

An extremely short ξ_c in the c-axis direction (perpendicular to the layer structure) results from the poor electronic transfer between CuO_2 layers. Superconductivity can easily be destroyed in the interlayer regions, and the CuO_2 layers can almost be regarded as coupled by a Josephson interaction. This phenomenon results in a large anisotropy. Anisotropy is mainly determined by the crystal structure of the superconductor. Figure 18 shows the relationship between the resistivity anisotropy factor and the crystal structure of typical superconductors with the composition of the highest T_c. Essentially, the anisotropy is smaller in substances with a short interlayer distance d between CuO_2 layers (76). Two methods have been proven effective for reducing the anisotropy factor in a particular substance: (*1*) increase the carrier concentration, and (*2*) replace the ions in the partially insulating layer between CuO_2 layers. The anisotropy of a material can be improved by about one order using either of the two methods. An increase in the distance of insulating layers in the cuprate materials weakens the coupling between superconducting CuO_2 planes along the c axis. This decoupling between planes causes the vortex lattice to break into pancakes and strings.

3.2.3. Irreversibility Line

An increase in the number (and distance) of insulating layers in the cuprate materials weakens the coupling between superconducting CuO_2 planes along the c axis and also results in a decrease in the irreversibility line. A progressive decrease of the irreversibility line is linked with increasing lattice anisotropy. The Josephson coupling energy between CuO_2 layers across the block layer varies inversely as the c-axis resistivity, which, within a tunneling model, may be expected to vary exponentially with the d_b spacing. Thus, if the irreversibility field is determined by the Josephson conducting across the block layer, then it can be expressed by equation

47.

$$H_{\mathrm{irr}} \propto \exp\left(\frac{-d_b}{\xi_{co}}\right) \tag{47}$$

where ξ_{co} is a c-axis correlation length. The proportionality will contain a universal function of T/T_c as well as a power law dependence on the superfluid density. Equation 46 indicates for the crystalline samples that H_{irr} is determined by anisotropy, not by pinning (110). In terms of the absolute value of the H_{irr}, the best superconducting material for application at liquid nitrogen temperatures is Tl-1223 and Hg-1223 (liquid nitrogen exists at temperature range from 65–124 K, depending on pressure). The direct J_{c} measurements of the $(Tl,Pb)Sr_2Ca_2Cu_3O_9$ and $(Hg,Pb)Sr_2Ca_2Cu_3O_9$ coatings have shown that at 91 K, at which $YBa_2Cu_3O_7$ is in the normal state, Tl- or Hg-based superconductors can conduct 1 MA/cm^2. Unfortunately, due to the toxicity of these compounds there is little interest from industry and from applied research organizations for the development of Tl, Hg practical long length conductors. Even at universities, research on these compounds is very restricted due to current strict safety regulations. Therefore, research is aimed toward thin and thick films and devices for microwave applications. There is hope for use of the novel multistage electrochemical deposition technique of Tl- and Hg-based coatings at room temperature (107), but further development and optimization is needed. As a result of such restrictions and limitations, research on $YBa_2Cu_3O_7$ large area coatings will inevitably intensify as the only currently acceptable HTS superconductor for applications in liquid nitrogen temperatures at fields up to few tesla because of its strong irreversibility line.

3.3. Applied Superconducting Conductor Processing Technologies

Earlier research and development of the powder-in-tube $YBa_2Cu_3O_{7-\mathrm{d}}$ conductors has shown that although this is the most favorable process for the conductor manufacture industry, the granularity and high angle grain boundaries retards the applicability of such conductors (111). Therefore, it is a technical challenge in which the major target is to pursue high speed and large-scale manufacturing processes of film deposition on long metallic alloy tapes. Based on technology developed for semiconductors, it is a challenge from miniaturization to large size fabrication. Several different types of deposition techniques, eg, pulse laser deposition, sputtering, chemical vapor deposition, metaloorganic chemical vapor deposition, thermal evaporation, sol–gel, and liquid-phase epitaxy, have been used to manufacture pieces of the high temperature superconducting tapes on a laboratory scale (112,113).

There are three major techniques used to manufacture so-called coated conductors: (*1*) RABiTS (Rolling-assisted, biaxially textured substrate) (114); (*2*) ion beam assisted deposition (IBAD) or the inclined substrate deposition processes (IDP); and (*3*) liquid-phase epitaxy (LPE) and thermomagnetic processing. The architecture of such conductors is presented in Fig. 19 (115).

3.4. Current Percolation Through the Grain Boundaries

3.4.1. Calcium Doping

For practical applications, the critical current density of the superconductor J_{c} is one of the most important physical parameters. In order to further improve practical conductors, the properties of the grain boundaries that limit the current must be fully understood. There is strong interest in chemical and structural modifications of the grain boundaries to improve the electrical properties of higher angle grain boundaries. There are pronounced changes in the microstructure and improvement of the electrical properties of the small-angle GB and also high angle GB that are induced by doping the boundaries with Ca. Calcium doping provides a viable means of engineering the electrical structure of the grain boundaries themselves, which are polycrystalline $Y_{0.8}Ca_{0.2}Ba_2Cu_3O_7$. Also, one may accept that J_{c} improvement of Ca-doped $YBa_2Cu_3O_7$ coatings could change

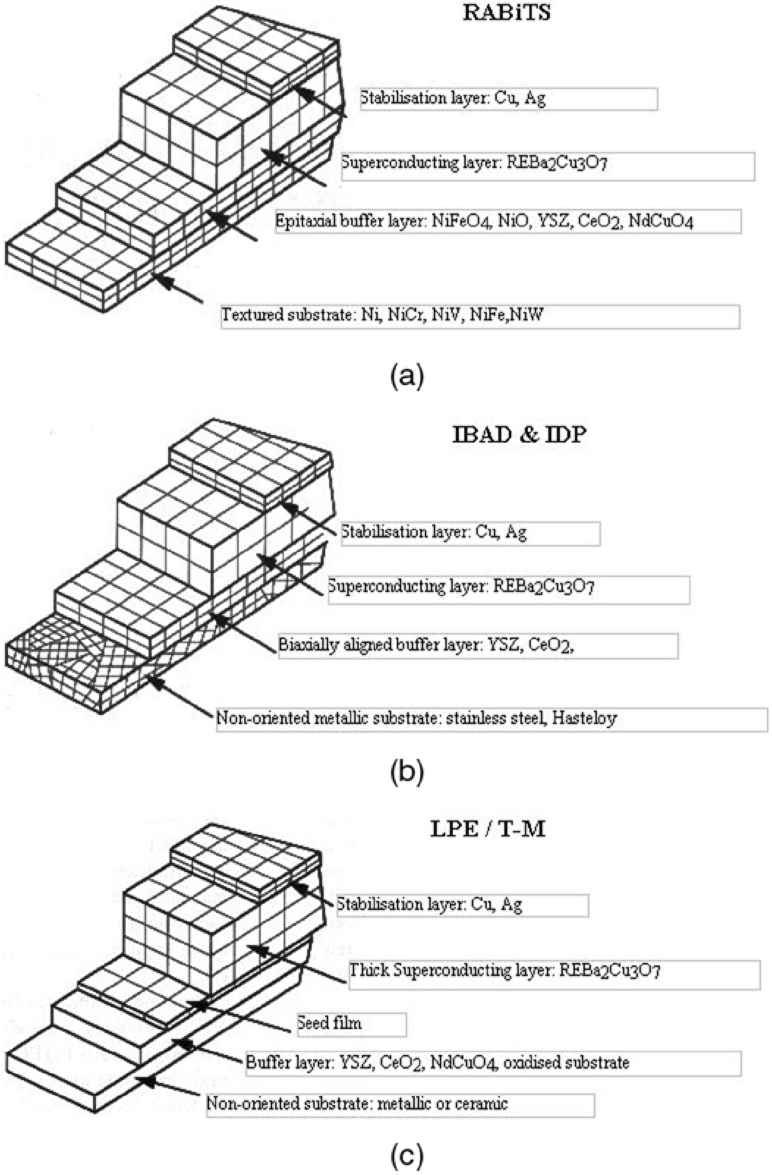

Fig. 19. Schematic representation of different architectures of the coated conductors: (**a**) RABiTS; (**b**) IBAD or IDP; (**c**) LPE or thermo magnetic process. (Courtesy of Y. Nakamura and Y. Shiohara, SRL.)

the level and shape of the J_c/J_{co}(length, width) dependence shifting J_c/J_{co} to higher values (116). The downside of Ca doping is the reduction of T_c and the necessity of avoiding oxygen overdoping. It is also possible to engineer the grain boundaries of the $REBa_2Cu_3O_7$ coatings with better connectivity by manipulating the composition of GB using a mixture of the rear-earth elements with different ion radiuses.

3.4.2. Conductors for ac Applications

The critical current decreases rapidly as the conductor length increases and the effect of the superconductor width is very significant (117). In the case of conductors for ac applications, where division of the superconducting coatings to the form of the filamentary structure and also magnetic decoupling of the filaments is essential (80), the percolative character of the current transfer in superconducting coatings may strongly reduce current capabilities of the conductor for particular applications. In an extreme case, if the size of the superconducting path becomes comparable to the grain size of the actual coating, the transport current will be reduced to zero. This problem of the coated conductor has to be addressed for each ac application to minimize the current percolation and simultaneously to minimize ac losses through the optimized filamentary structure and grain morphology. For example, this negative effect of current reduction due to the grains size comparable to the filament width can be minimized by using the IBAD process rather the RABiTS process, since grains of the IBAD coated conductors are one order of magnitude smaller.

3.4.3. Bulk Superconducting Joints

In bulk materials, the possibility of joining large single grains of (RE)123 materials considerably enhances the applicability of bulk materials with respect to large-scale applications. The ability of bulk superconductors to trap magnetic flux is determined by the product of its critical current density and the macroscopic dimensions of the specimen. Therefore, maximum trapped flux density in bulk materials, is obtained by maximizing the product of critical current density times the sample size of the given superconductor. On this basis large, high J_c bulk superconductors are required for high permanent field magnet applications. High quality superconducting joints produced via an infiltration method (118) have been successfully fabricated. An important point is that the irreversibility curves for both the intragrain and low angle GB intergrain area obey the same scaling $H_{\mathrm{m}} = H_o(1 - T/T_c)_n$. This is strong evidence that the boundary material may possess characteristics, identical to those within the grain. However, the production of bulk superconductors on a large scale presents several difficulties and superconducting joining technology is not a matured technique, yet there are attempts to grow the large surfaces by closely distributed seeding (119). In such a case, single-domain bulk superconductors can be achieved at the early stage of crystal growth, so that the liquid layer could not be inserted in the case of seed arrangement without spacing.

3.4.4. Pinning Centers

Pinning centers that define J_c versus B performance of the applied oxide superconductors can be classified, in order of effectiveness, as follows: (*1*) finely arranged, planelike defects that are oriented along the *c* axis. (However, usual grain boundaries become the sites of weak links due to the excessive thickness in which superconductivity is destroyed. Hence, a boundary of less disorder in the atomic arrangement is more desirable, such as a twin boundary, twin boundary pinning centers because of the phase transitions that are generated during the cooling process); (*2*) fine linear defects extending along the *c* axis; the size of these defects should be as close to the coherence length as possible (ie, ~ 2–3 nm), eg, columnar defects extending in the *c*-axis direction can be formed using heavy ion particle irradiation to form a superconductor that is capable of trapping Fluxons even in excess of 10 T at 77 K, simultaneously raising the irreversibility line; (*3*) finely dispersed pointlike defects whose diameters are as close to the coherence length as possible, eg, oxygen defects (clusters of oxygen vacancies) are naturally present in HTS materials, and submicron fine dispersion of the green insulation phase Y_2BaCuO_5 (120); (*4*) the interface of two phases that are both superconducting, but differ by pseudogaps, and hence have different energies for Fluxoids to be located in the two phases may act as the pinning center.

3.5. $Bi_2Sr_2Ca_{n-1}Cu_nO_{4+2n}$ Superconductors

Bibased family of superconductors also have perovskite-type structures with copper oxide planes and chains and orthogonal unit cells, Table 3.

Table 3. Superconducting Parameters and Structure of $Bi_2Sr_2Ca_{n-1}Cu_nO_{4+2n}$ Superconductors

Compound[a]	n, nm	c-axis/a-axis, T_cK	$\lambda_{ab}(0)$, $\lambda_c(0)$, nm	$H_{c2,ab}$,	$H_{c2,c}$, T	ξ_{ab}, nm	ξ_c
$Bi_2Sr_2CuO_6$	1	12/22					
$Bi_2Sr_2CaCu_2O_8$	2	3.090/0.54	85–90	300(ab),	500 (c)	280, 32	3, 0.4
$Bi_2Sr_2Ca_2Cu_3O_{10}$[b]	3	3.707/0.54	105–120	200(ab),	1000 (c)	250, 30	1.3, 0.2

[a] All Bi compounds are orthorhombic and the b axis is equal 0.541 nm.

[b] This compound is usually substituted by lead $(Bi, Pb)_2Sr_2Ca_2Cu_3O_{10}$ to stabilize the structure.

3.6. $(Bi, Pb)_2Sr_2Ca_2Cu_3O_{10}$ Conductors

Today, the PIT technique is used by several companies to make $(Bi,Pb)_2Sr_2Ca_2Cu_3O_{10}$ tape. There are of course variations in manufacturing processes from company to company, but the overall concept is the same.

3.6.1. Conductors for ac Applications: ac Losses

Electromagnetic losses occur in superconductors when they are exposed to time-varying fields or currents The pure hysteretic losses of the superconductor can be defined from the surface encircled by hysteresis loop M–H. The total losses of the superconductor are the sum of the hysteresis component, dissipated in the superconductor by the transport ac current or external ac magnetic field, and the coupling currents are induced in the resistive matrix. The transport losses, Q_t, are well described by the London-Norris equations for elliptical and rectangular cross-sections of a conductor (121,122). Loss in an elliptical superconducting wire does not depend on the eccentricity of the ellipse, and is given by (erg/length/cycle):

$$Q_t = \mu_o I_c^2/p[(1-i)\ln(1-i)+(2-i)i/2] \tag{48}$$

for the strip-type superconductor the loss is

$$Q_t = \mu_o I_c^2/p[(1-i)\ln(1-i)+(1+i)\ln(1+i)-i^2] \tag{49}$$

where $i = I/I_c$. The difference between these two equations reflects the different topologies of the field penetration in the two cases, rather than the actual geometry of the cross-section of the superconductor. Because losses are scaling with I^2, an equation can be rewritten to the reduced form:

$$Q^* = Q_t/I_c^2(B,\phi,T) \tag{50}$$

where ϕ is the angle of the magnetic field with respect to the ab planes of the superconductor (the smaller the angle ϕ, the higher the current) and T is temperature. Magnetic losses, Q_m, usually exhibit behavior according to the Bean critical-state model predictions.

To measure Q_t and Q_m ac losses, the electrical ac loss measurements techniques, transport current, and inductive are used. Hysteretic losses are difficult to calculate if the application requires simultaneous application of the ac transport field and an ac external field. In such a case, the best technique to measure the losses is a calorimetric method (123). To minimize the effect of ac losses in an external magnetic field, it is important to increase the resistivity of the highly conductive matrix, around the filaments, to alloy the matrix, or to introduce an insulating barrier.

Alternatively, to reduce ac losses even more effectively a magnetic material can be used instead of an insulating material around individual filaments, resulting in improvement of the superconducting filament stability and critical current improvement. It was proved that losses can be reduced substantially, more than an order of magnitude by coating individual filaments with magnetic material (79). Based on published results, one can conclude that magnetic screening–decoupling can be an effective method for decreasing transport ac losses in multifilamentary superconductors as long as percolative limitations in the individual filaments are taken into account. In comparison with losses in a standard (st), multifilamentary superconductor, Q_{st}, to losses in a multifilamentary superconductor with magnetic covers (cov), around individual filaments Q_{cov}, at the same reduced current i one can obtain magnetic decoupling loss reduction coefficient, K_{md}, (eq. 51); where $I = I/I_{\mathrm{c}}$, $I_{\mathrm{c1}} = I_{\mathrm{c}}/N$, N number of filaments.

$$K_{md} = \frac{Q_{st}}{Q_{\mathrm{cov}}} = \frac{\alpha I_c^2 F(i)}{Nk(i)a\alpha^2 I_{c1}^2 F(i)} = \frac{N^2 I_{c1}^2}{Nk(i)\alpha^2 I_{c1}^2} = \frac{N}{k(i)\alpha^2} \tag{51}$$

The parameters $k(i)$ and α are to be determined from the experiment and represent an individual filament. Here $k(i) = Q_{1\,\mathrm{cov}}/Q_1$ represents the ratio of the losses between the filament with the magnetic covering to the filament without cover, $\alpha = I_{c1\,\mathrm{cov}}/I_{c1}$ represents the ratio of the critical current between the filament with a cover to a filament without a cover. The larger the number of the filament, the higher reduction of losses in the conductor.

3.6.2. Conductor Joints

There are generally two types of joints used in electrotechnical applications of the superconducting devices and conductors: superconducting (superconductor–superconductor) and low resistivity (normal–superconductor, superconductor–normal superconductor). The superconducting joint (S-S) of two HTS wires has been studied by many researchers. For single core-to-single core joining, 80% J_c of the original value of the tape can be retained, where two tapes after uncover of the superconducting cores were pressed together. The sintering was conducted after a joint was made (124). Joining lengths of the conductor after final conductor manufacture is possible, but requires controllable atmosphere and well-controlled temperature distribution. Such a procedure is more complicated in the case of high current multifilamentary wires, where additional $(\mathrm{Bi,Pb})_2\mathrm{Sr}_2\mathrm{Ca}_2\mathrm{Cu}_3\mathrm{O}_{10}$ material has to be added and the continuity of almost perfect alignment of superconducting filaments may not be achieved. In such circumstances, it is better to join the ends of the superconducting wires before final annealing in a controllable atmosphere. The second type of contacts (S–N, S–N–S) can be divided to *ex situ* (clamping or soldering) and *in situ* (incorporated before final annealing (125). There are different concepts of low resistivity joints and contacts for the superconducting $(\mathrm{Bi,Pb})_2\mathrm{Sr}_2\mathrm{Ca}_2\mathrm{Cu}_3\mathrm{O}_{10}$ wires and tapes. When it is necessary in an application to connect superconducting tape with normal metal, eg, in the case of current leads and ends of any superconducting winding, the low melting point alloys can be used, eg, indium-based. For ceramic superconductors, especially those without metal cladding, making a low resistance and robust connection to a metal lead is a demanding task. In applications where a high current is applied, any measurable contact resistance results in a contact heating that is transferred to the superconductor, degrading its superconductivity. Furthermore, any nonuniformity in the contact can result in hot spot formation that can lead to localized thermal quenching and destruction of the contact decrease of greatly increased power dissipation. In addition, a large contact resistance results in excessive loss of liquid nitrogen during normal operation. The issue of contact formation is especially important in the case of ceramic superconductors, due to their brittle nature with no direct welding, soldering, or fastening possibilities. The contact resistance is one of the important considerations in the application of HTS materials to electrical power leads. Where space restriction prohibit the use of clamping, the connection of the HTS part to the normal metal contact have to be made by soft soldered (because neither welding nor brazing is allowed). From the calculations, the electrical resistances for the soldered S–N connection of 2.5 nW at 4.2 K and 15 nW at 77 K at 20 kA should be possible (126).

3.6.3. Temperature and Field Dependence of Critical Current Density

The critical current is strongly dependent on temperature and field. The temperature dependence for self-field critical currents is in most measurements found to be linearly increasing with decreasing temperature (eq. 52):

$$J_c(T) = J_c(0)\,(1 - \frac{T}{T_c}) \tag{52}$$

with $J_c(0\,\mathrm{K})$ being six to eight times higher than $J_c(77\,\mathrm{K})$ (127). The field dependence is strongly anisotropic with by far the largest suppression for fields perpendicular to the tape. It has been suggested and experimentally confirmed that the critical current density–field dependence can be described for all fields (128) as equation 53.

$$J_c = \frac{J_{co}}{\log(\frac{B_{\mathrm{self}}}{B_{\mathrm{irr}}})}\log(\frac{B}{B_{\mathrm{irr}}}) \tag{53}$$

where J_{co} is J_c in no external field; B_{self} is the calculated self-field generated by the critical current in zero external field; B_{irr} is the irreversibility field, ie, the minimum field where the critical current is zero. This actually says that the J_c field dependence is a simple logarithmic function in B: $J_c \propto \log(B)$. Despite the low irreversibility line for Bi2212 and $(\mathrm{Bi,Pb})_2\mathrm{Sr}_2\mathrm{Ca}_2\mathrm{Cu}_3\mathrm{O}_{10}$ conductors, the effort has been made to align the flakelike grains and improve pinning to improve the irreversibility field by complex texturing processes, eg, rolling and pressing, or even continuous sequential pressing (129,130). The position of the normalized maximum pinning force versus normalized magnetic field is a measure of the kind of pinning mechanism in the superconducting material. It appears that Bi conductors alkaline-earth cuprates, and surface pinning at the grains interfaces distributed in the volume of the superconductor is a source of main pinning. The summary of the current and expected parameters of the most saleable $(\mathrm{Bi,Pb})_2\mathrm{Sr}_2\mathrm{Ca}_2\mathrm{Cu}_3\mathrm{O}_{10}$ conductor is presented in Table 4.

3.7. $\mathrm{Bi}_2\mathrm{Sr}_2\mathrm{CaCu}_2\mathrm{O}_{8+x}$

The $\mathrm{Bi}_2\mathrm{Sr}_2\mathrm{CaCu}_2\mathrm{O}_{8+x}$ compound is highly anisotropic (Table 5) and behaves as a quasi-2D superconductor above a crossover field of 30 mT at 77 K. The $\mathrm{Bi}_2\mathrm{Sr}_2\mathrm{CaCu}_2\mathrm{O}_{8+x}$ superconductor is more anisotropic than $(\mathrm{Bi,Pb})_2\mathrm{Sr}_2\mathrm{Ca}_2\mathrm{Cu}_3\mathrm{O}_{10}$ and also has a lower irreversibility line. The magnetic field diagram for this material is very complex and all thermally driven effects, eg, thermodynamic melting, decoupling, and depinning transitions of the vortex lattice, can be observed. Weak bulk flux pinning at temperatures > 20–30 K, severely limits high field applications of this material to low temperatures.

3.8. Thallium- and Mercury-Based HTS Superconductors

Since the discovery of superconductivity in the Tl–Ba–Ca–Cu–O system, a considerable number of superconducting phases have been reported in the Tl-based system. There are two families of thallium-based compounds that differ by the number of Tl–O layers, m, $m = (1,2)$ and Cu–O layers, n, $n = (1–6)$; $\mathrm{Tl}_m\mathrm{Ba}_2\mathrm{Ca}_{n-1}\mathrm{Cu}_n\mathrm{O}_{2n+m+2}$. Both of these families are reaching high T_c values of 122 K at $n = 4$ for the single Tl–O layer structure and of 127 K at $n = 3$ for the double Tl–O layer structure. In the Tl–Sr–Ca–Cu–O system, superconducting phases with the single Tl–O layer structures $\mathrm{TlSr}_2\mathrm{Ca}_{n-1}\mathrm{Cu}_n\mathrm{O}_{2n+3}$ ($n = 1$,2, and 3) have been reported (131,132). It is known that the addition of Pb and Bi stabilizes most of the Tl-based superconducting phases, and a maximum T_c of 122 K is obtained at the phase $\mathrm{TlSr}_2\mathrm{Ca}_2\mathrm{Cu}_3\mathrm{O}_9$ ($n = 3$). Data in Table 6 represent one family of the Tl-based superconductors where substituting Ba by Sr results in a similar structure and very similar values. The Tl- and Hg-based HTS retain important superconducting features: The highest known critical temperatures 127–163 K and very low thin-film resistance, $R_s < 50\,\mu\mathrm{W}$ at 77 K and 10 GHz. The vast amount of data published in the

Table 4. Present Status and Future Expected Performance of (Bi, Pb)$_2$Sr$_2$Ca$_2$Cu$_3$O$_{10}$ Tapes

Parameter	Value in year 2000	Expected value in year 2004
width	2.5–4.5 mm	1–10 mm
thickness	0.15–0.3 mm	0.15–1 mm
length	1–1.5 km	40–50 %
std. dev. Thickness	5%	<2%
std. dev. Width	2%	<2%
std. dev. I_c batch to batch	6%	2%
std. dev. I_c within batch	2%	1%
price at 77 K self-field	300 ∈/kAm	<100 ∈/kAm
J_c long length typical at 77 K self-field	25 kA/cm^2	50 kA/cm^2
J_e long length typical at 77 K self-field	7 kA/cm^2	25 kA/cm^2
I_c long length typical at 77 K self-field	50 A	150 A
full width at half-maximum (fwhm) c-axis misalignment	10–12°	8–10°
critical strain	0.4–0.5%	0.4–0.5%
critical stress	120 MPa	250 MPa
T_c	110 K	110 K
normal state resistivity of ceramic	3×10^{-4} cm at 300 K	$2–3 \times 10^{-4}$ cm
thermal conductivity of ceramic	2 W/mK at 50 K	2 W/mK at 50 K
thermal conductivity of Ag/HTS tape at 50 K	500 W/mK	500 W/mK
thermal conductivity of Ag11 at%Au HTS tape at 50 K	50 W/mK	50 W/mK
integrated contraction $\Delta L/L_0$ (ab) at 50 K	-1.5×10^{-3}	-1.5×10^{-3}
integrated contraction $\Delta L/L_0$ (c) 50 K	-3×10^{-3}	-3×10^{-3}
thermal contraction tape at 300 K	16×10^{-6}/K	16×10^{-6}/K
thermal contraction ceramic (ab) at 300 K	10×10^{-6}/K	10×10^{-6}/K
thermal contraction ceramic (c) at 300 K	20×10^{-6}/K	20×10^{-6}/K
a–c losses (at 77 K, 50 Hz,100 mT parallel)	0.33–0.40 mWA/m	<0.1–0.25 mWA/m
quench stability at 77 K	$V_{\text{long}} = 0.02$ m/s	$V_{\text{long}} = 0.02$ m/s
joints	2×10^{-7} cm^2	2×10^{-7} cm^2
insulation (10 μm thick)	300 V (between windings)	500 V

literature on the structure and property relationship of both single- and double-layer Tl and Hg compounds has led, not only to the generalization of many features that help in the understanding of their superconducting behavior, but has also brought forward new microwave applications and superconducting electronic devices (133).

3.8.1. $Tl_2Ba_2Ca_{n-1}Cu_nO_{2n+3-\delta}$ Conductors

There are a few characteristic features of the layered structure of the Tl1223 family, which is isostructural with a Hg-based Hg1223 compound. A single insulating layer exists between adjacent blocks of CuO$_2$ layers. Two spacing layers are between adjacent blocks of CuO$_2$ planes. The spacing layer in this structure is composed of Ba and O (apices of the red square pyramids) and two separating layers exist in the block of CuO$_2$ planes. Each

Table 5. Resistivity Values for the *a*, *b*, *c* Axis of the $Bi_2Sr_2CaCu_2O_{8+x}$ Superconductor in Normal State

	ρ(300 K), $\mu\Omega$m	ρ(125 K), $\mu\Omega$m
$Bi_2Sr_2CaCu_2O_8$ (*a* axis)	15	8
$Bi_2Sr_2CaCu_2O_8$ (*b* axis)	6.5	3
$Bi_2Sr_2CaCu_2O_8$ (*c* axis)	1100	650

Table 6. Superconducting Parameters and Structure of $Tl_mBa_2Ca_{n-1}Cu_nO_{2n+3}$ Superconductors

Compound	*m*	*n*	T_c, K	p^a	*a*-Axis	*c*-Axis	Structure
$TlBa_2CuO_{5-x}$[b]	1	1	~10	0.3895	0.9694		
$TlBa_2CaCu_2O_7$	1	2	80	0.217	0.38023	1.2107	p.tetr
$TlBa_2Ca_2Cu_3O_9$	1	3	108–118	0.192	0.381	1.523	p.tetr
$TlBa_2Ca_3Cu_4O_{11}$	1	4	114–121	0.186	0.385	1.873	p.tetr
$TlBa_2Ca_4Cu_5O_x$	1	5	113–106				
$TlBa_2Ca_5Cu_5O_x$	1	6	100				
$Tl_2Ba_2CuO_6$	2	1	0–88	0.270	0.38629	2.3136	b.c tetr
$Tl_2Ba_2CaCu_2O_8$	2	2	87–112	0.212	0.38550	2.9318	b.c tetr
$Tl_2Ba_2Ca_2Cu_3O_{10}$	2	3	116–110[a]	0.135	0.3854	3.588	b.c tetr
$Tl_2Ba_2Ca_3Cu_4O_{12}$	2	4	116–113[a]	0.110	0.3854	4.207	b.c tetr

[a] Number of holes per Cu.

[b] Stoichiometric compound nonsuperconducting, and metallic; superconductivity induced by oxygen removal or partial substitutions. (Courtesy of J. Gopalakrishnan.)

[c] Decreasing order reflects the increase of the critical temperature T_c with oxygen loss $\tilde{\delta}$.

separates the individual CuO_2 layers in the block. The separating layer in this structure is composed of Ca atoms. Three conducting CuO_2 layers are in the conducting block. There is a single square planar layer and one layer at the base of each pyramid. The relation between T_c and oxygen d for $Tl_2Ba_2Ca_{n-1}Cu_nO_{2n+3-d}$ shows that sintering in an oxygen atmosphere overdopes the compounds, introducing an excess of hole carriers. On the other hand, a decrease in the number of excess oxygen atoms leading to a reduction of hole concentration in the conducting CuO_2 planes results in an appropriate carrier concentration and an extremely high T_c (134)

$$T_c/T_{c,\max} = 1 - 82.6(p - 0.16)^2 \tag{54}$$

From the whole family of the Tl-based conductors, the mostly likely to be applied in electrotechnology is Tl1223, due to its high irreversibility line and high T_c. Despite the fact that Tl1223 conductors are superior to YBCO and Bi2223 conductors because of their increased insensitivity to grain boundary misorientation, high irreversibility line, controllability of diffusion formation process, and applicability of the Ag-based substrates, the development of Tl- and Hg-based materials is very restricted due to the new European Union safety issues. Therefore, thin-film technology of the other Tl-based compounds, eg, Tl2212 and Tl2223, is taking over where superconducting layers can be restricted to small electronic devices for the telecommunication market. In this case, toxicity is not as much of issue as it is for kilometer-long coated conductors.

3.9. C_{60}

The C_{60} structure consists of 60 carbon atoms bonded together to form a hollow sphere 0.7 nm in diameter and is a natural insulator. The C_{60} structure has to be chemically altered to become superconducting. When reacted with alkali metals (A = Na, K, Rb, Cs, etc), the behavior of the fullerenes changes dramatically. By adding electrons to the empty conduction band, or removing them from the valence band (creating positively charged holes), the crystals become conductors and, at low enough temperatures, superconductors. Whereas pure C_{60} is a good insulator, Rb_3C_{60} is a metal, conducting electricity reasonably well. The compounds A_3C_{60} are metals and A_4C_{60} are insulators.

3.10. Metalorganic Superconductors

Intensive research on organic conductors arose after Little (135,136) proposed that synthetic materials when properly constructed could show superconductivity with transition temperatures as high as room temperature. In his model, which was an extension of the BCS theory, he discussed the pairing of electrons within an organic, polymer mediated via their coupling to highly polarizable side molecules. Guided by this idea, in 1979 research on organic superconductors resulted in discovery of superconductivity in the quasi-1D Bechgaard salt $(TMTSF)_2PF_6$, where TMTSF = tetramethyltetraselenafulvalene, $T_c = 1.2\,K$ (137). The substitution of the PF_6 complex by other monovalent anions, eg, SbF_6, AsF_6, TaF_6, or ClO_4, create a whole series of $(TMTSF)_2X$ organic superconductors characterized by $T_c < 3\,K$.

Over an extended range in the H–T plane, the magnetization of k-$(ET)_2Cu[N(CN)_2]Br$ is entirely reversible upon increasing and decreasing the field, indicating that the flux pinning is ineffective in this range. Although quasi-2D organic superconductors differ from layered high temperature ceramic superconductors in many respects, it turns out that they share a largely common phenomenon in their superconducting properties. The applicability of the organic superconductors as practical conductors are very limited because of their very weak pinning properties and low T_c. Some exotic applications may be invented in the future, but for now it is more of a physical phenomenon. One of the key quantities, which governs the physics of the superconducting mixed state, ie, the structure and dynamics of the vortex system, is the superconducting coherence length. Both classes of materials possess low carrier concentrations. A very comprehensive source of data describing structural, electronic, and lattice properties of organic superconducting materials has been published by Ishiguro and Yamaji (138).

3.11. Borocarbides

Borocarbides, discovered in 1993, are one of the least-understood superconductor systems of all. It has always been assumed that superconductors cannot be formed from ferromagnetic transition metals, eg, iron, cobalt, or nickel. It is the equivalent of trying to mix oil and water. Yet, the boron and carbon atoms within the molecule seem to act as a mitigator to this unwritten rule. In addition, when combined with elements that have unusual magnetic properties (like Holmium) some borocarbides exhibit what is known as reentrant behavior. Below T_c, where they should remain superconductive, there is a discordant temperature at which they briefly retreat to a "normal", nonsuperconductive state. A reentrant behavior of superconductivity occurs in $HoNi_2B_2C$ compounds because superconductivity is strongly suppressed in the region of the helicoidal magnetic order existence (5.2–6 K).

4. Applications of HTS and LTS Superconductors

4.1. Market Requirements

Despite tremendous efforts in research and development after the discovery of high temperature perovskite-type layered superconductors and the high expectations expressed in market projection, potential electrical commercial applications of these materials are taking off very slowly. Therefore, an update of the original comparative prediction of the market for the low temperature conductors and high temperature superconductors is presented in Fig. 20 where there is no crossover between the LTS and HTS. This is because different applications of superconductivity require the simultaneous fulfilment of diverse thermal, mechanical, and electromagnetic specifications; the potential to operate at higher temperatures is not the decisive factor except

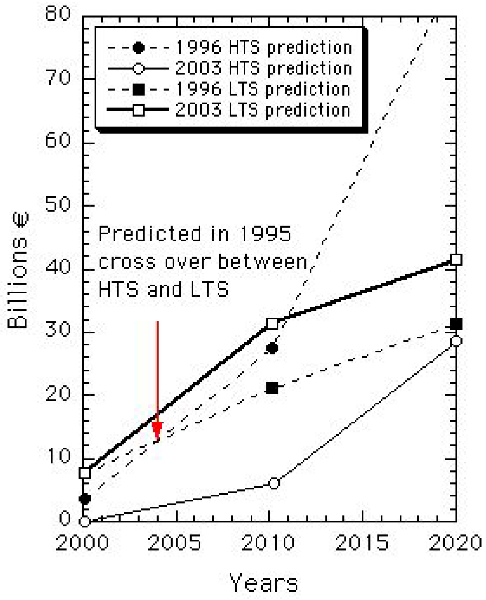

Fig. 20. Projections of the LTS and HTS market that is shared between electronics, power, industrial processing, medical care, and transportation. The 1995 estimate conducted at the International Superconductivity Industry Summit, Yamanashi 1996, unit numbers corrected according to data in early 2003 (solid lines).

transmission lines and transformers. Medical care that is mostly represented by magnetic resonance applications based on LTS will grow, and in 2010 should reach 15 Billion $/year. Oxford Instruments and Oxford Magnet Technology together, routinely use a one-third of all the superconducting material in the world. A chart underlining most of the considered, and in some cases tested, applications of superconductivity is presented in Fig. 21. The ranges for the current density of superconductor versus operating magnetic field required for various areas of the superconductivity application in electric power engineering are presented in Fig. 22.

4.2. HTS Transmission Cables

Advanced research on design and construction of resistive cryocables with vacuum insulation and liquid nitrogen impregnation of multilayer insulation in 60- and 70-ties formed the solid base for rapid development of the concept of superconducting cables cooled by LN_2. The HTS transmission cables that carry current without energy losses will increase the capacity of the transmission system, saving money, space, and energy. Prototype transmission cables are currently being developed by teams led by American Superconductor, Pirelli Cable Company and Southwire Company, Nordic Cable, Siemens, and also by many companies in Japan (Chubu Electric Power & Furukawa Electric Co, 500 m long Superconducting Cable.), Russia and China, 10 KA HTS Cable by CIDEC Research Center of Condumex Wire & Cable Company in Mexico, and also “VNIIKP” (Moscow-Podolsk). Cables have to have a uniform current distribution between the layers. The HTS tapes, made by the PIT technology on the bases of Bi2223, were used. The technology of HTS tape winding ensured degradation of critical current lower than a few percent after the winding. The biggest losses are at the connection junction between the copper current-lead and the cable.

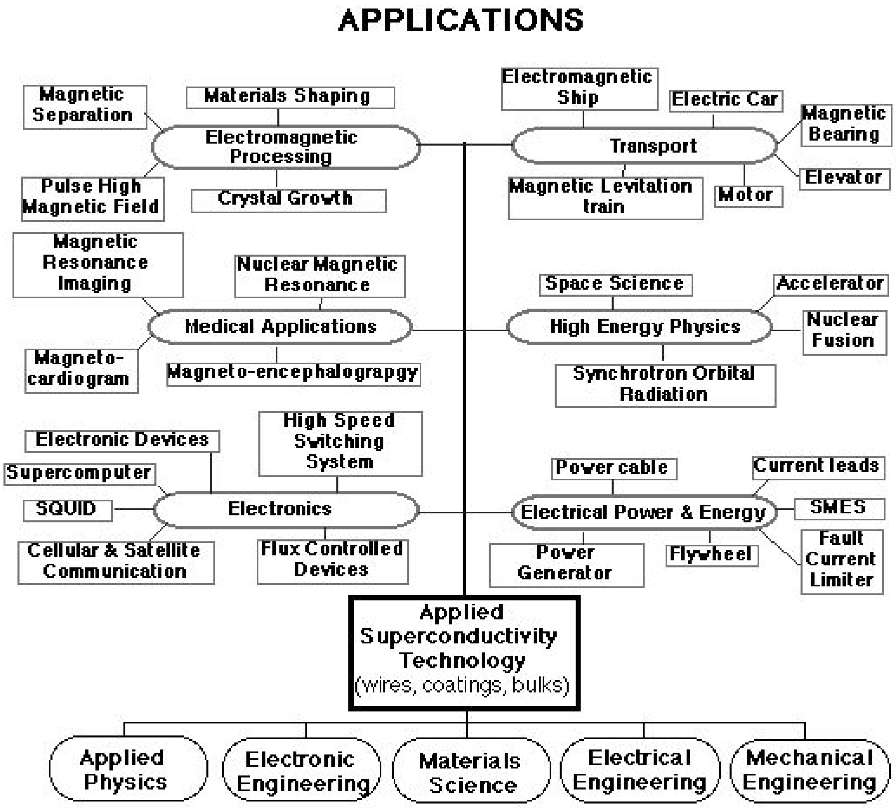

Fig. 21. Chart of all envisaged application of superconductivity across different sectors.

A 100 m long 66 kV, high T_c superconducting power cable system has been developed and tested for a long period by the Tokyo Electric Power Co. & Central Research Institute of Electric Power Industry, Japan. The cable has three cores in a cryostat and cold dielectric configuration. Some properties, eg, the tension of the cable due to thermal contraction, critical current, ac losses, and shield current, have to be measured at each test after the cooling cycle when the cable was cooled from room temperature to an LN_2 temperature for 50 h.

4.3. Research Electromagnets

Resistive dc electromagnets (Bitter electromagnets) use extremely high dc currents flowing in good conductors to generate magnetic fields up to 33 T (139). This method is costly due to high power consumption and is limited by the cooling power of the high pressure water supply around the coils. Alternatively, pulse magnetic fields can be used for the purpose of bulk HTS magnets magnetization, materials processing, and characterization (140). Such pulse magnets can routinely generate fields 40–50 T over a period of 20 ms that can be seen as an advantage for particular applications. Superconducting dc electromagnets avoid the heat dissipation problems of resistive electromagnets, and the major running cost arises from the need to cool the superconductor using liquid helium. The limit on this type of electromagnet is the upper critical field, or more precisely the irreversibility field of the superconducting material. Superconducting LTS electromagnets are presently limited to ~ 20 T. Hybrid electromagnets, which use superconducting magnets to boost the fields from resistive magnets, have reached yet higher fields. There are certain economic facts that are decisive in new technology development

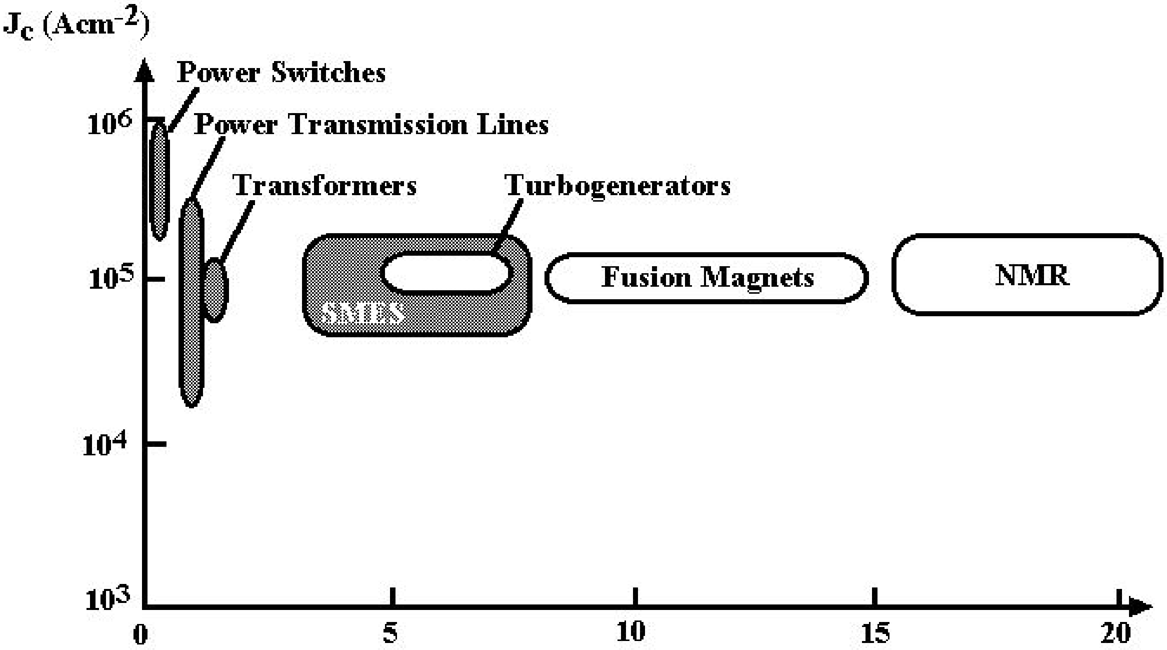

Fig. 22. Ranges of current densities J_c of superconducting conductor versus operating magnetic field required for various areas of superconductivity application. (Courtesy of Prof. P. Komarek.)

and HTS has a tough LTS act to follow: the LTS electromagnets of several tesla are build routinely; liquid helium cryostats for 1.8 and 4.2 K operation are a mature technology; mechanical coolers (and increasingly pulse tubes) can produce useful cooling power at 4.2 K; NbTi is cheap to buy, reliable, reproducible, and easy to work with; Nb_3Sn and Nb_3Al technology has similar maturity (development continue). The cost of Nb_3Sn and Nb_3Al is a greater issue, but new electrochemical Nb-related technologies may dramatically reduce the final cost (56). Finally, processing of Nb_3Sn and Nb_3Al magnets requires care, but is straightforward. In addition, existing commercial LTS conductors can be operated in a truly persistent mode where superconducting current can circulate in the close superconducting circuit without losses due to quality of the conductor and superconducting joints. (1-W dissipation evaporates ~ 1 l/h of He). Previous step jumps in available magnetic fields have depended on improved superconducting material being available. To displace LTS in the existing market with HTS and MgB_2, the combined technology of conductor and cooling must be cheaper. The 1 GHz nuclear magnetic resonance (NMR) system is a good example where high magnetic field ~23.5-T magnets may just be possible using LTS materials, but may prove to be economical if suitable HTS material become available. For fields above this level, new conductor technology is required, eg, $Nb_3(AlGe)$, using electrochemical reduction and infiltration processes, but HTS is possibly the only real future candidate (Table 7). Most of the larger coils in magnets are stress, not J_c, limited. The engineering current density in the range of 100–200 A/mm^2 is adequate for current needs. Further improvement should be made in piece length, joining, persistence, and stress tolerance. If this could be increased, it would enable either higher J_e at lower fields or higher fields at the same J_e.

Currently, additional internal coils are made from HTS Bi2212 pancake coils (141,142). The major constrain on the final performance of the superconducting LTS and HTS materials are (*1*) static stress accumulated during diffusion reaction; (*2*) cool down from reaction temperature to potting temperature $1000 \Rightarrow 300\,K$; (*3*) cool down to operating temperature $300 \Rightarrow 4.2\,K$; and (*4*) large $F_L J_c \times B$ induced by high current and high

Table 7. Electromagnet Systems Manufactured for the Different Field and Temperature Range Require Combination of Different Superconducting Conductors

Magnetic field, T	Magnets	Operating temperature
~10	NbTi	1.8–4.2 K + cryogen free
>19	TNbTi + Nb_3Sn + $(Nb,Ti)_3Sn$	1.8–4.2 K
>20	NbTi + Nb_3Sn + $(Nb,Ti)_3Sn$ + $Nb_3(Al,Ge)$ + Bi2212	4.2 K
2–10	HTS Bi-2223, Bi-2212, MgB_2	20–30 K + cryogen free
>5	HTS YBCO	65 K

magnetic field. One possible use of HTS magnets is in space research where cooling is easy and power requirements and weight constrains are critical.

4.4. Current Leads

Superconducting electromagnets, widely used in numerous applications, require a supply of high current to power the electromagnet. The current is transmitted from room temperature, 273 K, to the required operating temperature ~4 K. In a basic liquid, helium-cooled electromagnet current leads are usually made from a normal metallic conductor and are cooled by vapor from the boiling cryogen. This is an expensive way to power superconducting electromagnets. Because of the low thermal conductivity and high critical current capabilities, the dc HTS superconducting current leads are the first high current application. For some applications, the low T_c of the actual HTS superconductor pose temperature limits at the hot end of such a current lead. In the superconducting part of a dc current lead, $I \leq I_c(T)$, the solid-state heat conduction through the superconductor is inversely proportional to the length of conductor, L, and is the only mechanism contributing to the low temperature heat load. Unlike the dc current leads, an optimum length exists for an ac lead. The hysteretic ac losses, that have to be added are usually proportional to L. The optimum length of the current lead conductor corresponds to the crossover point of the ac load and conduction curves (143).

4.5. Cryogen-Free Electromagnets

Introduction of a so-called cryogen free system based on conductive cooling of the superconducting winding and current leads, by Gifford McMahon cryocoolers, enabled introduction of a wide range of revolving electromagnets. Such a refrigerator-cooled electromagnet is characteristic for its simple operation at temperatures of ~6 or 4 K, because it does not need a special cryogen, eg, liquid helium or nitrogen.

For the magnets using Bi2223 wires, a 20 K refrigerator, which has a larger cooling capacity than a 4 K refrigerator, can be employed, because the Bi2223 wires exhibit a high T_c of 110 K and the J_c-B properties are drastically improved at ~20 K because of a rapid increase of the irreversibility line. The refrigerator-cooled Bi2223 magnets possess the following characteristics: (*1*) easy operation because no cryogen is required (cooling time 20–50 h); (*2*) a compact magnet is feasible by using the good J_c-B properties at 20 K; (*3*) the system is economical and reliable, the cooling efficiency of a 20 K refrigerator is five times higher than that of a 4 K refrigerator; (*4*) stability is significantly improved, because the specific heat of Bi2223 at 20 K is 100 times larger than that at 4 K, and the T_c is sufficiently high (144); (*5*) high cryogenic stability, very large disturbances are needed to increase the magnet temperature, and the slight increase of the coil temperature does not cause critical situation (145). For the magnets using LTS superconducting wires, 5 K refrigerators can be used to enable a respectable magnetic field of ~15 T, which can be used in the complex materials processing and characterization. The superconducting coil is a hybrid coil composed of a Nb_3Sn and NbTi coil. The main parameters of the coil and the superconducting conductors are shown in Table 8.

Table 8. Parameters of a 15.1 T Liquid Helium-Free Superconducting Electromagnet System with a Room-Temperature Bore of 52 mm[a]

central field	15.1 T
room-temperature bore	52 mm
dimensions outer diameter	830 mm
height	1221 mm
weight	720 kg
current lead	$(Bi, Pb)_2Sr_2Ca_2Cu_3O_{10}$ tape
GM cryocooler cooling capacity of first stage	37 W at 40 K
cooling capacity of second stage	1.0 W at 4.2 K

[a] Ref. 146.

4.6. Electromagnetic Assisted Material Processing

Electromagnets for a large diameter (8 in. by 12 in., 20.32 by 30.48 cm) silicon single-crystal pulling apparatus using the horizontal magnetic Czochralski method are manufactured in large numbers using low temperature superconducting conductors of NbTi. The magnetic field requirements are not critical: magnetic field is low $B \sim 0.4$ T, operating current ~ 150 A, and bore diameter is 1.2–1.5 m. These magnets do not need to operate in a persistent mode, therefore, superconducting switches are not needed. The profit made on such a unit is much higher than on an mri magnet. Similar silicon single-crystal pulling electromagnets have been manufactured mostly in Japan from HTS Bi2223 superconducting wires (294). The special feature of the magnetically assisted Czochralski method of single-crystal growth is a magnetic field used as an extra control parameter for crystal growth. The magnetically assisted Czochralski method of single-crystal growth has three variations of different magnetic field shape: (*1*) vertical magnetic field-type (VMC); the molten silicon is forced by the interaction between the flow and the magnetic field. This interaction affects the flow pattern and consequently the resulting crystal; (*2*) horizontal magnetic field-type (HMC), silicon is molten by conductance heating. This is easy to achieve a highly purified single crystal. This method can make extra low oxygen concentration silicon crystals, but it is not easy to enlarge the diameter of the crystal; (*3*) cusp-shaped magnetic field-type (CMC); the cusp-shaped magnetic field is generated by two electromagnets facing the same poles. The effect of the cusp field is that it generates less magnetic flux at a crystal–melt interface than at the other part of the melt and it has parallel magnetic flux to the melt surface and coaxial shape to the crystal growth axis at the same time. Development of cryogen-free superconducting magnets for the semiconductor industry to grow 12 in. (30.48 cm) silicon single crystals is being conducted by Toshiba Corporation and Shin-Etsu Handotal Co.

4.7. Electromagnets for Nmr and Mri Systems

Nuclear magnetic resonance is the fundamental analytical tool in biomedical research, synthetic chemistry, neurology, food analysis, and human diagnostics and *in situ* imaging of human organs during complex invasive operations. It is also a valuable tool in basic physics research. If an atom has an odd number of protons and neutrons, it will have what is known as a “magnetic moment:” it will spin, and its axis will tilt in a certain direction. When that tilted nucleus is put into a magnetic field, the axis of the tilt will change, and the nucleus will also wobble at a certain speed. If radio waves are then beamed at the wobbling nucleus at just the proper wavelength, they will cause the wobbling to intensify; this is “magnetic resonance” phenomenon. The resonant frequency is known as the Larmor frequency, and the Larmor frequencies vary for different atoms. There is a correlation between the characteristic frequency and magnetic field required for certain elements to be used as a tester. A field of 2.35 T corresponds to a proton frequency of 100 MHz. Hydrogen, eg, has a Larmor frequency of 42.58 MHz. Therefore the minimum required dc magnetic field in the case of hydrogen could be 1 T. Hydrogen, which is a major constituent of water and of carbohydrates, eg, fat, is very common in the human body. If radio

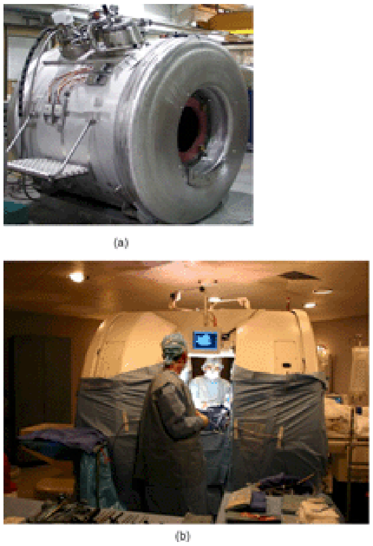
(a)
(b)

Fig. 23. A split-coil mri machine for real-time imaging during operation, the display on the monitor presents cross-section of the patient's scull (147). (Courtesy of Oxford Magnet Technology plc.)

waves at this Larmor frequency are beamed into magnetized hydrogen atoms, the hydrogen nuclei will absorb the resonant energy until they reach a state of excitation. When the beam goes off, the hydrogen nuclei will relax again, each nucleus emitting a tiny burst of radio energy as it returns to its original state. The nuclei will also relax at slightly different rates, depending on the chemical circumstances around the hydrogen atom. Hydrogen behaves differently in different kinds of human tissue. Those relaxation bursts can be detected, timed, and mapped. The powerful magnetic field within an mri machine can permeate the human body; but the resonant Larmor frequency is beamed through the body in thin, precise slices. The resulting images are neat cross-sections through the body. Unlike X-rays, magnetic resonance does not ionize and possibly damage human cells. Instead, it gently coaxes information from many different types of tissue, causing them to emit signals about their chemical makeup. Blood, fat, bones, tendons, all emit their own characteristics, which a computer then reassembles as a graphic image on a computer screen. One of the advanced applications of the sophisticated mri scanners is real-time imaging of the area of interest during real-time operation. To provide *in situ* real-time imaging during an operation, an intraoperative "walk-in" mri machine was developed (Fig. 23), where the surgeon can operate while consulting instantaneous cross-sectional images of the patient's anatomy. Superconducting mri is expensive, but can easily generate 0.5–2-T fields, allowing for high quality imaging (147). Magnetic fields $> 3\,\mathrm{T}$ have not been approved for use in medical imaging of the human body. There have been attempts to use split-coil electromagnets with HTS Bi2223 coils, but this type of machine requires further development to prove it is competitive with very well developed LTS mri instruments.

An integral part of the mri magnet working in a so-called persistent mode is the superconducting switch. The role of the superconducting switch is to minimize the heat transfer along the current leads from room temperature to the low temperature zone where usually temperatures are closer to 4 K are required. By enabling current to flow in a resistance less superconducting circuit, the losses of liquid helium are negligible and the mri magnet may work in a persistent mode for years without refilling, supported only by cryocoolers and protected from warming up by superinsulation adopted from space applications. The superconducting switch is manufactured with the superconducting bridge material that is connected to the main field generating coil by the superconducting permanent joints. A superconducting switch is placed away from the magnetic

Table 9. Designed Specifications of an Outer LTS Electromagnet in a 1-GHz Superconducting NMR Spectrometer

operating current	256 A
maximum outer diameter	872 mm
maximum height of windings	1600 mm
cold bore diameter	132 mm
weight of Nb_3Sn conductors	1346 kg
weight of Nb–Ti conductors	3262 kg
inductance	1111 H
stored energy	37 MJ

field generated by the field coil to improve its performance since the joints are the weakest point of the fully superconducting circuit. There are three major stages of implementation of the persistent mode using a superconducting switch:

(1) Transport current generated by the power supply at room temperature is passed to a superconducting electromagnet. A superconducting bridge is driven to a normal state (NS) by the application of the local magnetic field or by increasing the temperature or a combination of both.
(2) Once the desired value of the current is reached in the superconducting field coil, the bridged material is reversibly transferred to the superconducting state by removal of the heat or magnetic field in the control coil. From this moment, the power supply can be switched off, because the continuous superconducting circuit has been established.
(3) At this stage, current leads can be mechanically disconnected from the internal electromagnetic magnet coil (persistent mode) so the thermal link between a fully superconducting circuit and room temperature can be disconnected.

Paradoxically, considering the wide use of magnetic resonance, it is a relatively insensitive spectroscopy because the energy of the radio frequency photon is so small and must compete with strong sources of the background noise. Luckily, this is not a problem for the whole body mri scanners where there are a large number of nuclear spins as high as 10^{28}. In the case of small biochemical samples considering lack of sensitivity that vary as B^2, where B is the applied field, intensive effort has been put into increasing the photon energy in the case of small mass samples by using systems equipped with very powerful electromagnets ~ 20 T.

Different Nb-based superconductors are suitable for use in nmr magnets working at different frequencies. The NbTi multifilament wire is used exclusively in the case of magnets generating a field between 7 and 9.5 T because NbTi is less expensive, it needs no thermal heat treatment, and it is much less brittle and thus easier to wind. Use of nb_3Sn in this field range is not economical. Above 9.5 T a hybrid design is used, where the inner part of the coil is wound with Nb_3Sn multifilamentary wire. For field regions between 9.5 and 12 T, only Nb_3Sn is used. For field regions > 12 T the material of choice is $(NbTa)_3Sn$ or $(NbTi)_3Sn$. The limits are defined by the $J_c(B)$ characteristic of the respective conductors used in magnets. However, the systems working in persistent mode with superconducting switches do not require any better conductors than NbTi because the required magnetic field should not be > 2–3 T. The 1-GHz spectrometer requires hybrid magnet systems and is 10 times more powerful. It is also > 30 times more expensive than standard mri (148). In new designs working at frequencies > 1 GHz, there are real possibilities of use of internal HTS coils as specified in Tables 9 and 10. The mri machines enhance medical diagnostics by imaging internal organs, often eliminating the need for invasive surgeries. These MRIs, which currently are made with low temperature superconductors, will be smaller and less expensive when made with an HTS electromagnet or coil.

Table 10. Parameters of the Research and Development Insert Electromagnet for the Spectrometer

material of conductor	Ag-sheathed Bi-2212 tape (or preferentially wire)
number of filaments	19
size of conductor	5 × 0.25 mm
non-SC/SC ratio	3.3
number of double pancakes	4
winding method	Wind and react
inner diameter	16.5 mm
outer diameter	44.5 mm
height of winding	46.5 mm
number of turns	28

4.7.1. A Semiportable MRI System with a Superconducting Receiver Coil

Conventional mri scanners use superconducting magnets and a high field, however, although the actual resolution of the images is excellent, there are high capital cost, running cost, and space requirements. There is an interesting alternative concept of using superconducting receiver coils for mri systems that require only a very weak constant magnetic field on the order of tenths of millitesla, which can be easily generated by nonsuperconducting magnets. In any case, the critical parameter for image quality is the signal / noise ratio. There are two main contributions to the noise / coil noise (noise due to the resistance of the receiver coil) and body noise (noise due to the object under investigation, the patients body). At lower fields the receiver coil noise dominates, whereas at higher fields body noise dominates. In order to recover the signal lost by using a low magnetic field, a receiver coil has to be made from a superconductor. Such a concept was successfully developed by a U.K. team (149) to create mri images of the parts of human body where a constant 150 mT external magnetic field was generated by a nonsuperconducting $YBa_2Cu_30_7$ wire. The future goal is to develop a fully operational alternative mri system with a very low field (as low as 15 mT). Since scans are taken over only 17 s in duration with a $YBa_2Cu_30_7$ coil, this rapid acquisition imaging could be particularly useful when imaging children.

There is also interesting research taking place, which is aimed at lowering the magnetic field needed for experiments. This procedure is not yet at the application stage, but shows the potential of the magnetic resonance techniques. It was shown that by prepolarizing the nuclei in the field of a few militesla, which is switched off before resonance observation is conducted, it was possible to observe proton magnetic resonance in a liquid sample at a frequency of ~ 100 Hz. In this case, SQUID was used to detect individual flux quanta, Φ_o in equation 1, rather than the receiver coil to measure changes in flux (150).

It can be concluded that magnetic resonance requires superconducting materials and devices irrespective of the magnetic field intensity used. At high magnetic fields, very sophisticated composite wires and switches are needed. At low fields, superconducting receiver coils are needed, where at very low fields SQUID is required.

4.8. Magnetically Guided Surgical Instruments

Oxford Research Instruments has built magnets for a revolutionary new system allowing surgeons to guide instruments magnetically through the brain, and potentially through other sensitive parts of the body, without resort to conventional surgery and stereotactic frames. The magnetic surgery system has been developed by Stereotaxis, Inc. of St. Louis, Missouri, and is currently being investigated as a potentially less invasive, yet more effective way to biopsy brain tumors and carry out interventional neuroradiology and cardiovascular procedures. Magnetic surgery is fundamentally new and continuing to develop. A magnetic tip attached to a fine flexible guidewire or catheter is guided through the brain by rapid adjustments to the magnetic fields of three superconducting magnets placed around the patient's head. A real-time X-ray image, showing two planes of the head, provides the surgeon with direct, visual control of the tip. Position is determined to within 1 mm, with the potential for a curved path in an attempt to avoid vulnerable areas. Once in position the magnetic tip is withdrawn, enabling a flexible biopsy tool to be inserted. The magnet consists of three 5 T, 40-cm diameter superconducting coils, mounted at right angles to each other about the patient's head. The degree of control required demands extremely rapid alteration of the magnetic field (a high sweep rate), and thus, very high voltages from the power supply and high grade superconducting wire. The magnets are subjected to high stresses during the rapid and frequent cycling of the field (151).

4.9. Accelerators

4.9.1. Large Hadron Collider

Superconducting magnets have been intensively used for high energy particle accelerators in many recent accelerator projects. Most of the constructions were with superconducting magnets made of NbTi alloys. However, the use of metallic compound conductors are expected to come into use in accelerator projects in the near future. The energy frontier of the particle accelerator is now at the construction of the Large Hadron Collider (LHC). This accelerator uses 1232 superconducting dipole magnets cooled by a 1.8 K superfluid, to generate 8.33 T. The original thought of LHC was to generate l0 T by an alloy conductor with intensive cooling. The operation field has been reduced to assure the operation.

The aim of the LHC accelerator, when in function in 2005, is to collide protons head on, at energies of 7 TeV, for the production of otherwise inaccessible heavy constituents of matter. At CERN, the superconducting cables are used in the dipole and quadrupole magnets of the LHC, which is now under construction. The dipole magnets bend the particles to keep them on their right track. The quadrupole magnets focus the particles exactly on the right spot on their track. In the 27-km long underground tunnel, there are two vacuum tubes where the particles are accelerated almost at the speed of light and collided on certain places along the ring. These collisions are examined in detectors, where one of the key components is a superconducting magnet. In addition, two new detectors are under construction at CERN, ATLAS, and CMS (Compact Muon Solenoid). The strands for the CMS conductor have been supplied by Outokumpu Superconductors (probably the only manufacturer that has been able to meet the set requirements). In addition to superconductors, very demanding, high quality copper products, eg, hollow conductors and copper wedges, are needed for the LHC project.

With the evolution of compound materials, natural development is in the direction of compound materials at a higher field. However, the requirement for the particle accelerator has been changing. Physics prefers to do experiments with "simple" leptons rather than hadrons, which have the "complicated" structure of three quarks. Circular accelerators with high field ending magnets generate too much synchrotron radiations at this high energy. The Lepton accelerator has to be built in a linear acceleration machine. Even for the hadron accelerator, it is necessary to limit the magnetic field to $<$ 11 T (152).

4.9.2. Linear Collider

The linear collider (153) does not use bending magnets, but has the possibility of using superconductivity. In general, a higher frequency is advantageous to generate a large acceleration field. However, the superconducting cavity is frequency limited because of BCS resistance. Superconducting cavity development has been on L-band (154). The acceleration field of the X-band normal cavity is larger than that of the L-band superconducting cavity. The superconducting cavity also has the disadvantage of a 2 K superfluid operation. The HTC superconductors were expected to solve problems, but were found to have a high grain boundary resistance due to the strong anisotropy. The recent discovery of the MgB_2 superconductor, characterized by low surface resistivity, gives a new aspect to cavity application (155). Although the critical temperature of MgB_2 is much lower than High Temperature Superconductors, $T_c \sim 39$ K is high enough to operate a cavity at 4.2 K with a C-band microwave. The nature of this superconducting material gives no grain boundary problem. Moreover, high thermal conductivity at the critical temperature contributes to the stability of cavity operation.

Table 11. Specification of a 5 GWh SMES System[a]

stored energy	5000 MWh
output Power	1000 MW
aluminum structure	~25,000 tons
conversion efficiency	~0.95
cryogenic loss	~6 MW
overall efficiency	~0.91
conductor:	
conductor length	~500 km
material	Nb_3Sn at 4.2 K
weight	~25000 tons
no. turns	~330
size	21 × 10 cm
cost[b]	3 billion £
coil:	
no. Coils	3
diameter	400, 376, 400 m
coil height	10.8, 18, 10.8 m
burial depth	150 m
magnetic field at the ground surface[c]	>25 mT
current	707 KA
peak field	8.4 T
inductance	71.8 H

[a] Ref. 157.

[b] Conductor stands for ~20% of the grand total cost.

[c] To achieve 1 mT at the ground surface, the diameter should be 1500 m. There is no significant difference for the dipper burial up to 750 m.

4.10. Superconducting Magnetic Energy Storage

The superconducting magnetic energy storage (SMES) system is expected to play an important role in future power systems, eg, power conditioning, load leveling, and power stabilization and energy storage (Table 11). The SMES is capable of controlling active and reactive power simultaneously, rapidly, and smoothly (157). Since the output power of the photovoltaic power generation system is greatly influenced by the weather, some type of new SMES energy storage system is indispensable to the independent photovoltaic systems. However, for the power-grid-connected photovoltaic system a current transforming circuit is to be put between the solar cell and the superconducting coil (156).

4.11. HTS Transformers for Higher Performance Trains

Siemens, together with GEC-Alsthom, built a single-phase prototype of a superconducting train transformer with a capacity of 1 MW. This is an important step on the way to future applications that require 10 MW transformers. Development effort was particularly focused on optimization of the HTS Bi2223 tapes in respect to long-term cryogenic stability and ac losses.

The reason for the development effort is that conventional transformers pay for optimized weight and volume with transmission losses of ~ 10 %, whereas transformers based on HTSC offer a number of advantages. For the same volume, they handle more power, have a lower weight per unit power, and lower losses. At 98%, their efficiency is ~ 8% higher than that of conventional train transformers. Since the situation with high speed train locomotives is getting very competitive and further improvement of conventional on-board transformers is virtually impossible, the future can be in superconducting transformers.

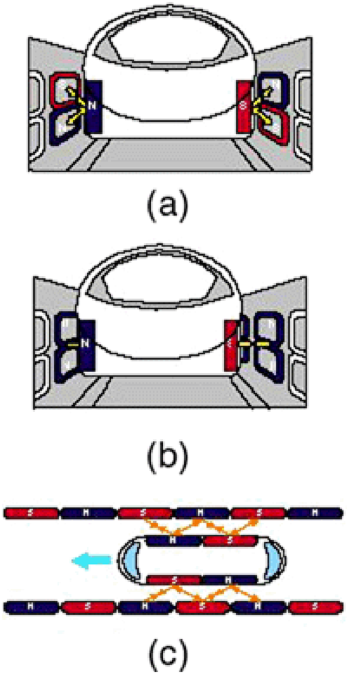

Fig. 24. Schematic representation of the three basic interactions of the superconducting and track coils in a MAGLEV train: (**a**) principle of magnetic levitation; (**b**) principle of lateral guidance; (**c**) principle of propulsion. (Courtesy of Railway Technical Research Institute, Tokyo.)

4.12. Superconducting Levitating Train, MAGLEV

The MAGLEV trains seem to float on air as a result of using superconducting magnets. These trains have been under development in Japan for two decades. The MAGLEV is a transportation system in which the vehicle runs levitated from the guideway (corresponding to the rail tracks of conventional railways) by using electromagnetic forces between superconducting electromagnets made from the LTS wires on board the vehicle and normal metal electromagnetic coils on the ground. One of the perspective designs of the superconducting magnets for the MAGLEV train is a racetrack coil made of HTS wires similar to the shape of LTS wires, but made from normal metal and placed on the ground. The following is a general explanation of the principle of MAGLEV, Fig. 24.

The principle of magnetic levitation (Fig. 24**a**): The “8” shaped levitation resistive coils are installed on the sidewalls of the guideway. When the on-board superconducting magnets pass at high speed about several centimeters below the center of these coils, an electric current is induced within the coils, which then acts temporarily as an electromagnet. As a result, there are forces that push the superconducting magnet upward, and ones that pull them upward simultaneously, thereby levitating the MAGLEV vehicle.

The principle of lateral guidance (Fig. 24**b**): The levitation coils facing each other are connected under the guideway, constituting a loop. When a running MAGLEV vehicle, ie, a superconducting magnet, displaces laterally, an electric current is induced in the loop, resulting in a repulsive force acting on the levitation coils of the side near the car and an attractive force acting on the levitation coils of the side farther apart from the car. Thus, a running car is always located at the center of the guideway.

The principle of propulsion (Fig. 24**c**): A repulsive and an attractive force induced between the magnets are used to propel the vehicle (superconducting magnet). The propulsion coils located on the sidewalls on both sides of the guideway are energized by a three-phase alternating current from a substation, creating a shifting magnetic field on the guideway. The on-board superconducting electromagnets are attracted and pushed by the shifting field, propelling the MAGLEV vehicle. For the superconducting LSM, the ground coil is an essential element corresponding to the armature in the conventional motor and to the conventional rails. The ground coils come in two types: propulsion coils to propel the vehicle and levitation coils serving both to levitate the vehicle and to guide it laterally. When electric current flows in these coils fitted to the guideway, the MAGLEV vehicle can run. The actual train is equipped with four pairs of rubber wheels similar to those on an airplane. The four wheels under the carriage are to provide a means of rolling support for the carriage during the initial acceleration to the level at which the magnetic levitation becomes sufficiently effective to lift up the train. The side four wheels are to provide simultaneous lateral guidance. The trial operation of the 18.4-km long Yamanashi MAGLEV Test Line, which was constructed in 1997, is still underway. The newest prototype with its record high speed of 552 km/h (in ambient air) has already run > 140,000 km with > 18,000 trial passengers. There is a plan to conduct experiments in a air evacuated tunnel where in the absence of the friction force, the maximum estimated speed to be reached is 2800 mile/h. In future, this concept may be an ultimate traveling means. Most of the information concerning the future development of superconducting trains can be found on the Railway Technical Research Institute, Tokyo home page, http://www.rtri.or.jp/.

4.13. Flux Pumps

In normal circumstances, current has to be supplied to the superconducting field coil from an external source, which presents some problems due to heat leak, ohmic losses, maintenance of mechanical and electric contacts, etc. A so-called flux pump system indirectly feeds the superconducting field coil with an adjustable direct superconducting current at working temperature. Hence, once a current is feed into the circuit, the current becomes a “persistent current”, ie, keeping at the same current level forever as long as superconducting joints are of a high quality.

4.14. Bulk Materials Applications

Electromagnetic applications for bulk materials can be classified into two types: (*1*) passive applications, in which an external magnetic field is used as the magnetic field source; and (*2*) active applications, in which the bulk superconductor itself acts as the magnetic field source by trapping a strong magnetic field.

4.14.1. Passive Bulk Applications

When an external magnetic field is applied to a superconductor that exhibits the pinning effect, the magnetic flux is trapped near the superconductor’s surface. This phenomenon allows a strong, but imperfect diamagnetism, to be obtained.

Superconductors that exhibit the pinning effect can be used to produce stable levitation by utilizing the magnetic flux that is trapped within the superconductors. The repulsive force can be expressed as equation 54.

$$F = M(dH/dx) \tag{55}$$

where dH/dx is a field gradient and M is the diamagnetic magnetization. This phenomenon differs from the mutual repulsion of permanent magnets. Furthermore, superconductors that can trap a large magnetic flux can be stabilized at any position in space and made immovable.

4.14.2. Fixed Levitation

One example of an application that utilizes this levitation phenomenon is the liquid hydrogen tank levitation system that was recently developed in Germany. In this application, the superconducting bulks are used as part of the heat insulation system. The liquid hydrogen tank is levitated using the repulsive force that is produced between the superconducting bulks (installed within the tank) and the externally installed permanent magnets. Superconducting materials that utilize the pinning effect allow a stable levitated position to be maintained because part of the magnetic flux is trapped by the surface of the superconductor (158). With this type of levitation a large restraining force (an electromagnetic force) is produced in the direction where the magnetic field changes. The system was designed to prevent the vaporization of hydrogen that can occur as a result of heat conduction. The liquid hydrogen tanks will be mounted on vehicles, eg, automobiles, that are expected to use liquid hydrogen as fuel in the future. Since the tanks are used to store liquid hydrogen, no additional equipment is necessary to cool the bulk superconductors. Heat insulation has been improved by $> 50\%$ using this superconducting levitation system.

4.14.3. Stabilized Levitation

Superconducting levitation systems that utilize permanent magnets have the advantage of allowing stabilized levitation without the need for additional control systems. Applications of this levitation system in flywheels for energy storage utilize this feature to attain zero loss on a free run. However, the load carrying force is limited when permanent magnets are used as the external magnetic field source. Moreover, the levitation gap cannot be adjusted. For this reason, a levitation system is designed that allows both the load carrying force and the levitation gap to be controlled using electromagnets as the external magnetic field source (159,160). Such a system has the advantage of allowing the levitation mechanism to be adjusted by the application of an external electric current, although a certain amount of energy must then be consumed. This control mechanism could theoretically be fitted to a conveyor system, eg, to manufacture a linear elevator. However, when normal conducting electromagnets are used, the intensity of the generated magnetic field is limited. Furthermore, a large amount of electrical power is required. A combination of bulk superconductors and superconducting electromagnets are thus more suitable. The use of superconducting magnets alone is of course also possible, but in this situation an additional mechanism is required to ensure stability. A combination of superconducting magnets and bulk superconductors could be used to produce a magnetic field of 5 T. A field of this strength could then be used to generate a load carrying force with a surface pressure of ~ 100 kg /cm^2. At present, the largest surface pressure attainable using permanent magnets is ~ 1 kg/cm^2. Thus, the electromagnetic force could be enhanced 100 times by using the above combination of superconducting products. This large electromagnetic force could then be utilized to fabricate an ultrahigh power actuator with low power consumption. While superconducting magnets with the strength of 7 T have been fabricated using $Bi_2Sr_2CaCu_2O_8$ tapes (161), the only superconducting magnets that are commercially feasible (at the present time) are composed of low temperature superconducting wires. The use of low temperature superconducting coils is of course also possible, but the potential of this application would be vastly increased if high temperature superconducting electromagnets operating at the temperature of liquid nitrogen became commercially feasible. In addition, an active control system would require that the magnetic fields generated by the superconducting magnets also be adjustable. Consequently, high temperature superconducting electromagnets with a high degree of stability would also be advantageous from this point of view (162). Due to the very strong magnetic fields that can be trapped by bulk superconductors, even at high temperatures one of the perspective designs of the superconducting magnets for the MAGLEV train is to substitute superconducting bulk magnets for the race track type superconducting coils that are presently being used in magnetically levitated train systems (163). If the race track coils are replaced with large-scale bulk superconductors without changing the design, the size of the required coils would be $\sim 50\,\text{cm} \times 1\,\text{m}$. However, the production of bulk superconductors on such an ultralarge scale presents several difficulties and superconducting joining technology is not a matured technique yet (164). Therefore the use of several superconducting bulk magnets in place of a single race track superconducting coil should be considered. The strength of the actual bulk superconductor can also be increased through silver doping (165). Furthermore, the strength of bulk superconductors can be improved by vacuum-impregnating them with an epoxy resin (162). The performance of bulk superconductors is steadily improving, and the specifications outlined above should be attainable. However, for commercialization, an efficient excitation technique is also necessary. The direct excitation method would require the installation of a large superconducting coil excitation systems in relay base stations. Cooling would then be performed in the presence of a magnetic field. However, these facilities would be very large, and maintenance would be dificult. Therefore, various methods for enhancing trapped magnetic fields through repeated excitation can be used (166). Energy storage in both flywheels and superconducting magnetic energy storage systems will ensure the quality and reliability of the power transmitted to utility customers. In addition, energy storage provides utilities with cost savings by allowing them to store energy when the demand for electricity is low and generating the power is cheap. This stored energy is then dispensed when demand is high and power production is more expensive. In the heart of the flywheel is a superconducting magnetic bearing (167).

4.14.4. Fault–Current Limiters

The superconducting fault current limiter (FCL) is particularly attractive since no conventional limiting device exists for high voltage networks and thus corresponds to a real need. In general, there are two types of fault–current limiters: resistive and inductive. Currently, the most promising one is the resistive type. Fault–current limiters help utilities deliver reliable power to their customers. The HTS fault–current limiters detect abnormally high current in the utility grid (caused by lightning strikes or downed utility poles). They then reduce the fault–current, so the system equipment can handle it. A U.K. team recently patented and produced a successful working prototype HTS fault–current limiter based on Bi2223 CRT rods, which is going to be produced by VA TECH Strategic Technology Group (168). The same bars can be used as efficient current leads for cryogen-free magnet applications. In 2000, ABB successfully tested a one-phase 6.4-MVA prototype based on stacks of Bi-2212 thick film meander composites (169). The 5-m long meanders are structured from Bi-2212 sheets ($0.1\,\mathrm{m}^2$) fabricated with ABB proprietary technology and are reinforced with steel bypasses and reinforced plastic composite to avoid "hot-spots" and enhance mechanical stability.

The $YBa_2Cu_3O_7$ compound is also a good candidate for current limitation due to its large critical current density and its large normal state electric fields. However, this material is very sensitive to hot spots in liquid nitrogen. An operation at higher temperatures decreases the critical current density and consequently reduces local heating (hot spots). Tests in liquid argon (87.3 K) were carried out on a monodomain, and the critical current density remained large ($\sim 50\ \mathrm{MA/m^2}$, 0 T). It is the first example where a nondestructive quench was observed in a bulk $YBa_2Cu_3O_7$ monodomain sample. The power and energy per unit volume developed during the transition reached, respectively, $75\,\mathrm{GW/m^3}$ and $350\,\mathrm{MJ/m^3}$. These values are large enough to induce an effective current limitation and weak enough to restrict overheating and resulting destruction (170). Not only was a bulk HTS used as a FCL switching element, but a very successful $YBa_2Cu_3O_7$ thin-film superconducting fault–current limiter demonstrator was also manufactured by Siemens (171).

Superconducting electronics can provide many high performance devices for communication applications, from wideband low temperature superconducting Josephson junction-based analog-to-digital converters (172) to narrowband high temperature superconducting preselected filters. Many of these applications can provide very low insertion loss, or unsurpressed sensitivity or dynamic range, due to the use of superconducting components. Such high performance superconducting components are vulnerable to damage or destruction if exposed to high power transient signals, eg, lightening strikes or unintentional radar illumination. The use of conventional power limiters (173) to reduce such risk in practical applications could lead to increased insertion loss, or a signal reduction in dynamic range or bandwidth, compromising the advantage of using superconducting components. Recent development of a power limiter can protect the superconducting electronics without compromising the performance (174).

4.14.5. Active Bulk Applications

Superconductors that exhibit the pinning effect are capable of trapping the magnetic field. The intensity (M) of the trapped magnetic field is given by equation 82:

$$M = A I_c r \tag{56}$$

where A is a constant that is dependent on the shape of the bulk material, I_c is the critical current, and r is the size of the loop through which the critical current flows. Thus, the intensity of the trapped magnetic field may be increased by enhancing the pinning effect of the bulk superconductor, also improving I_c. Fabrication techniques for producing large bulk superconductors that do not contain any weak links are also important. These characteristics have undergone extensive improvements as a result of progress in bulk superconductor processing. Trapped magnetic fields as high as 10 T have already been attained at 50 K (175). At the temperature of liquid nitrogen, a trapped magnetic field of 2.1 T has been obtained using a $SmBa_2Cu_3O_7$ superconductor (176), while a trapped field of 3.7 T has been obtained using a neutron-irradiated $YBa_2Cu_3O_7$ superconductor (177). Recent experiments indicate that trapped magnetic flux in a $YBa_2Cu_3O_7$ disk ban be 1 T at 78 K, 9 T at 45 K, and 17 T at 29 K (178). Superconducting bulk magnets can generate much higher magnetic fields than permanent magnets of the same size. Consequently, they have attracted much attention for their potential functionality. However, superconducting magnets also have the disadvantage of requiring a cooling system. To utilize trapped magnetic fields effectively, cooling mechanisms must be developed in conjunction with excitation technology. Once these technical challenges have been resolved, superconducting bulk magnets can be applied to a variety of fields where permanent magnets are presently in use. The higher fields attainable with superconducting magnets will allow the performance of these conventional systems to be vastly improved. A trapped field in bulk superconductors should be considered in a similar manner to that produced by a solenoid, since it is generated by currents flowing over the length scale of the material, rather than by aligned electron spins. It is well known that the field at the end of a long solenoid reduces to one-half that at its center. Hence, the flux density at the surface of a long bulk superconductor of diameter 1 cm carrying 50 kA/cm^2 at 77 K, eg, may be estimated to be ~ 3 T, which is significantly greater than that achievable with iron-based magnets.

4.14.5.1. Superconducting Motors and Generators. Motors and generators made with superconducting wire will be smaller and more efficient. A 400-hp motor is being developed by an SPI team led by Reliance Electric Company. Generators will use superconducting wire in place of iron magnets, making them smaller and lighter. New generators also may get more power from less fuel. An SPI team led by General Electric is developing a 100-mV-A generator.

A much smaller electric current can be used to generate an equivalent output (torque). Alternatively, a much larger output can be obtained with the input of an equivalent electric current. Consequently, superconducting bulk magnets have enabled the development of motors with previously unattainable outputs. Superconducting bulk magnets must be built into the motors beforehand and are excited after they have been cooled. As a result, magnetization using pulsed magnetic fields is being investigated because this method does not require a large amount of space or a lengthy period of time. With this method, the bulk superconductors are wound with a coil and installed in the motor. The superconductors are then excited by the application of an external pulsed magnetic field (140,179). With pulsed magnetization, the required magnetic field intensity is, in principle, almost twice what the bulk superconductor is capable of trapping. However, the generation of heat by the motion of the magnetic flux complicates the analysis. Nevertheless, various methods for enhancing trapped magnetic fields through repeated excitation are being developed. These methods are eagerly anticipated as practical solutions to the problem of excitation (180). An experimental motor using bulk superconductors that are magnetized by pulsed excitation has now been completed. The motor was used successfully to power a golf cart (181).

An enhanced torque motor has been achieved by using a Fe/HTS "zebra" reluctance motor (182). In this design, the rotor consist of a series of alternate iron and superconducting plates. Theoretical considerations suggest that an equal distribution of the iron and superconducting plates works best.

4.14.5.2. Magnetic Separation Applications. Trapped magnetic fields exhibit a triangular pyramid shape with their peak occurring at the center. Consequently, a large field gradient is naturally attained. As indicated by equation 54, the force acting upon the magnetic substance (magnetization M) is not proportional to the strength of the magnetic field, but to the field gradient (dH/dx). Bulk superconductors with relatively small magnetizations are then acted upon by large electromagnetic forces. This phenomenon creates the potential for bulk superconductors to be used as high performance magnetic separators. In view of the many environmental problems that are now attracting concern, high performance magnetic separators are expected to have a far reaching effect on matters, such as the effective use of resources and the removal of hazardous materials.

4.14.5.3. Other Magnetic Field Applications of Bulk Materials. Numerous other applications exist for superconducting bulk magnets. For example, the use of Fe–Nd–B magnets in industrial equipment is now of interest. In many cases, the superconducting magnets must be magnetized after they have been incorporated into a larger device or system. In this situation, the bulk superconductors are treated as a "magnetization unit". Small bulk superconductors are capable of trapping magnetic fields that are as large as 10 T. Furthermore, the shape of the superconductor can be used to localize the magnetic field in a specific area, allowing magnetic field leakage that could harm nearby equipment to be prevented. Bulk superconductors can therefore be used to generate large magnetic fields over a specific area for use in testing equipment, measuring equipment, etc. The development of refrigerators has been advancing rapidly in recent years. If researchers can develop a bulk magnet component that is removable and easily transportable, the range of potential applications will be greatly expanded. For example, a proposal has been made to use a pair of bulk superconductors as a magnetic clamp for holding metallic plates together without the need for welding or bolting (183). Easily transportable bulk superconductors would also allow equipment, eg, magnetic separators, to be used in remote areas where electricity is not immediately available. Many superconducting bulk applications are dependent on the development of peripheral technologies, eg, cooling mechanisms. Once these technologies have been established, the range of applications is expected to widen even further.

4.15. HTS and LTS Josephson Devices

The S–I–S tunnel junctions are used in SQUIDs, electronic circuits like RSFQ-logics, high speed computers, conventional microcallorimeters, single-electron tunneling devices, in the voltage standard, X-ray detectors, and optical detectors. Superconducting tunnel junctions (STJs) have been extensively investigated as photon detectors covering the range from near-ir to X-ray energies. A 6 × 6 array of tantalum junctions has already been used in an optical spectrophotometer. With this camera, the European Space Agency has performed multiple astronomical observations of optical sources using the William Herschel 4.2-m telescope at La Palma. Following the success of this program, Oxford Instruments developed a second generation camera (184).

4.15.1. S–I–S Tunnel Junctions, SQUID

The S–I–S tunnel junctions are also employed as sensitive power sensors (bolometers) for electromagnetic waves in the ir or microwave region, eg, in the field of astronomy. SQUIDs are used for biomagnetic measurements and NDE (nondestructive evaluation), eg, of aircraft rivets and rims. The SQUID magnetometers are used to measure extremely weak quasistatic magnetic fields. There are two types of SQUIDs available for this purpose, dc and radio frequency (rf). The dc SQUIDs use two Josephson junctions connected in parallel, with an applied dc current. For this SQUID, the junctions must be nonhysteretic. When an external magnetic flux is applied, the two junctions interfere with each other, causing the total critical current and the voltage to modulate with a certain period, equation 56. The phase difference between junction A and B can be expressed as

$$\phi_B - \phi_A = \frac{2\pi}{\Phi_o} \oint A\,dl = 2\pi \frac{\Phi}{\Phi_o} \tag{57}$$

for a ring with n junctions, the result is the same,

$$\sum_n (-1)^n \Phi_o = 2\pi \frac{\Phi}{\Phi_o} \tag{58}$$

Measurements of these interference effects can be used to determine the external magnetic flux. An rf SQUID uses a superconducting loop containing a Josephson junction to measure the external magnetic field (185). Properties of the SQUID vary periodically due to the applied magnetic flux, and these variations are measured to determine the flux. In contrast to the classical electrocardiography (ECG) method, MCG systems work without contact to the body and additionally allow the spatial reconstruction of the current paths on the heart muscle with a large diagnostic potential. This is under clinical evaluation. It has been found that a single Josephson junction can be used as a switch. This relies on the hysteretic nature of the junction. The zero voltage and nonzero voltage states of the junction are designated as on and off positions for the switch. The state of the junction is changed by temporarily increasing the current to force the system to take the nonzero voltage state or by temporarily reducing the current to force the system to assume the zero voltage state. One benefit is that the state can change extremely rapidly, on the order of tens of picoseconds (186). The other main benefit of these switches is that very little energy must be expended to change the state of the switch. Josephson switches have found application as memory devices and logic circuits.

A successful demonstration uses the patterned flexible-coated conductor $YBa_2Cu_3O_7$/YSZ/Hastelloy characterized by $J_c > 10^5$ A/cm^2 at 77 K as a transformer to form an axial first-order gradiometer in combination with the dc SQUID and superconducting shielding (187). The strip-line is bent in a way that the two pick-up loops of the transformer are facing each other. In this configuration, the system is sensitive to axial first-order gradients in the x direction, and magnetic fields, in the z direction perpendicular to the magnetometer plane. A superconducting shield is employed to reduce the magnetometer response to the z-oriented field. Such an axial HTS SQUID gradiometer may find use in geophysics, offering magnetic gradient tensor measurements that are advantageous compared to either conventional total magnetic field intensity geophysical surveys or magnetic vector surveys. Because economic geophysical targets require gradient sensitivities of better than 10 pT/m, SQUID gradiometers offer the potential for providing a gradient tensor system (188,189).

4.15.2. Thallium-based Devices

Among the active Tl-based devices fabricated to date are bolometric ir detectors and SQUIDs. Another exciting development has been that of a flux-flow transistor (SFFT), a three-terminal device that exploits the weak pinning in TBCCO films. It can be switched between the flux-flow state and a lossless state by a combination of the field in the device and bias across the weak-link array (190). It has been shown that the TI-based SFFT device is faster than the comparable Y-123 device by virtue of lower flux pinning, and hence higher flux velocities (191). The SFFT was used as a microwave amplifier in phase shifters for eventual use in space communications and in amplifiers for Fourier transform infrared (FTIR) detectors (192). The TI step-edge junction technology is being developed to attain capability to produce high quality junctions with relatively high yield and good uniformity within a junction and across a wafer. A reflective microwave switch made of TBCCO thin film has also been developed for signal control applications (193). An area that deserves more attention is the study of nonbolometric response of TBCCO films. The potentially subpicosecond response times of HTS materials make them attractive for the development of ultrafast optical and electrical switches and devices for use in optical and microwave signal processing (133).

A wide range of passive devices have already been demonstrated by using TBCCO superconductors (eg, interconnects, stripline, waveguides). A 1-ns microstrip delay line using TI-2212 thin films was fabricated in 1990 (194). It has also been demonstrated that TI-2212 films can make efficient Josephson mixers at 77 K. When integrated with an antenna structure, these mixers have broad applications at submillimeter wave and FTIR frequencies (195). It is natural to expect that as the processing technology for TBCCO thin films advances, it would become feasible to explore them for utilization in many more devices. Of course, the patterning and contacting technologies for these films, have to make progress simultaneously in order to move toward a strong device-based input (196).

4.15.3. MgB_2 Devices

Experimentally observed single-picosecond dynamics of Cooper pairs in MgB_2 show that MgB_2 is a good candidate for ultrafast superconducting electronic and optoelectronic devices and is similar to Nb-based materials. The MgB_2 thin films will be able to operate as efficient photon counters with counting rates exceeding 100 GHz (197).

4.15.4. Cellular Phone Base Stations

Cellular phone base stations will use HTS filters. Some experts predict that this will be one of the most significant early markets for HTS, but only if reliability has been achieved.

5. Conclusion

These are only a few of the many possible uses for superconductors. Research and development of HTS may still yield many more uses for materials that can carry electricity without resistance. However, as today's new technologies move into the marketplace, they will have a great effect on the way electricity is generated, delivered, and used, and on the medical and transportation technologies of tomorrow.

6. Nomenclature

A_m	material constant
a, b, c	crystallographic axes
a_n	normal domain size
a_s	superconducting domain size
a_o	triangular fluxon lattice spacing
A_{O2}	characteristic temperature in oxygen content equation
a_1, a_2	sample dimensions
B	magnetic flux density (magnetic induction)
B_{self}	calculated self induction generated by critical current in zero external magnetic field
B_{irr}	irreversibility induction
$B(x)$	flux density at distance x inside the metal
B_a	flux density of the applied field
B_{c1}	first critical magnetic induction
B_{c2}	upper critical magnetic induction
B_{c3}	third critical magnetic induction
$b=B/B_{c2}$	normalized (reduced) induction
b_p	full penetration field

b_o	external field below full penetration field, b_p
C_{el}	electronic specific heat
C	capacitance
D	grain size
d_w	wall energy parameter
d	thickness of superconducting film
d_b	block-layer spacing which separates the CuO_2 layers
e	electron charge it can be also (e_1 or e_2)
E	electric field
E_c	represents the superconducting condensation energy
F	force per unit length acting on a normal core
F_r	repulsive force
F_p	pinning force
F_L	Lorentz force
F_v	force acting in a direction opposite to the vortex velocity v
G	geometrical function of the microstructure
H_a	applied magnetic field
H_{ext}	external magnetic field
H_{c1}	first critical field
H_{c2}	upper critical field
$H_{c2(ab)}$	upper critical field along the ab plane
$H_{c2(c)}$	upper critical field along the c axis
H_{c3}	third critical field
H_c	thermodynamic magnetic field
H_D	demagnetizing field
H_i	internal field
$H_{irr(c)}$	irreversibility field along the c axis
$H_{irr(ab)}$	irreversibility field along the ab plane
H_{self}	self field
h	Planck's constant
	$h/2\pi$
I	transport current
I_c	critical current
I_{c1}	$I_{c1}=I_c/N_f$ critical current of one filament
$I_{c1\mathrm{cov}}$	critical current of one filament with magnetic cover
i_d	diamagnetic superconducting screening currents
i_p	paramagnetic superconducting current
i_A	current in superconducting branch A
i_B	current in superconducting branch B
i	normalized current $i=I/I_c$
J	current density
J_S	current density at the surface
J_c	critical current density
J_e	engineering critical current density
$J_{c,\mathrm{mag}}$	magnetic intragrain critical current density,
I_c	critical current
K	material coefficient or constant
K_{md}	decoupling loss reduction coefficient
k	constant, $V=kI^n$
$k(i)$	empirical parameter $k(i)=\frac{Q_{1\,\mathrm{cov}}}{Q_1}$
k_j	parameter defining the J_c *versus* superconductor thickness dependence
k_B	Boltzman's constant
k_p	smoothing parameter defining maximum pinning value

L_B	inductance of the superconducting path B
L_A	inductance of the superconducting path A
l	length
l_e	mean free path for electron in material
M	magnetization
M_{AB}	mutual inductance between superconducting branches A and B
M	the mass of ions forming the crystal lattice
M_r	remanent magnetization
M_f	the intensity of the trapped magnetic field
m	electron mass
m'	fitting parameter
N_d	demagnetizing coefficient
N_e	number of subelements in an individual bundle
N_f	number of filaments
$N_s(E)$	density of states
N_s	number of superelectrons per unit volume
n	integer (a multiplies)
n	power component, $V=kI^n$
n_s	density of superelectrons
n_c	carrier density
n'	fitting parameter
n_d	density of the Fluxons (number of Fluxons, n_f, divided by sample surface)
n_b	stacking number in the individual bundle arrangement
n_c	carrier density
P_o	constant independent of grain size
P	conductor overall filling factor
$\boldsymbol{p}_i$	quasi-particle momentum
P_i	filling of the individual bundle arrangement
p_h	hole concentration per Cu atom
p	fitting parameters of the $f(b)$ function
R_n	normal resistivity
R	coil radius
r	size of the loop through which the critical current flows
S	surface
S_s	cross-section of an individual subelement
S_t	cross-section of the external tubes
Q	electromagnetic losses
$Q*$	normalised transport losses
Q_t	transport losses per cycle
Q_m	magnetic losses
Q_{st}	magnetic losses in standard multifilamentary superconductor
Q_{cov}	magnetic losses in magnetic covers (cov), around individual filaments
q	fitting parameters of the $f(b)$ function
T	absolute temperature in kelvin
T_o	temperature constant
T_f	torque
T_s	saturation temperature
T_g	growth temperature
T_p	peritectic temperature
T_c	critical temperature
T_{irr}	irreversibility temperature
T_{LP}	non-Fermi liquid-pseudogap transition temperature
t	normalized temperature, $t = T/T_c$
t_s	thickness of superconductor
V_c	volume of the crystal
V	voltage

v	velocity
v_{i}	velocity of electrons
v_{F}	Fermi velocity
W	energy loss in superconductor per cycle
w	number of tunnel junctions
x	amount of oxygen in the perovskite
α, β, γ	grain misorientation angle also parameter
α	angle at which the vortex motion makes with the transport current
β_{c}	McCumber parameter
γ	electronic specific heat coefficient
Δ	the superconducting energy gap
ε	Ginzburg-Landau mass anisotropy parameter
η	viscosity constant
Θ	angle between magnetic field direction and crystal c-axis
ϑ	Characteristic angle (critical current vs. grain boundary dependence)
κ	Ginzburg-Landau parameter
λ	penetration depth
λ_{ab}	penetration depth in ab plane
λ_{c}	penetration depth in c plane
$\lambda*$	dimensionless electron–phonon coupling strength
λ_{L}	London penetration depth
μ_{o}	permeability of free space
ξ	coherence length
ξ_{O}	London coherence length
ξ_{ab}	coherence in ab plane
ξ_{c0}	c-axis correlation length
ξ_{c}	coherence along the c-axis
ξ_{p}	Pippard introduced the modified coherence length
ρ	resistivity
σ	stress
υ	velocity of normal cores
Φ	flux
Φ_{o}	fluxon
$-\Phi_{\mathrm{o}}$	anti-fluxon
Φ'	Fluxoid $\Phi' = n_{\mathrm{f}}\Phi_{\mathrm{o}}$
ϕ_{ab}	angle of magnetic field in respect to ab planes of superconductor
ϕ	angle between the crystallographic axis and magnetic field
ϕ_{A}	phase of junction A
ϕ_{B}	phase of junction B
χ	magnetic susceptibility
Ψ	wave function
Ψ_{o}	maximum value of the wave function
ω_{c}	characteristic frequency
ω_{D}	Debye's frequency

BIBLIOGRAPHY

Cited Publications

1. H. K. Onnes, *Common. Phys. Lab.* **12**, 120 (1911).
2. G. Nardin, L. Randaccio, and E. Zangrando, *Acta Crystallgr.* **B45**, 521 (1989).
3. R. L. Powell and A. F. Clark, *Cryogenics* **18**, 137 (1978).

4. B. A. Glowacki and S. A. Ignatowicz, *Cryogenics* **27**, 162 (1987).
5. L. N. Cooper, *Phys. Rev.* **104**, 1189 (1956).
6. J. Bardeen, L. N. Cooper, and J. Schrieffer, *Phys.Rev.* **106**, 162 (1957).
7. E. Maxwell, *Phys. Rev.* **78**, 477 (1950).
8. C. A. Reynolds, B. Serin, C. Wright, and L. B. Nesbitt, *Phys. Rev.* **78**, 487 (1950).
9. C. E. Gough and co-workers, *Nature (London)* **326**, 855 (1987).
10. P. W. Anderson and R. Schrieffer, *Phys. Today* **44**, 55 (1991).
11. A. P. Pippard, *Proc. R. Soc. London A* **203**, 210 (1950).
12. J. Bardeen, L. N. Cooper, and J. R. Schrieffer, *Phys. Rev.* **108**, 1175 (1957).
13. A. P. Pippard, *Proc.R. Soc. London A* **216**, 547 (1950).
14. F. London and H. London, *Proc. R. Soc. (London) A* **155**, 71 (1935).
15. E. M. Savitskii and co-workers, in K. Mendelssohn and K. D. Timmerhaus, eds., *Superconducting Materials*, The International Cryogenics Monograph Series, Plenum Press, New York, 1973, p. 12.
16. A. C Rose-Innes and E. H. Rhoderick, in R. Smoluchowski and N. Kurti, eds., *Introduction to Superconductivity*, International Series in Solid State Physics, Vol.6, Pergamon Press, New York, 1988, pp. 78, 185.
17. R. Hake, *Phys.Rev.* **158**, 356 (1967); and also S. Foner, and E. J. McNiff, *Appl. Phys. Lett.* **32**, 122 (1978).
18. A. A. Abrikosov, *Sov. Phys. -JETP* **9**, 1364 (1959).
19. H. Ullmaier, *Irreversible Properties of Type II Superconductors*, Springer-Verlag, Berlin, 1975, p. 141.
20. A. Tonomura, in T. Matsushita and K. Yamafuji, eds., *Proceedings of the 8th International Workshop on Critical Currents in Superconductors*, World Scientific, Singapore, 1996, p. 381.
21. K. A. Muller, M. Takashige, and J. G. Bednorz, *Phys.Rev. Lett.* **58**, 1143 (1987).
22. M. K Wu and co-workers, *Phys. Rev. Lett.* **58**, 908, (1987).
23. M. Suenaga, A. K. Ghosh, Y. Xu, and D. O. Welch, *Phys. Rev. Lett.* **66**, 1777 (1991).
24. A. Houghton, R. A. Pelcovits, and A. Sudbo, *Phys. Rev. B* **40**, 6763 (1989).
25. B. A. Glowacki and Z. Bukowski, *J.Mater. Sci.* **22**, 775 (1987).
26. J. H. Hinken, in J. L. Birman, H. Faissner, and J. W. Lynn, eds., *Superconductor Electronics, Graduate Text in Contemporary Physics*, Springer Verlag, Berlin, 1988.
27. B. D. Josephson, *Phys.Lett.* **1**, 251 (1962).
28. K. A. Delin and A. W. Kleinsasser, *Supercond. Sci. Technol.* **9**, 227 (1996).
29. A. F. Andreev, *Sov. Phys. JETP* **19**, 1228 (1964).
30. R. Roberge, in S. Foner and B. B. Schwartz, eds., *Superconductor Materials, Metallurgy, Fabrication and Applications*, Plenum Press, New York, 1981, p. 389.
31. X. Kawakami and H. Takayanagi, *Appl. Phys. Lett.* **46**, 92 (1985).
32. R. L. Powell and A. F. Clark, *Cryogenics* **18**, 137 (1978).
33. J. W. Ekin, *Appl. Phys.Lett.* **55**, 905 (1989).
34. C. J. G. Plummer and J. E. Evetts, *IEEE Trans. Mag.* **23**, 1179 (1987).
35. H. Jiang and co-workers, *Phys. Rev. Lett.* **66**, 1785 (1991).
36. C. P. Bean, *Phys. Rev. Lett.* **8**, 250 (1962).
37. D. X. Chen and R. B. Goldfarb, *J. Appl. Phys.* **66**, 2489 (1989).
38. D-N. Zheng, Ph.D. dissertation, University of Cambridge, 1994.
39. A. Sanchez, and C. Navau, *Supercond. Sci. Technol.* **14**, 444 (2001).
40. J. E. Evetts and B. A. Glowacki, *Supercond. Sci. Technol.* **13**, 443 (2000).
41. T. Takeuchi, *Supercond. Sci. Technol.* **13**, R101 (2000).
42. R. M. Scanlan, W. A. Fietz, and E. F. Koch, *J. Appl. Phys.* **46**, 2244 (1975).
43. M. Tinkham, *Introduction to Superconductivity*, McGraw-Hill, New York, 1975, p. 146.
44. G. Deutcher, in K. Kitazawa and T. Ishiguro, eds., *Properties of High-T_c Short Coherence Length Superconductors*, Advances in Superconductivity, Springer-Verlag, Tokyo, 2002, p. 384.
45. K. Kitazawa, *Ceramic Bull.* **68**, 880 (1989).
46. M. Tachiki and S. Takahashi, *Solid State Commun.* **70**(3), 291 (1989).
47. M. V. Feigelman, V. B. Geshkenbein, and A. I. Larkin, *Physica C* **167**, 177 (1990).
48. R. Herzog, Ph.D. dissertation, Cambridge University, 1997.
49. E. J. Kramer, *J.Appl.Phys.* **44**, 360 (1973).

50. A. Wisniewski, R. Pozniak, M. Baran, and R. Szymczak, in T. Matsushita and K. Yamafuji, eds., *Proceedings of the 8th International Workshop on Critical Currents in Superconductors*, World Scientific, Singapore, New Jersey, London, Hong Kong, 1996, p. 381.
51. B. A. Glowacki, *Intermetallics* **7**, 117 (1999).
52. P. Verhoeve and co-workers, Estec / ESLAB 1999/056/SA.
53. D. W. Face and D. E. Prober, *J. Appl. Phys.* **62**, 3257 (1987).
54. R. W. Heussner, J. D. Marquardt, P. J. Lee, and D. C. Larbalestier, *Appl. Phys. Lett.* **70**, 901 (1997).
55. G. Z. Chen, D. J. Fray, and T. W. Farthing, *Nature (London)* **407**, 362 (2000).
56. B. A. Glowacki and co-workers, *Physica C* **372–376**, 1315 (2002).
57. H. Hillman and co-workers, in M. Suenaga and A. F. Clark, eds., *Filamentary A-15 Superconductors*, Plenum Press, New York, 1980, p. 17.
58. H. Krauth, in K. Fossheim, ed., *Superconducting Technology*, World Scientific, Singapore, 1991, p. 149.
59. B. A. Glowacki and J. E. Evetts, *IEEE Trans. Mag. MAG* **25**, 2200 (1989).
60. B. A. Glowacki, in A. Narlikar, ed., *Frontiers in Superconducting Materials*, Springer Verlag, New York, 2005, p. 697.
61. J. J. Hanak and H. S. Berman, *J. Phys. Chem. Solids Suppl.* **C7**, 249 (1967).
62. K. Inoue, A. Kikuchi, Y. Yoshida, and Y. Iijima, *Physica C* **384**, 267 (2003).
63. M. Weger, *Rev. Mod. Phys.* **36**, 175 (1964).
64. J. Nagamatsu and co-workers, *Nature (London)* **410**, 63 (2001).
65. M. Cooper, *New Scientist* **2293**, 21 (June 2, 2001).
66. B. A. Glowacki and co-workers, *Supercond. Sci. Technol.* **14**, 193 (2001).
67. B. A. Glowacki and co-workers, *Supercond. Sci. Technol.* **16**, 297 (2002).
68. T. Serebryakova, *J. Less-Common Met.* **67**, 499 (1979).
69. D. C. Larbalestier, *Nature (London)* **410**, 186 (2001).
70. C. B. Eom and co-workers, *Nature (London)* **411**, 558 (2001).
71. H. H. Wen and co-workers, *Phys. Rev. B* **64**, 134505 (2001).
72. S. L. Budko and co-workers, *Phys. Rev. Lett.* **86**, 1877 (2001).
73. D. K. Finnemore and co-workers, *Phys. Rev. Lett.* **86**, 2420 (2001).
74. S. Jin, H. Navoori, C. Bower, and R. B. van Dover, *Nature (London)* **411**, 563 (2001).
75. M. Majoros, B. A. Glowacki, and M. E. Vickers **15**, 269 (2002).
76. K. Kishino and co-workers, *Physica C* **235–240**, 2775 (1994).
77. S. Soltanian and co-workers, *Supercond. Sci. Technol.* **16**, L4 (2003).
78. K. Komori and co-workers, *Appl. Phys. Lett.* **81**, 1047 (2002).
79. M. Paranthaman and co-workers, *Appl. Phys. Lett.* **78**, 3669 (2001).
80. B. A. Glowacki and M. Majoros, *Supercon. Sci. Technol.* **13**, 971 (2000).
81. B. A. Glowacki, M. Majoros, N. A. Rutter, and A. M. Campbell, *Cryogenics* **41**, 103 (2001).
82. R. Chevrel, M. Sergent, and J. Prigent, *J. Solid State Chem.* **3**, 515 (1971).
83. B. T. Matthias and co-workers, *Science* **175**, 1465 (1972).
84. E. Parthe, *Acta Crystallogr.* **B36**, 1 (1980).
85. O. Fisher and M. B. Maple, *Superconductivity in Ternary Compounds I; Topics in Current Physics*, Springer-Verlag, Berlin, 1982.
86. O. Fisher, *Appl. Phys.* **16**, 1 (1978).
87. B. Seeber, C. Rossel, O. Fischer, and W. Glaetzle, *IEEE Trans. Mag.* **19**, 402 (1983).
88. B. Seeber, M. Decroux, and O. Fisher, *Physica B* **155**, 129 (1989).
89. C. Rossel and co-workers, *Physica C* **165**, 233 (1990).
90. D. N. Zheng, H. D. Ramsbottom, and D. P. Hampshire, *Phys. Rev. B* **52**, 12931 (1995).
91. L. Le Lay, T. C. Willis, and D. C. Larbalestier, *Appl. Phys. Lett.* **60**, 775 (1992).
92. G. Deutscher and K. Muller, *Phys. Rev. Lett.* **59**, 1745 (1988).
93. K. Kitazawa and co-workers, *Physica C* **153–155**, 9 (1988).
94. Y. Tokura, J. B. Torrance, T. C. Huang, and A. I. Nazzal, *Phys. Rev.* **B38**, 7156 (1988).
95. K. Kitazawa, *Ceramic Bull.* **68**, 880 (1989).
96. R. H. Koch and co-workers, *Appl. Phys. Lett.* **51**, 200 (1987).
97. D. Dimos, P. Chaudhari, J. Mannhart, and F. K. LeGoues, *Phys. Rev. Lett.* **61**, 219 (1988).

98. B. A. Glowacki and M. Majoros, *Superconductor Sci. Technol.* **13**, 483 (2000).
99. J. G. Bednorz and K. A. Müller, *Z. Phys. B* **64**, 189 (1986).
100. M. K. Wu and co-workers, *Phys. Rev. Lett.* **58**, 908 (1987).
101. A. Schilling, J. D. Cantoni, J. D. Guo, and H. T. Ott, *Nature (London)* **363**, 56 (1993).
102. C. W. Chu and co-workers, *Nature (London)* **365**, 323 (1993).
103. M. G. Smith and co-workers, *Nature (London)* **351**, 549 (1991).
104. Y. Tokura, H. Takagi, and S. Uchida, *Nature (London)* **337**, 345 (1989).
105. J. M. Tarascon and co-workers, *Physica C* **162–164**, 285 (1989).
106. N. P. Ong and co-workers, *Phys. Rev. B* **35**, 8807 (1987).
107. S. H. Pawar, P. M. Shirage, and D. D. Shivagan, *Supercond. Sci. Technol.* **15** (2002).
108. B. Batlogg and C. M. Varma, *Physics World* **13** (Feb. 2, 2000).
109. C. Kawabata and T. Nakanishi, *J. Phys. Soc. Jpn.* **59**, 3835 (1990).
110. J. L. Tallon and co-workers, *Phys. Rev.* **B52**, R11972 (1996).
111. B. A. Glowacki and J. E. Evetts, *Mat. Res. Soc. Symp. Proc.* **99**, 419 (1988).
112. A. Goyal and co-workers *, J. Mater. Res.* **12**, 2924 (1997).
113. Y. Yamada, *Supercond. Sci. Technol.* **13**, 82 (2000).
114. B. A. Glowacki and co-workers, *Mater. Sci.* **37**, 157 (2002).
115. B. A. Glowacki, in A. Narlikar, ed., *Frontiers in Superconducting Materials*, Springer Verlag, New York, 2005, p. 765.
116. G. Hammerl and co-workers, *Nature (London)* **407**, 162 (Sept. 14, 2000).
117. N. A. Rutter and B. A. Glowacki, *IEEE Trans. Appl. Supercond.* **11**, 2730 (2001).
118. G. J. Schmitz, A. Tigges, and J. C. Schmidt, *Supercond. Sci. Technol.* **11**, 73 (1998).
119. Y. A. Jee, G-W. Hong, T-H. Sung, and C-J. Kim, *Inst. Phys. Conf. Ser.* **167**, 107 (1999).
120. M. Murokami, *Supercond. Sci. Technol.* **5**, 185 (1992).
121. H. London, *Phys. Lett.* **6**, 162 (1963).
122. W. T. Norris, *J. Phys. D. Appl. Phys.* **3**, 489 (1970).
123. I. Hlasnik, M. Majoros, and L. Jansak, in B. Seeber, ed., *Handbook of Applied Superconductivity*, Vol. 1, IOP Publishing, Bristol and Philadelphia, 1998, p. 344.
124. J. X. Jin, S. X. Dou, H. K. Liu, and C. Grantham, *IEEE Trans. Appl. Supercon.* **5**, 1051 (1995).
125. A. Kursumovic, R. P. Baranowski, B. A. Glowacki, and J. E. Evetts, *J. Appl. Phys.* **86**, 1569 (1999).
126. R. Heller and J. R. Hull, *IEEE, Tran. Appl. Supercon.* **5**, 797 (1995).
127. T. Kaneko, Recent Progress of Superconducting Wires Based on Bi-compounds, The International Workshop on Superconductivity, July 12–15, Okinawa, Japan, 1998.
128. S. Kobayashi, *Physica C* **258**, 336 (1996).
129. B. A. Glowacki and J. Jackiewicz, *J. Appl. Phys.* **75**(6), 2992 (1994).
130. S. P. Ashworth and co-workers, *IEEE Trans. Appl. Supercond.* **5**, 1271 (1995).
131. M. A. Subramanian, P. L. Gai, and A. W. Sleight, *Mater. Res. Bull.* **25**, 101 (1990).
132. C. N. R. Rao, A. K. Ganguli, and R. Vijayaraghavan, *Phys. Rev. B* **40**, 2565 (1989).
133. J. V. Yakhmi and A. M. Herman, in A. M. Herman and J. V. Yakhmi, eds., *Thalium-based High-temperature Superconductors*, Marcel Dekker, New York, 1994, p. 607.
134. J. B. Parise and co-workers, *Physica C* **159**, 239 (1989).
135. W. A. Little, *Phys. Rev. A* **134**, 1416 (1964).
136. W. A. Little, *Sci.Am.* **212**, 21 (1965).
137. D. Jerome, A. Mazaud, M. Ribault, and K. Bechgaard, *J. Phys. Lett.* **41**, L95 (1980).
138. T. Ishiguro and K. Yamaji, in P. Fulde, ed., *Organic Superconductors; 88 Springer Series in Solid-State Sciences*, Springer-Verlag, Berlin Heidelberg, 1989.
139. M. D. Bird, *Physica B* **216**, 193 (1996).
140. B. A. Glowacki and co-workers, *Physica C* **384**, 205 (2003).
141. M. Chen and co-workers, *Inst. Phys. Conf. Ser.* **148**, 719 (1995).
142. D. T. Ryan and co-workers, *Inst. Phys. Conf. Ser.* **167**, 1231 (1999).
143. P. F. Herrmann, in B. Seeber, ed., *Handbook of Applied Superconductivity*, Vol.1, Institute Publishing, Bristol and Philadelphia, 1998, p. 801.
144. J. Sakuraba and co-workers, *Supercond. Sci. Technol.* **13**, 12 (2000).

145. K. Sato and co-workers, *Supercond. Sci. Technol.* **13**, 18 (2000).
146. T. Matsushita, *Supercond. Sci. Technol.* **13**, 51 (2000).
147. B. A. Glowacki, *SMI Rev., Art Technol.* **2**, 3 (2002).
148. T. Matsushita, *Supercond. Sci. Technol.* **13**, 51 (2000).
149. S. J. Penn and co-workers, *IEEE Trans. Appl. Supercond.* **9**, 3070 (1999).
150. R. McDermott and co-workers, *Science* **295**, 2247 (2002).
151. J. W. Burgoyne, *Phys. World* **10**, 23 (2000).
152. Design Study for Staged Very Large Hadron Collider, Fcrmilab-TM-2149, 2001.
153. 2001 ed. Nan Phinney Report in the next linear collider, SLAC-R-571, 2001.
154. TESLA: The Superconducting Electron Positron Linear Collider with an Integrated X-ray Laser Laboratory, DESY-2001-0I1, 2001.
155. M. Wake, in K. Tachikawa, ed., *Proceedings of the International Workshop on Superconducting Materials*, Society of Non-Traditional Technology, Tsukuba, Japan, 23–27 Feb. 2001, p. 7.
156. Y. Ohsawa, K. Kato, and T. Homma, in Y. Murakami, ed., *Proceedings of the International Sympossium on New Developments in Applied Superconductivity*, Word Scientific, Singapore, 1989, p. 547.
157. H. J. Boening and J. F. Hauer, *IEEE Trans. Power Apparatus Systems* **104**, 302 (1985).
158. F. C. Moon, *Superconducting Levitation*, John Wiley & Sons, Inc., New York, 1994.
159. K. Sawa and co-workers, *Proceedings of the 4th Magnetic Suspension Technology, NASA* CP- 1998-207654, 1998, p. 353.
160. H. Ohsaki and N. Nozawa, *Inst. Phys. Conf. Ser.* **167**, 1083 (1999).
161. T. Kato and co-workers, *Advances in Superconductivity*, Vol. X, Springer, Tokyo, 1998, p. 877.
162. M. Murakami, *ISTEC J.* **12**, 37 (1999).
163. K. R. Davey, *IEEE Trans. Appl. Supercond.* **6**, 160 (1996).
164. Y. A. Jee, G-W. Hong, T-H. Sung, and C-J. Kim, *Inst. Phys. Conf. Ser.* **167**, 107 (1999).
165. M. Morita and co-workers, *Mat. Sci. Eng. B* **53**, 159 (1998).
166. Y. Itoh and U. Mizutani, *Jpn. I. AppI. Phys.* **35**, 2114 (1996).
167. J. R. Hull, *Supercond. Sci. Technol.* **13**, R1 (2000).
168. P. Malkin and D. Klaus, *IEE Rev.* **3**, 41 (2001).
169. M. Chen and co-workers, *Physica C* **372–376**, 1677 (2002).
170. P. Tixador and co-workers, *Cryogenics* **39**, 77 (1999).
171. R. Nies and co-workers, *Inst. Phys. Conf. Ser.* **167**, 1025 (1999).
172. S. V. Rylov and co-workers, *IEEE Trans. Appl. Supercond.* **7**, 2649 (1997).
173. A. L. Ward, R J Tan, and R. Kaul, *IEEE Trans. Microwave Theory Tech.* **42**, 1879 (1994).
174. J. C. Booth, K. Leong, and A. Schima, 9th International Superconductivity Electronics Conference, 7–11 July 2003, Sydney, Australia.
175. Y. Ren, R. Weinstein, J. Liu, R. P. Sawh, and C. Foster, *Physica C* **251**, 15 (1995).
176. T. Oka and U. Mizutani, *Haikangijutsu* **1**, 45 (1999).
177. H. W. Weber, in N. Koshizuka and K. Tajima, eds., *Advances in Superconductivity XI*, Springer-Verlag, Tokyo, 1999, p. 37.
178. M. Tomita and M. Murakami, *Nature (London)* **421**, 517 (2003).
179. X. Chaud, *Appl. Superconductivity* **1**, 148 (1995).
180. Y. Itoh and U. Mizutani, *Jpn. I. AppI. Phys.* **35**, 2114 (1996).
181. T. Oka and co-workers, *J. Jpn. Inst. Metals* **61**, 931 (1997).
182. G. J. Barnes, M. D. McCulloch, and D. Dew-Hughes, *Inst. Phys. Conf. Ser.* **167**, 1075 (1999).
183. M. Strasik and co-workers, *IEEE Appl. Supercond.* **9**, 183 (1999).
184. D. D. E. Martin and co-workers, in M. Iye and A. F. M. Moorwood, eds., *Proceedings of SPIE* Vol. 4841, 2003, p. 805.
185. D. Koelle and co-workers, *Rev. Mod. Phys.* **71**, 631 (1999).
186. T. Van Duzer and C. W. Turner, *Principles of Superconductive Devices and Circuits*, North Holland, New York, 1981.
187. M. Bick and co-workers, 9th International Superconductive Electronics Conference, PTh05, 7–11 July 2003, Sydney, Australia.
188. A. Chwala and co-workers, *Supercon. Sci. Technol.* **14**, 1111 (2001).

189. K. Leslie and co-workers, 9th International Superconductive Electronics Conference, PTh21, 7–11 July 2003, Sydney, Australia.
190. J. S. Martens and co-workers, *J. Appl. Phys.* **65**, 4057 (1989).
191. J. S. Martens and co-workers, *IEEE Trans. Appl. Supercond.* **1**, 95 (1991).
192. J. S. Martens and co-workers, *IEEE Trans. Appl. Supercond.* **2**, 111 (1992).
193. L. S. Martens and co-workers, *IEEE Microwave Guided Wave Lett.* **1**, 291 (1991).
194. L. C. Bourne and co-workers, *Appl. Phys. Lett.* **56**, 2333 (1990).
195. J. P. Hong and co-workers, *Appl. Phys. Lett.* **59**, 991 (1991).
196. J. V. Yakhmi and A. M. Herman, in A. M. Herman and J. V. Yakhmi, eds., *Thalium-based High-temperature Superconductors*, Marcel Dekker, Inc., New York, 1994, p. 607.
197. Y. Xu and co-workers, the 9th International Superconductive Electronics Conference, 7–11 July 2003, Sydney, Australia.

BARTEK. A. GLOWACKI
University of Cambridge

Related Articles

; ; ; ; Advanced Materials,